

ADVANCED PROCESSING OF GaN FOR NOVEL ELECTRONIC DEVICES

By

XIAN-AN CAO

2

A DISSERTATION PRESENTED TO THE GRADUATE SCHOOL
OF THE UNIVERSITY OF FLORIDA IN PARTIAL FULFILLMENT
OF THE REQUIREMENTS FOR THE DEGREE OF
DOCTORAL OF PHILOSOPHY

UNIVERSITY OF FLORIDA

2000

ACKNOWLEDGMENTS

I have been very fortunate to have the privilege of working with Prof. Stephen J. Pearton, which turned out to be an exciting and rewarding learning experience. It is his sharp insight, enlightened guidance and generous support that make it possible for me to finish a project like this. He also took a genuine interest in my personal development and ensured my growth by constant demands, advice and encouragement. I deeply appreciate the best of opportunities Prof. Pearton provided me, and credit his belief in my capability as an inspiration for achievement of my academic career. I am also indebted to Prof. Fan Ren. The value of the academic and personal relationship with him is undeniable.

Many thanks extend to Prof. Cammy R. Abernathy, Prof. Fred Sharifi, Prof. Rajiv K. Singh, and Dr. Jim M. Van Hove at SVT Associates, for their valuable contribution. The assistance from my group mates and from collaborators of Prof. Ren's group and Prof. Abernathy's group is highly appreciated.

Special thanks go to my family, without whom I would not be what I am, for their moral support and encouragement through all my professional endeavors.

TABLE OF CONTENTS

ACKNOWLEDGMENTS	ii
LIST OF TABLES	v
LIST OF FIGURES	vi
ABSTRACT	xiv
CHAPTERS	
1. INTRODUCTION	1
1.1 III-V Nitrides for Device Applications	1
1.2 GaN Technology: A Late Blooming	6
1.3 Processing Challenges for Novel Electronics	17
1.4 Dissertation Goal and Scope	21
2. SEMICONDUCTOR PROCESSING: THEORY AND BACKGROUND INFORMATION	23
2.1 Ion Implantation	23
2.1.1 Ion Stopping and Damage Introduction	23
2.1.2 Implant Isolation and Doping	27
2.2 Rapid Thermal Processing	29
2.3 Metal/Semiconductor Contacts	32
2.3.1 Schottky Contact	32
2.3.2 Ohmic Contact	36
2.4 Dry Etching	40
3. ULTRA-HIGH TEMPERATURE ACTIVATION OF IMPLANT DOPING IN GaN	47
3.1 Introduction	47
3.2 High Temperature Annealing and AlN Encapsulation	48
3.3 N-type Implant Doping	54
3.4 P-type Implant Doping	57
3.5 Dopant Redistribution	59
3.6 Residual Damage	67

4. HIGH RESISTANCE IMPLANT ISOLATION IN GaN	69
4.1 Introduction	69
4.2 O-implantation for Selective Area Isolation	71
4.3 Creation of High Resistivity GaN by Ti, Fe, and Cr Implantation	76
5. ELECTRICAL CONTACTS TO GaN	82
5.1 Introduction	82
5.2 Effects of Interfacial Oxides on Schottky Contact	85
5.2.1 $(\text{NH}_4)_2\text{S}$ Treatment to Reduce Schottky Barrier Height	85
5.2.2 Interfacial Insulator Model	92
5.3 Thermally Stable W-based Ohmic Contact	95
5.3.1 W on Si-implanted GaN	95
5.3.2 Behavior of W and WSi Contacts to p-GaN	98
6. DRY ETCH DAMAGE IN GaN	107
6.1 Introduction	107
6.2 Plasma Damage in n-GaN	109
6.2.1 Comparison of N_2 and H_2 Discharge Exposure	109
6.2.2 Effect of Etching Chemistries on Damage	114
6.2.3 Thermal Stability of Damage	124
6.3 Plasma Damage in p-GaN	126
6.3.1 Surface Type-Conversion Effects	126
6.3.2 Thermal Stability of Damage	134
6.4 Determination of Damage Profile in GaN	137
7. FABRICATION AND SIMULATION OF GaN-BASED BIPOLAR TRANSISTORS	145
7.1 Introduction	145
7.2 Common Base Operation of GaN BJT and AlGaN/GaN HBT	147
7.3 Growth and Processing Issues	156
7.4 Quasi-3D Modeling of Electrical Performance of GaN Bipolar Transistors...	164
7.4.1 npn Structure	166
7.4.2 pnp Structure	176
8. CONCLUSIONS AND FUTURE TRENDS	188
REFERENCES	193
BIOGRAPHICAL SKETCH	202

LIST OF TABLES

<u>Table</u>	<u>Page</u>
1.1 Comparison of 300 K semiconductor material properties.....	5
2.1 Boiling points for possible etch products of III-V nitrides etched in halogen- or CH ₄ /H ₂ -based plasmas.....	45
5.1 Summary of electrical data for test diodes.....	90
5.2 Temperature-dependent contact data for p-GaN.....	105
7.1 Parameters used in the simulations.....	165
7.2 npn GaN/AlGaN HBT structure and doping.....	166
7.3 Best and typical values of mobility and lifetime in each layer of the HBT.....	166
7.4 Layer structure and doping for pnp GaN/Al _{0.2} GaN HBT.....	177
7.5 Typical values of carrier mobility and lifetime in the various layers of the HBT....	177
8.1 Ion implantation doping in GaN.....	190

LIST OF FIGURES

<u>Figure</u>	<u>Page</u>
1.1 Bandgap of hexagonal (α -phase) and cubic (β -phase) InN, GaN, and AlN and their alloys versus lattice constant a_0	2
1.2 The various ternary and quarternary materials used for LEDs with the wavelength ranges indicated.....	2
1.3 Calculated breakdown voltage as a function of doping concentration and thickness of the drift region in GaN M- n^- - n^+ diodes.....	4
1.4 Electron drift velocity at 300 K in GaN, SiC, Si and GaAs computed using the Monte Carlo technique.....	4
1.5 Cross section TEM of typical MOCVD grown GaN using an AlN buffer layer on SiC (left) and typical LEO GaN (right).....	9
1.6 A survey of 300 K GaN electron Hall mobility values as reported by various groups. The solid line shows the calculated results for uncompensated n-GaN.....	11
1.7 Cross-sectional view of a typical structure of GaN-based laser diode.....	13
1.8 Conduction band structure of a modulation-doped structure.....	15
2.1 Schematic of the cross section S (proportional to the energy loss per unit distance) for electronic (S_e) and nuclear (S_n) stopping processes as a function of ion energy. Typical values for the parameters E_1 , E_2 and E_3 for O implanted in GaAs are: $E_1=10$ keV, $E_2=20$ keV, $E_3=4$ MeV.....	24
2.2 Index of interface behavior S as a function of the electronegativity difference of the semiconductors(a). Barrier height versus work function of metals deposited on n-GaN reported from various groups(b).....	35
2.3 Determination of contact and sheet resistance using the TLM measurements: (a) TLM pattern (b) resistance between the contact pads (width W) vs. distance between the contacts.....	39
2.4 Schematic diagram of RIE (top) and ICP (bottom) etch systems.....	44

3.1	Time-temperature profiles for Zapper TM RTP annealing at 1400 °C and 1500 °C.....	50
3.2	SEM micrographs (top) and RMS roughness (bottom) of GaN surfaces annealed at 1200 -1500 °C.....	52
3.3	SEM micrographs (top) and RMS roughness (bottom) of AlN surfaces annealed at 1150 -1450 °C.....	53
3.4	Sheet carrier concentration (a) and electron mobility (b) in Si-implanted GaN after uncapped and AlN-capped annealing.....	56
3.5	Arrhenius plots of sheet electron density in S (a) and Te (b) implanted GaN as a function of annealing temperature.....	58
3.6	Sheet carrier concentrations in Mg ⁺ and C ⁺ implanted GaN as a function of annealing temperature.....	60
3.7	Calculated and experimentally measured (by SIMS) profiles of implanted Si (150 keV, $5 \times 10^{15} \text{ cm}^{-2}$) in GaN.....	61
3.8	SIMS profiles of S ⁺ (top) and Te ⁺ (bottom) implanted GaN before and after annealing at 1450 °C (the profiles are essentially coincident).....	63
3.9	SIMS profiles of Mg ⁺ (top) and C ⁺ (bottom) implanted GaN before and after annealing at 1450 °C (the profiles are essentially coincident).....	65
3.10	SIMS profiles of Be ⁺ implanted GaN before and after annealing at different temperatures.....	66
3.11	TEM plan view (a) and selected -area diffraction pattern from Si ⁺ -implanted GaN after 1100 °C, 10 s annealing.....	68
3.12	TEM plan view (a) and selected-area diffraction pattern from Si ⁺ -implanted GaN after 1400 °C, 10 s annealing.....	68
4.1	Schematic of GaN structure for measurement of sheet resistance after ion implantation.....	71
4.2	Ion (top) and Damage (bottom) profiles for multiple energy O ⁺ implant sequence into GaN.....	73
4.3	Evolution of sheet resistance of n- and p-type GaN with annealing temperature after O ⁺ implantation (top), and Arrhenius plots of sheet resistance after either 300 °C (n-type) or 600 °C (p-type) annealing (bottom).....	75

4.4	Ion (top) and damage (bottom) profiles for multiple energy Fe^+ implant sequence into GaN.....	77
4.5	Evolution of sheet resistance of GaN with annealing temperature after Cr^+ (top) and Fe^+ (bottom) implantation.....	79
4.6	Arrhenius plots of sheet resistance in Cr^+ (top) and Fe^+ (bottom) implanted n- and p-type GaN after annealing at either 450 °C (n-type) or 600 °C (p-type).....	80
4.7	Schematic representation of the positions in the energy band gap of defect levels created by O, Fe, Cr and Ti implant into GaN.....	81
5.1	Forward (top) and reverse (bottom) I-V characteristics from AuPt/n ⁺ -GaN diodes of different diameters, either cleaned in a conventional fashion prior to metal deposition or with an additional (NH ₄) ₂ S treatment.....	87
5.2	Forward (top) and reverse (bottom) I-V characteristics from AuPt/n ⁻ -GaN diodes of different diameters, either cleaned in a conventional fashion prior to metal deposition or with an additional (NH ₄) ₂ S treatment.....	88
5.3	I-V characteristics from AuPt/p-GaN diodes of different diameters, either cleaned in a conventional fashion prior to metal deposition or with an additional (NH ₄) ₂ S treatment.....	89
5.4	I-V characteristics from complete GaN mesa diodes before and after (NH ₄) ₂ S treatment.....	91
5.5	Energy band diagrams at the interface of n ⁺ -GaN/metal and n ⁻ -GaN/metal with or without an interfacial oxide layer	94
5.6	Specific contact resistance for W on Si ⁺ implanted GaN, as a function of post-metallization annealing temperature.....	96
5.7	The x-ray diffraction results for the (a) as-deposited, (b)800 °C annealed, (c) 1000 °C annealed W on n ⁺ -GaN samples.....	97
5.8	SEM micrographs of W contact on Si ⁺ -implanted GaN after annealing at 750 °C.....	99
5.9	Annealing temperature dependence of I-V characteristics of WSi, W and Ni/Au contacts on p-GaN (60 s anneal times).....	101

5.10 SEM micrographs of Ni/Au contacts on p-GaN after 60 s anneals at 400 °C (top left) or 700 °C (top right), and W contacts after annealing at 400 °C (bottom left) or 900 °C (bottom right).....	102
5.11 Annealing time dependence at 700 °C of I-V characteristics from W contacts on p-GaN.....	103
5.12 Ionization efficiency of Mg acceptors in GaN, and Fermi-level position for GaN doped with 10^{18} cm^{-3} Mg acceptors as a function of temperature.....	105
5.13 Measurement temperature dependence of I-V characteristics of Ni/Au, W and WSi contacts on p-GaN.....	106
6.1 Schematic of GaN Schottky diode structure.....	110
6.2 I-V characteristics from GaN diodes before and after H ₂ (top) and N ₂ (bottom) plasma exposure (150 W rf chuck power, 5 mTorr) at different ICP powers.....	112
6.3 Variation of V _B in GaN diodes (top) and dc chuck self-bias (bottom) as a function of ICP source power in H ₂ or N ₂ plasmas (150 W rf chuck power, 5 mTorr)	113
6.4 I-V characteristics from GaN diodes before and after H ₂ (top) or N ₂ (bottom) plasma exposure (500 W source power, 5 mTorr) at different rf chuck powers.....	115
6.5 Variation of V _B in GaN diodes (top) and dc chuck self-bias (bottom) as a function of rf chuck power in H ₂ or N ₂ plasmas (500 W source power, 5 mTorr).....	116
6.6 Schematic of the diode structure (top) and SEM of a complete device (bottom).....	118
6.7 I-V characteristics from n-GaN samples exposed to ICP Cl ₂ /Ar (top) or Ar (bottom) discharges (500 W source power) as a function of rf chuck power prior to deposition of the rectifying contact.....	119
6.8 Variations of V _B and V _F (top), and n-GaN etching rate or dc self-bias (bottom) as a function of rf chuck power for n-GaN diodes exposed to ICP Ar and Cl ₂ /Ar discharges (500 W source power).....	120

6.9 I-V characteristics from n-GaN samples exposed to ICP Cl ₂ /Ar (top) or Ar (bottom) discharges (150 W rf chuck power, 500 W source power) as a function of plasma exposure time prior to deposition of the rectifying contact.....	122
6.10 Variation of V _B and V _F (top) and of n-GaN etch depth (bottom) as a function of plasma exposure time for n-GaN diodes exposed to ICP Cl ₂ /Ar discharges (500 W source power 150W rf chuck power).....	123
6.11 AFM scans of GaN surfaces (top) and I-V characteristics from GaN diodes (bottom) before and after N ₂ plasma exposure (500 W source power, 150 W rf power, 5 mTorr) and subsequent annealing at different temperatures prior to deposition of the Schottky contacts.....	125
6.12 I-V characteristics from GaN diodes with Schottky metal deposited on control samples (top) and plasma-exposed samples (bottom) followed by annealing at different temperatures.....	127
6.13 I-V characteristics from n-GaN samples exposed to ICP Cl ₂ /Ar (top) or Ar (bottom) discharges (500 W source power, 100 W rf chuck power) as a function of annealing temperature prior to deposition of the rectifying contact.....	128
6.14 Variation of V _B in n-GaN diodes exposed to ICP Cl ₂ /Ar or Ar discharges (500 W source power, 100 W rf chuck power) with annealing temperature prior to deposition of the rectifying contact.....	129
6.15 I-V characteristics from samples exposed to either H ₂ (top) or Ar (bottom) ICP discharges (150W rf chuck power) as a function of ICP source power prior to deposition of the Ti/Pt/Au contact.....	131
6.16 Variation of diode breakdown voltage in samples exposed to H ₂ or Ar ICP discharges (150 W rf chuck power) at different ICP source powers prior to deposition of the Ti/Pt/Au contact. The dc chuck self-bias during plasma exposure is also shown.....	132
6.17 Forward turn-on characteristics (top) and turn-on voltage (bottom) of diodes exposed to ICP Ar discharges (150 W rf power) at different ICP source powers prior to deposition of the Ti/Pt/Au contact.....	133
6.18 I-V characteristics from samples exposed to either H ₂ (top) or Ar (bottom) ICP discharges (500W source power) as a function of rf chuck power prior to deposition of the Ti/Pt/Au contact.....	135

6.19 Variation of diode breakdown voltage in samples exposed to H ₂ or Ar ICP discharges (500 W source power) at different rf chuck powers prior to deposition of the Ti/Pt/Au contact. The dc chuck self-bias during plasma exposure is also shown.....	136
6.20 I-V characteristics from samples exposed to ICP Ar discharges (750 W source power, 150 W rf chuck power) and subsequently annealed at different temperatures prior to deposition of the Ti/Pt/Au contact (top) and breakdown voltage as a function of annealing temperature (bottom).....	138
6.21 Wet etching rate of p-GaN in boiling NaOH solutions as a function of solution molarity.....	139
6.22 Wet etching rate of Ar plasma-exposed (750 W source power, 150 W rf chuck power) p-GaN as a function of depth into the sample.....	140
6.23 I-V characteristics from samples exposed to ICP Ar discharge (750 W source power, 150 W rf power) and subsequently wet etched to different depths prior to deposition of the Ti/Pt/Au contact (top) and breakdown voltage as a function of depth removed (bottom).....	142
6.24 Forward I-V characteristics from p-GaN samples exposed to ICP Cl ₂ /Ar (top) or Ar (bottom) discharges (500W source power, 150W rf chuck power) and wet etched in boiling NaOH to different depths prior to deposition of the rectifying contact.....	143
6.25 Wet etch depth versus etch time in boiling NaOH solutions for plasma damaged p-GaN.....	144
7.1 Layer structure for HBT and BJT.....	147
7.2 TEM cross-section of BJT structure grown on GaN buffer on sapphire.....	148
7.3 Schematic of process sequence for GaN/AlGaN HBT.....	149
7.4 SEM micrograph of complete HBTs	150
7.5 Common-base characteristics from 50 μ m diameter devices at 25 °C (top) and 250 °C (bottom). The emitter current was stepped in 200 μ A increments from 200 μ A.....	152
7.6 Gummel plot of GaN/AlGaN HBT at 25 °C.....	153
7.7 Common-base characteristics of GaN/AlGaN HBT at 25 °C.....	154

7.8	Common-base characteristics of 50 μm diameter BJT at 25 $^{\circ}\text{C}$ and 300 $^{\circ}\text{C}$. Emitter current was stepped from 10 to 70 mA in 10 mA steps.....	155
7.9	Common-base characteristics of BJTs at 25 $^{\circ}\text{C}$ as a function of different emitter current increments.....	157
7.10	I-V characteristics measured between emitter and collector for HBTs grown on different GaN buffers on sapphire substrates.....	158
7.11	SIMS profile of Mg in MBE grown GaN/AlGaN HBT structures.....	160
7.12	SIMS profiles showing H decorating the base region in an MOCVD grown GaN/AlGaN HBT structure.....	161
7.13	Annealing temperature dependence of I-V characteristics for Ni/Au on the p-type base layer.....	161
7.14	I-V characteristics of base-collector and base-emitter junctions in BJTs at 25 $^{\circ}\text{C}$ or 250 $^{\circ}\text{C}$	163
7.15	Cross-section of a GaN/AlGaN HBT with dimensions.....	164
7.16	Gummel plot (top) and dc current gain (bottom) for the HBT with structure of Table 7.1, assuming either optimistic or typical values for carrier mobility and lifetime.....	168
7.17	Gummel plot (top) and dc current gain (bottom) for the HBT with structure of Table 7.1, with either a graded or constant composition base layer.....	169
7.18	Effect on dc current gain of base thickness (top), electron mobility in base (center) or electron lifetime in base (bottom).....	171
7.19	Common-emitter characteristics for the HBT with structure of Table 7.1, for hole concentrations of $2 \times 10^{17} \text{ cm}^{-3}$ (top) or 10^{18} cm^{-3} (bottom) in the base.....	172
7.20	Effect of base contact resistance on Gummel plots.....	174
7.21	Effect of device operating temperature on Gummel plot (top) or the breakdown voltage of the C-E junction (bottom).....	175
7.22	Current gain as a function of collector current for HBT and BJT of the same layer thicknesses and doping.....	176

7.23 Gummel plot (top) and dc current gain (bottom) for the pnp HBT with structure of Table 7.4, with the collector contact either on top (i.e. to be side of the e and b contacts) or bottom of the sub-collector layer.....	179
7.24 Distribution of the current streamlines (top) and the recombination rates (bottom) at high injection regime for the pnp HBT with side collector contact structure	180
7.25 Distribution of the current streamlines (top) and the recombination rates (bottom) at high injection regime for the pnp HBT with bottom collector contact structure	181
7.26 Effect on dc current gain of base thickness (top), electron mobility in base (center) or electron lifetime in base (bottom) in the pnp HBT.....	182
7.27 Common-emitter characteristics for the pnp HBT with structure of Table 7.4, for hole concentrations of $2 \times 10^{17} \text{ cm}^{-3}$ (top) or 10^{18} cm^{-3} (bottom) in the base.....	184
7.28 Effect of base thickness on the reverse breakdown voltage of the CE junction in the pnp HBT.....	185
7.29 Effect of device operating temperature on Gummel plots (top) and dc current gain (bottom) of the pnp HBT.....	186
7.30 Comparison of dc current gain as a function of collector current for npn and pnp GaN/AlGaN HBTs with the same doping and thickness.....	187

Abstract of Dissertation Presented to the Graduate School
of the University of Florida in Partial Fulfillment of the
Requirements for the Degree of Doctor of Philosophy

ADVANCED PROCESSING OF GaN FOR NOVEL ELECTRONIC DEVICES

By

Xian-an Cao

May 2000

Chairperson: Professor Stephen J. Pearton

Major Department: Materials Science and Engineering

The 1990s have brought commercial viability of GaN-based photonic devices and startling progress of GaN-based field effect transistors. However, continued research is required to explore the full potential offered by the III-V nitride system, especially for microelectronic applications and power switches. Further improvement of fabrication procedures is one of high priorities of current research. A host of processing challenges are presented by GaN and related materials because of their wide-bandgap nature and chemical stability. A complete understanding in the critical areas such as ion implantation doping and isolation, rapid thermal annealing, metal contact, and dry etching process, is necessary to improve the routine device reproducibility, and should directly lead to optimization of device performance.

This dissertation has focused on understanding and optimization of several key aspects of GaN device processing. A novel rapid thermal processing up to 1500 °C, in

conjunction with AlN encapsulation, has been developed. The activation processes of implanted Si or Group VI donors, and common acceptors in GaN by using this ultrahigh temperature annealing, along with its effects on surface degradation, dopant redistribution and damage removal have been examined. 1400 degrees has proven to be the optimum temperature to achieve high activation efficiency and to repair the ion-induced lattice defects. Ion implantation was also employed to create high resistivity GaN. Damage-related isolation with sheet resistances of $10^{12} \Omega/\square$ in n-GaN and $10^{10} \Omega/\square$ in p-GaN has been achieved by implant of O and transition metal elements. Effects of surface cleanliness on characteristics of GaN Schottky contacts have been investigated, and the reduction in barrier height was correlated with removing the native oxide that forms an insulating layer on the conventionally-cleaned surface. W alloys have been deposited on Si-implanted samples and Mg-doped epilayers to achieve ohmic contacts with low resistance, and better thermal stability than the existing non-refractory contact schemes. Dry etching damage in GaN has been studied systematically using Schottky diode measurements. Wet chemical etching and thermal annealing processes have been developed to restore the ion-degraded material properties.

Based on these technical improvements, attempts have been made to demonstrate GaN-based bipolar transistors. The devices operated in common base mode at current densities up to $3.6 \text{ kA}\cdot\text{cm}^{-2}$ and temperatures up to 300 °C. The key issues which currently limit the device performance, such as high base resistance, poor impurity control, and defects resulting from the heteroepitaxial growth, have been addressed. Physically-based simulation suggested that GaN bipolar devices may still suffer from small minority-carrier lifetime in the absence of aforementioned processing problems.

CHAPTER 1 INTRODUCTION

1.1 III-V Nitrides for Device Applications

For the last three decades or so, the III-V semiconductor material system has been viewed as highly promising for semiconductor device applications at blue and ultraviolet (UV) wavelengths in much the same manner that its highly successful As-based and P-based counterparts have been exploited for infrared, red and yellow wavelength. As members of the III-V nitrides family, AlN, GaN, InN and their alloys are all wide band gap materials, and can crystallize in both wurtzite and zincblende polytypes. Wurtzite GaN, AlN and InN have direct room temperature bandgaps of 3.4 eV, 6.2 eV and 1.9 eV, respectively (Fig. 1.1). In cubic form, GaN and InN have direct bandgaps, while AlN is indirect. In view of the available wide range of direct bandgaps, GaN alloyed with AlN and InN may span a continuous range of direct bandgap energies throughout much of the visible spectrum well into the ultraviolet wavelengths. This makes the nitride system attractive for optoelectronic device applications, such as light emitting diodes (LEDs), laser diodes (LDs), and detectors, which are active in the green, blue or UV wavelengths.¹ Although similar applications based on InGaAlP heterostructures have been successfully demonstrated, this material system is limited to about 550 nm. The addition of III-V nitrides to the family of device-quality semiconductors is essential for developing full-color displays (Fig. 1.2) and the case of coherent sources high density optical storage technologies, and very likely devices for signal and illumination

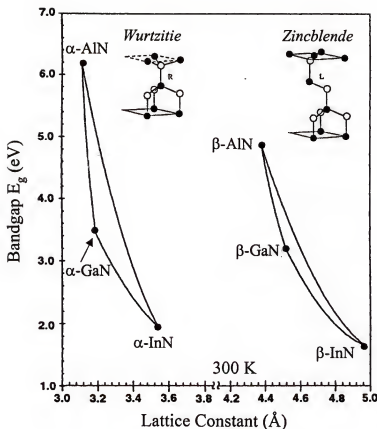


Fig. 1.1 Bandgap of hexagonal (α -phase) and cubic (β -phase) InN, GaN, and AlN and their alloys versus lattice constant a_0 .

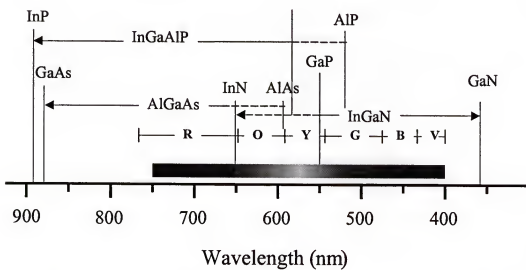


Fig. 1.2 The various ternary and quarternary materials used for LEDs with the wavelength ranges indicated.

application. Particularly, the combination of GaN-based blue and green LEDs with GaAs-based red LEDs forms the basis for large-scale full displays and white light illumination. The solid-state white light source generated by mixing the primary colors in a light scrambling configuration would provide not only compactness and high lifetime, but also would reduce power consumption by 80-90% compared to incandescent or fluorescent light sources.

Another area gaining a lot of attention for III-V nitrides is high temperature/high power electronics.² The interest stems from two intrinsic properties of this group of semiconductors. The first is their wide bandgap nature. The wide bandgap materials such as GaN and SiC, are promising for high temperature applications because they go intrinsic at much higher temperatures than materials like Ge, Si and GaAs. It means that GaN power devices can operate with less cooling and fewer high cost processing steps associated with complicated structures designed to maximize heat extraction. The second attractive property of III-V nitrides is that they have high breakdown fields. The critical electric field of the breakdown scales roughly with the square of the energy band gap, and is estimated to be >4 MV/cm for GaN,³ as compared to 0.2 and 0.4 MV/cm for Si and GaAs respectively. Fig. 1.3 is a plot of avalanche and punch through breakdown of GaN Schottky diodes calculated as a function of doping concentration and standoff layer thickness. It can be seen that 20 kV device may be obtained with ~ 100 μ m thick GaN layer with doping concentration $<10^{15}$ cm⁻³.

GaN has also excellent electron transport properties, including good mobility, and high saturated drift velocity as shown in Fig. 1.4.⁴ This makes it adequate for general

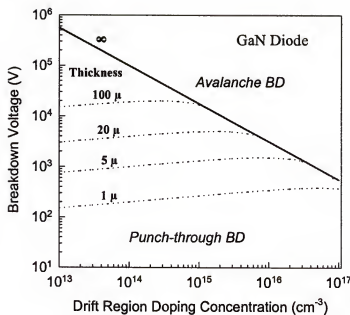


Fig. 1.3 Calculated breakdown voltage as a function of doping concentration and thickness of the drift region in GaN M-n-n⁺ diodes.

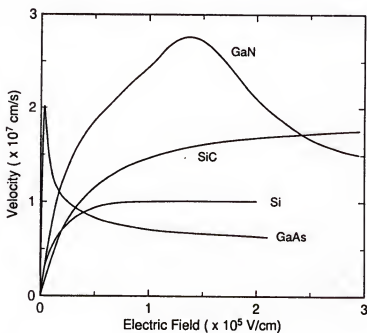


Fig. 1.4 Electron drift velocity at 300 K in GaN, SiC, Si and GaAs computed using the Monte Carlo technique.

electronics, and promising for microwave rectifiers, particularly. The material properties associated with high temperature, high power, and high frequency application of GaN and several conventional semiconductors are summarized in Table 1.1. It is anticipated that GaN may eventually prove to be superior to SiC in this area.

Table 1.1 Comparison of 300 K semiconductor material properties. (CFOM= Combined Figure of Merit for high temperature/high power/high frequency applications)

Property	Si	GaAs	4H-SiC	GaN
Bandgap E_g (eV)	1.12	1.42	3.25	3.40
Breakdown Field E_B (MV/cm)	0.25	0.4	3.0	4.0
Electron Mobility μ (cm ² /V·s)	1350	6000	800	1300
Maximum Velocity v_s (10 ⁷ cm/s)	1.0	2.0	2.0	3.0
Thermal Conductivity χ (W/cm·K)	1.5	0.5	4.9	1.3
Dielectric Constant ϵ	11.8	12.8	9.7	9.0
CFOM = $\chi\epsilon\mu v_s E_B^2 / (\chi\epsilon\mu v_s E_B^2)_{Si}$	1	8	458	489

The strongest feature of the III-V nitrides compared to SiC is the heterostructure technology it can support. Quantum well, modulation-doped hetero-interface, and heterojunction structure can all be made in this system, giving access to new spectral regions for optical devices and new operation regimes for electronic devices. From this point of view, III-V nitrides can be considered the wide band gap equivalent of the AlGaAs/InGaAs system which has set the modern benchmark for microwave device performance.

Other advantageous properties of III-V nitrides include high mechanical and thermal stability, large piezoelectric constants and the possibility of passivation by forming thin layers of Ga_2O_3 or Al_2O_3 with band gaps of 4.3 eV and 9.2 eV respectively. In addition, AlN has received considerable attention for its insulating property,⁵ particularly as a potential isoelectronic insulator for GaAs field effect transistors (FETs).

1.2 GaN Technology: A Late Blooming

Substantial research on III-V nitrides growth was initiated in early 1960s. However, they have trailed way behind the easier-to-grow Si and GaAs semiconductors on the development curve. Nearly 30 years later, Si and GaAs have been pushed to their theoretical limits, while nitrides are just beginning to show their promise. The technological spin-offs came late because ideal substrates could not be found and the consequent growth of GaN thin films contained substantial concentration of defects and had high n-type background. Even in films having relatively small background electron concentration, p-type doping could not be achieved until recently.

One particular difficulty in the growth of GaN thin films is the unavailability of sufficiently large (>1 cm) single crystals for use as substrate for homoepitaxial growth. Thus up to now, heteroepitaxial growth has been a practical necessity and the choice of substrate is critical. Possible substrate materials should have low thermal expansion and lattice mismatch with the grown crystals. Also, they should be unaffected by the growth chemistries (such as NH_3 or H_2) at high growth temperatures (in excess of 1000 °C in some cases). Under these presuppositions, sapphire and SiC are the most popular substrate materials used currently. When hexagonal GaN is grown on the (0001) basal

plane of Al_2O_3 , a lattice misfit of ~13% at the growth temperatures can generate high density of dislocations and defects in the thin film. In the practical case, a large part of the misfit is relaxed through 3D island growth. The residual strain is comparable to the lattice misfit between 6H-SiC and GaN, and result is comparable dislocation densities observed.⁶ Today, SiC substrates, though more costly, are of increasing interest for high temperature high power devices like transistors due to their good thermal conductivity and possibility of n- and p-type doping. The materials with a close lattice match with GaN, such as LiAlO_2 ⁷ and LiGaO_2 ⁸, were also used for epitaxial substrates. However, the grown GaN lacked the desired electronic properties due to either the rough growth or unintentional contamination from the substrates. The ideal candidate substrate is clearly a GaN wafer. Several research groups are investigating the growth of the bulk GaN crystals and very thick films through various techniques.⁹⁻¹¹ However, commercially available large area GaN wafers appear to be several years away. The nitride community is therefore challenged with growth of heteroepitaxial films.

Many epitaxial thin film growth processes have been developed, including molecular beam epitaxy (MBE),^{12,13} hydride vapor phase epitaxy (HVPE),^{9-11,14} metalorganic chemical vapor deposition (MOCVD),¹⁵⁻²⁰ and derivatives of these methods. In the past few years, MOCVD has evolved into a leading technique for production of III-V nitrides optoelectronic and microelectronic devices. One remarkable application worthy to be mentioned is the achievement of super-bright blue LEDs.¹⁸ Characteristics of this method include the use of high purity chemical sources, a high degree of composition control and uniformity, high growth rates, large scale manufacturing potential and the ability to grow abrupt junctions.

Initially the growth of GaN was performed directly on sapphire and SiC substrate, with large crystalline defects threading vertically from the substrate interface through the newly deposited thin film. The wafer usually had rough surfaces mainly caused by the 3D growth mode. In 1986, Amano et al.¹⁶ succeeded in remarkably improving the GaN surface morphology as well as the electrical and optical properties by deposition of a thin low-temperature AlN buffer layer prior to the high temperature growth of GaN. The essential role of this buffer is both to supply nucleation and promote lateral growth of the GaN film due to the decrease in interfacial free energy between the film and the substrate. Although the buffer layer has reduced the effects of the lattice mismatch, the densities of the threading defects in these thin films are still in the range of 10^9 - 10^{10} cm $^{-2}$, and on the order of one million times higher than in other semiconductor systems. These defect-laden materials, to date, have had a surprisingly small effect on the performance of both optical and electronic devices, but they may raise major questions as to the long-term stability of these devices. It is unlikely that the full promise of GaN and related alloys can be realized without a major reduction in the defect densities in the as-grown materials.

In 1994, the lateral epitaxial overgrowth (LEO) technique was employed to further improve the quality of the heteroepitaxially grown GaN by a marked reduction in defect density.¹⁹ In this method, a layer of GaN grown by MOCVD is covered with 100-200 nm of amorphous SiO₂ and Si₃N₄ with *ex situ* techniques. Small circular or rectangular "windows" are then etched through to the underlying GaN. A GaN film is subsequently regrown under conditions such that growth occurs epitaxially only in the windows and not on the mask. If growth continues, lateral growth over the mask eventually occurs. Since most of the extended dislocations propagate in the growth direction through GaN,

very few threading dislocations are visible in the regrown GaN that extends laterally over the mask. Marchand et al.²⁰ observed that the density of dislocation reaching the surface of LEO GaN was in the 10^4 - 10^5 cm $^{-2}$ range, while the film over the window regions still contained high levels of the threading defects. Fig. 1.5 compares the cross-section transmission electron microscopy (TEM) of a typical MOCVD growth and LEO GaN.

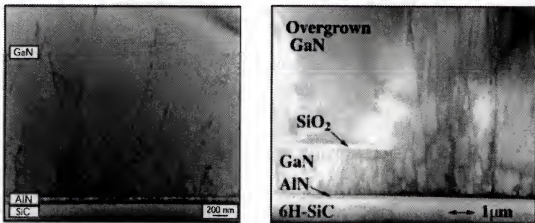


Fig. 1.5 Cross section TEM of typical MOCVD grown GaN using an AlN buffer layer on SiC (left) and typical LEO GaN (right).

A refined approach to a nearly dislocation free GaN substrate for devices can be employed by two successive LEO steps with the mask of the second step positioned over the opening defined by the mask of the first step, thus blocking the defects that grown out of the first windows. This complicated procedure offers the possibility of eliminating the disadvantages of heteroepitaxy, and will be important until GaN substrates become available.

In addition to growing GaN films with low defect densities, another key requirement for fabricating devices is the ability to precisely control the desired electrical properties of the thin film. In general, wide bandgap semiconductors are difficult to dope due to native defects. When the enthalpy for defect formation is lower than the band gap energy, the probability of generating a defect increases with the bandgap, i.e. the energy released by donor-to-acceptor transition. Particularly for GaN, MOCVD grown material is commonly n-type conductive, and N-vacancy was long believed to be the dominant donor. Many attempts have been made to avoid N-vacancy formation by growing GaN at high pressures and high temperatures.^{21,22} Efficient n-type doping of GaN through incorporation of Si during the growth proved relatively easy to achieve. Highly doping can also be created by implantation of Si or Group VI donors. Recently, Burm et al.²³ have shown a shallow Si implant at high dose to produce a doping density of $4 \times 10^{20} \text{ cm}^{-3}$, resulted in an extremely low ohmic contact resistance of $4 \times 10^{-8} \Omega \cdot \text{cm}^2$ using Ti/Au contacts.

Since conductivity is proportional to the product of carrier concentration and Hall mobility, another goal for GaN used in device applications is to obtain highest Hall mobilities possible. Fig. 1.6 summarizes the measured electron mobility in n-type GaN, along with the results obtained from Monte Carlo simulation.^{24,25} As can be seen, the experimental data is roughly half of the calculated value, possibly due to significant scattering from impurities and defects in the state-of-the-art materials.

The III-V nitrides are expected to be made p-type by inserting Column II elements such as Zn, Mg Be and Ca substitutionally for Ga to form single acceptors. However all of these divalent elements form deep acceptors, the shallowest being Mg with an ionization

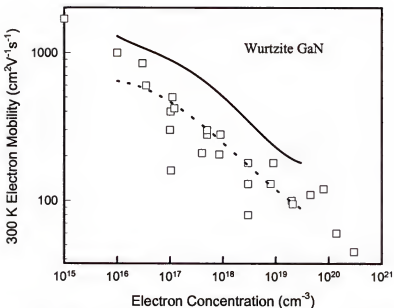


Fig. 1.6 A survey of 300 K GaN electron Hall mobility values as reported by various groups. The solid line shows the calculated results for uncompensated n-GaN.

level of 0.17 eV which is still many kTs above the valence bandedge of GaN.²⁶ At this acceptor level, one should only expect <10% of the Mg atoms to be ionized at room temperature, which means the Mg concentration needs to be approximately two orders of magnitude larger than the desired hole concentration. When MOCVD is used as the growth method, it has been difficult to obtain p-type conductivity. It was later found that hydrogen plays a crucial role in passivating the Mg acceptors, and creates a neutral complex Mg-H that prevents the formation of holes in GaN.²⁷ It was first shown by Amano et al.²⁸ that p-type conductivity can be achieved by activating Mg-doped GaN using low-energy electron irradiation. Nakamura demonstrated subsequently that the activation of Mg can also be realized by thermal annealing at ~700 °C.²⁹ Note that MBE

grown GaN doped with Mg may be p-type without a thermal activation process, because of the absence of hydrogen and H-N radicals during growth. In addition, p-type doping was also achieved by implant of Ca or Mg into GaN, followed by high temperature annealing (~ 1100 °C).^{30,31} The highest hole concentration reported so far is $\sim 10^{18}$ cm⁻³, and the typical hole mobility is very low, often 10 cm²·V⁻¹·s⁻¹ or below, but allowing the realization of p-n junctions. Achieving low resistance ohmic contacts to the GaN layers with poor p-type doping concentrations has proved to be troublesome. Recently, Brandt et al.³² found that by compensating Be with O, a neutral dipole is formed that does not scatter the holes. Hence a record high hole mobility of 150 cm²·V⁻¹·s⁻¹ was obtained. This may be the ideal contact layer for GaN based devices.

The current level of the progress in the development of GaN commercially viable devices, namely GaN based-LEDs, LDs and UV detectors, has been the direct result of the realization of high quality crystals of GaN, AlGaN, InGaN, and relatively recent achievement of p-type conduction in GaN. The first pn junction LED was demonstrated by Amano et al.²⁸ in 1989. Following this, Nichia Chemical Industries announced the commercial availability of blue LEDs with high efficiency and luminous intensities over 1 cd.¹⁸ In the subsequent years, high brightness single quantum well structure blue, green, and yellow InGaN LEDs with luminous intensities above 10 cd have been commercialized.^{33,34} In 1996, Nakamura et al.³⁵ reported the first current-injection GaN-based LDs with separate confinement heterostructure, and subsequently achieved continuous-wave (CW) lasing at room temperature.³⁶ Fig. 1.7 schematically shows the cross-section of the nitride-based laser diode. The active layer is a InGaN multiquantum well with a large number of well layers. GaN and AlGaN were used as the waveguide

and cladding layers, respectively. The mirror facet was formed by numerous methods, including dry etching, polishing or cleaving.

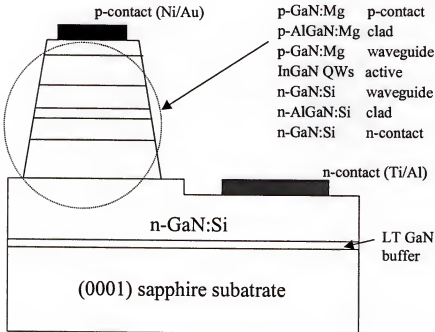


Fig. 1.7 Cross-sectional view of a typical structure of GaN-based laser diode.

Surprisingly, the high-density dislocations resulting from the heteroepitaxial growth on sapphire in these optical devices did not appear to be efficient nonradiative centers, as they are in other III-V materials. However, the crystalline defects do affect the device reliability. Nichia employed the LEO growth technique for their blue LDs and achieved an increase in device lifetime from a few hundred hours to an estimated 10,000 hours.³⁷ Another major problem limiting diode performance is high specific contact resistance of

ohmic contact on the p-GaN side of the junction. Present lateral GaN lasers suffer significant IR drops due to poor p-type doping and ohmic metallization.

The nitride material growth technology that supports the optical device efforts has also proven to be compatible with the development of electronic devices. In the past several years, the electronic device development has emphasized field effect transistor (FET) structures, because this important class of devices put smaller demands on the growth and fabrication technique compared to bipolar transistors. The rapid progress that has been made, especially in modulation-doped FETs (MODFETs), has been sufficient to show that GaN and related alloys will play a significant role in the future development of high temperature, high power, and high frequency electronic devices.³⁸⁻⁴¹

Fig. 1.8 presents a schematic representation of a GaN/AlGaN heterostructure. Due to the large conduction band discontinuity, the electrons diffusing from the large bandgap AlGaN into the smaller bandgap GaN form a 2D electron gas (2DEG) in the triangle quantum well at the interface, which is the hallmark of MODFET. The sheet carrier density of the 2DEG was found to be further enhanced by the strong piezoelectronic effect in GaN. Piezoelectronic coefficients in nitrides were measured to be about an order of magnitude higher than in traditional Group III-V semiconductors.⁴² Theoretical simulations have predicted a high peak electron velocity of $\sim 3 \times 10^7$ cm/s²⁵ and an electron mobility of ~ 2000 cm²·V⁻¹·s⁻¹ in the GaN channel at room temperature at a carrier concentration of 10^{17} cm⁻³.⁴³ Gaska et al.⁴ investigated the highest measured Hall mobility at room temperature was 2019 cm²·V⁻¹·s⁻¹, and increased approximately fivefold to 10,250 cm²·V⁻¹·s⁻¹ below 10 K for growth on 6H SiC substrate.

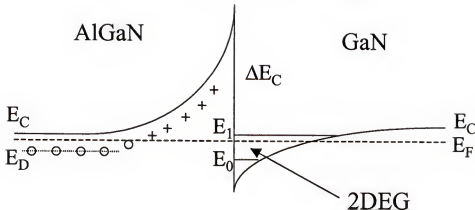


Fig. 1.8 Conduction band structure of a modulation-doped structure.

In 1993, Khan et al.³⁸ demonstrated the first AlGaN/GaN MODFET, with a g_m of 23 ms/mm and 2DEG mobility of $563 \text{ cm}^2 \cdot \text{V}^{-1} \cdot \text{s}^{-1}$ at 300 K. They also reported the first microwave results with f_t of 11 GHz and f_{\max} of 14 GHz.³⁹ In the early stages, the MODFETs exhibited very low transconductances and relatively poor frequency response. This is consistent with the defect-laden nature of the early GaN and AlGaN layers. With improvements in the materials quality, the transconductance, current capacity, drain breakdown voltage are all increased to the point that GaN-based MODFETs are now strong contenders in the arena of high power devices/amplifiers. To date, the highest power density achieved for a $0.45 \times 125 \mu\text{m}$ GaN MODFET is 6.8 W/mm at 10 GHz and associated gain of 10.65 dB.⁴⁰ The operation temperature has been pushed to 750 °C by employing a thermally stable Pt/Au gate contact.⁴¹

The published performances of epitaxial GaN-based MESFETs demonstrate that all the required components for a MESFET based technology are in place,^{44,45} i.e. an

appropriate high resistivity buffer/substrate combination has been developed for doped layer epitaxial growth, FET channels can be grown with thin n⁺ contact layers on which ohmic contact with adequate contact resistances have been achieved, gate metalizations which can pitch off the channel and support a high drain bias have been demonstrated, and it has been shown that both mesa etch and implant isolation can be used to define the active device area. Recently, an all implanted GaN junction FET,⁴⁶ a Si₃N₄ gated GaN MISFET,⁴⁷ and a Ga₂O₃(Gd₂O₃) gated GaN MOSFET⁴⁸ with reasonable performance were also reported. These types of devices potentially have advantage over MESFET, especially at high temperatures due to low reverse leakage currents.

So far, there are only several reports of development of GaN based bipolar transistors.^{49,50} Basically the device performance is limited by the difficulty in growth and processing related to the buried p-type layer and the small minority carrier lifetime. It is still far from commercialization of these devices, but their developments will follow the material improvements in the new decade, and much impetus comes from defense applications where ultrawide bandwidth and linearity are desired.

Group III-V nitrides offer a valuable combination of electrical, optical and piezoelectrical behavior, and enable the fabrication of LEDs, LDs, detectors, and transistors. In the past, the poor quality of the materials, the lack of p-type doping, and the absence of reliable processing procedures thwarted engineers and scientists from fabricating these useful devices. However, the 1990s have brought significant advances in the sophistication of growth techniques, the purity of the chemicals used for film deposition, the controlled introduction and activation of selected impurities, and progress in processing techniques. Most of the aforementioned obstacles have been sufficiently

overcome, and the electronic and optical devices have been demonstrated and partially commercialized. Market projections show that GaN-based blue and green LEDs will represent the majority of the estimated \$3 billion per year GaN-based device market by 2006. In transistors, GaN can go where no other semiconductors have gone before. The future development in this area will definitely be fueled by the increasing demand for high temperature, high power applications. From materials science to device engineering, from laboratory research to commercial products, III-V nitride technologies have shown a late but exciting blooming.

1.3 Processing Challenges for Novel Electronics

While further improvements in the III-V nitride materials quality can be expected to enhance device operation, further device advances will also require improved processing technology. Owing to their wide bandgap nature and chemical stability, GaN and related materials present a host of device processing challenges, including poor p-type doping (by implantation), difficulty in achieving reliable low-resistance p-ohmic contacts, high temperatures needed for implant activation, lack of efficient wet etch process, generally low dry etch rates and low selectivity over etching masks, and dry etch damage. These problems constitute a major obstacle to successful demonstration and commercialization of some GaN-based devices, such as bipolar transistors and power switches, whose performance are much more affected by the immature fabrication techniques. To fully exploit these device applications, a number of critical advances are necessary in the areas of implantation doping and isolation, high temperature thermal processing, ohmic contact to p-type material, dry etching process, and device passivation.

Ion implantation is an enabling technology for creating selective area doping and forming high resistance regions in device structures. For the development of ion implantation doping for advanced GaN-based electronics, it is important to understand the dopant activation process, and implantation-induced damage generation and removal. Recent studies have showed that quite good activation efficiency can be obtained by annealing at 1100 °C anneal,^{30,51} but implantation damage can not be significantly removed at this temperature. Annealing at temperatures >1300 °C are suggested to fully remove the damage and further optimize the transport properties of implanted regions in GaN.⁵¹ Since these temperatures are beyond the capability of most rapid thermal annealing systems, new annealing apparatus must be developed. Consequently, there is an urgent need to carry out detailed studies on the dopant activation, impurity redistribution, defect removal, and surface degradation at these elevated temperatures. Efficient surface protection must be developed to prevent material decomposition and N₂ loss from the GaN surfaces.

Ion implantation is also attractive for inter-device isolation and producing current guiding. Efficient compensation has been achieved in the GaN materials by using N or He implantation.^{30,52} However, the isolation is not stable at high temperatures, i.e. typical implant damage compensation. Implantation in In-containing III-V nitrides has shown that InGaN, as used in LED, laser cavity, or transistor channel, is difficult to be rendered highly resistive.⁵³ The defect level is usually high in the energy gap, not near midgap, as is ideal for implant isolation. There is a strong need for an understanding of the implant isolation process and mechanism in III-V nitride materials because of the emerging applications for high temperature, high power electronics based on this material system.

In particular, attempts need to be made to explore thermally stable implant isolation in GaN, and significant compensation must be achieved in the In-containing nitrides.

Considerable progress in the development of contacts to GaN has been made in the past several years.⁵⁴ Nevertheless, it is necessary still to improve upon the electrical performance of these contacts, particularly to achieve low contact resistances to p-GaN, and to develop contacts with greater thermal stability, which is critical for high current density devices. It has proven challenging to obtain acceptable low specific contact resistances on p-GaN. Values $\leq 10^{-5} \Omega\text{-cm}^2$ would be desirable in general for electronics, but more typical numbers are 10^{-1} - $10^{-3} \Omega\text{-cm}^2$. The high contact resistances can be attributed to several factors, including: (1) The absence of a metal with a sufficiently high work function (the bandgap of GaN is 3.4 eV, and the electron affinity is 4.1 eV, but metal work functions are typically ≤ 5 eV). (2) The relatively low hole concentrations in p-GaN due to the deep ionization level of the Mg acceptor (~ 170 meV). (3) The tendency for the preferential loss of nitrogen from the GaN surface during processing, which may produce surface conversion to n-type conductivity. In order to further lower the contact resistances to p-GaN, it will be necessary to further increase p-type conductivity or to lower the barrier height of the metal contacts, perhaps by growing a more readily contacted compositionally graded semiconductor alloy on the p-GaN.

The thermal stability of the contacts is also noteworthy. Annealing at ~ 700 °C resulted in interfacial reaction along with serious morphological degradation of the conventional Ti-based or Ni-based contacts.^{55,56} In the case of contact to p-GaN, the metallization will heat up as current flows across the interface due to the high series resistance, leading to metal migration down threading dislocations and eventual shorting

of the devices. Thermally stable Schottky contacts are also required for power amplifiers and optoelectronics that operate at high temperatures, but the electrical characteristics of the metal/n-GaN diodes have been reported to suffer degradation upon exposure to temperatures as low as 300 °C (Pd),⁵⁷ 400 °C (Pt),⁵⁸ 575 °C (Au)⁵⁹ and 600 °C (Ni).⁵⁴

Furthermore, there is a large scatter in the measured results of Schottky barrier height (SBH) and the ohmic contact resistance, suggesting that our understanding of the interface reactions, surface preparation, and non-idealities associated with the metal/GaN contacts is far from complete.

Dry etching has become the dominant patterning technique for the Group III nitrides due to the shortcomings in wet chemical etching. The etch rates in reactive ion etch (RIE) systems are generally low.⁶⁰ High density plasma etching, i.e. inductively coupled plasma (ICP)^{61,62} and electron cyclotron resonance (ECR)⁶³ etching have been developed in a variety of chlorine- and methane-based chemistries. The etch rates of GaN were reported as high as 9800 Å/min in a Cl₂/H₂/Ar mixture.⁶² However, surface roughening, N depletion, and degradation in electrical and optical properties were observed. Some device etching applications, such as gate recessing for FETs and base mesa formation for HBTs, can be particularly susceptible to ion-induced damage. In order to minimize the deleterious effects of energetic ions during dry etching, it will be necessary to develop effective low-damage etching processes that utilize ion energies well below 100 eV. At this point, it is also important to determine the nature of the plasma-induced damage in GaN, and to explore the procedures for damage removal.

GaN-based amplifiers and switches are attractive for high power applications in hostile environments. Reliable edge termination and passivation process are critical to

fully exploit these types of devices. There is not much work to date in this area. In addition, as discussed earlier, thermally stable doping, isolation, and metal contacts are all key issues for these special applications.

1.4 Dissertation Goal and Scope

This dissertation will investigate several important aspects of GaN processing. Emphasis will be placed on achieving high activation efficiency implant doping and high resistance implant isolation, developing ultra-high temperature thermal processing, achieving reliable low resistance ohmic contacts, and systematic study of dry etch damage. All the work is directed towards the optimizing the fabrication techniques of GaN-based optoelectronics and microelectronics. Particularly, fabrication of advanced GaN-based bipolar transistors will be attempted, based on these improved process modules. Finally, the simulation of the device performance will be performed as the implication for future trends in the arena.

Chapter 2 presents the physical mechanisms of several aspects of semiconductor processing, including ion implantation, rapid thermal annealing, metal contact, and dry plasma etching. The related background information of III-V materials are reviewed.

Chapter 3 starts with a review of efforts to develop implant doping in GaN to date. A novel rapid thermal processing up to 1500 °C is then developed, with AlN as encapsulation. The activation processes of implanted donors and acceptors in GaN using this ultra-high temperature annealing, along with its effects on surface degradation, impurity redistribution and defect removal are examined.

Chapter 4 discusses implantation isolation in n- and p-type GaN, with emphasis on comparison of the behavior of implanted O and transition metal elements like Fe, Cr and Ti in GaN. The compensation mechanism and the damage-related levels are determined.

In Chapter 5, early studies on ohmic contact and Schottky contact to GaN are reviewed. Then a new surface cleaning process using an additional $(\text{NH}_4)_2\text{S}$ treatment is developed. The thin native oxide left after conventional cleaning is found to have a strong influence on the contact characteristics on GaN. Finally the behavior of W-based ohmic contacts on both Si-implanted n-type GaN and Mg-doped p-type GaN is studied. The refractory contact schemes prove to be much more thermally stable than the more common metallizations.

Chapter 6 presents a systematic study of the effects of ICP Ar, H_2 , N_2 , and Ar/Cl₂ discharge exposure on the electrical properties of n- and p-type GaN. The thermal stability and depth of the plasma damage are determined. Two different techniques are developed to remove dry etch damage, i.e. wet chemical etching and thermal annealing.

In Chapter 7, the developed process modules are employed to demonstrate the first MBE grown GaN BJT and AlGaN/GaN HBT. The devices operate at high temperatures and high powers in common-base mode. The key issues related to structure growth and device fabrication are addressed. Finally, in order to gain a better understanding of the expected performance of GaN-based bipolar transistors, and as a suggestion for further work, physically-based simulation is performed using Atlas/Blaze.

Chapter 8 offers conclusions of the current work and an outlook for the future research.

CHAPTER 2

SEMICONDUCTOR PROCESSING: THEORY AND BACKGROUND INFORMATION

2.1 Ion Implantation

2.1.1 Ion Stopping and Damage Introduction

Ion implantation has played a major role in development of III-V semiconductor device technology. It is used to create the active layers by implanting a dopant species and then activating the dopant by high temperature anneal. The bombardment with energetic ions can also be utilized to create a high resistivity region selectively on a wafer that already contains doped layers.

The ion implanted into a semiconductor undergoes collisions with the target atoms, and loses energy due to the ion stopping process. Much of the ion energy is transferred to the lattice, as a localized thermal spike or to displace the target atoms. The total energy loss per unit distance is determined by two effects: the electronic stopping and the nuclear stopping. In the former process, the ion energy is lost by excitation and ionization of atoms, which suffer an inelastic collision with the ion. The lost energy eventually dissipates as heat, and does not create atomic displacements in the materials. The electronic stopping cross section is proportional to the velocity of the implanted ion and therefore to the square root of its energy. Its contribution dominates in the high-energy regime. Nuclear stopping occurs as a result of elastic collisions of ions with nuclei or whole atoms in the solid, in which, a part of kinetic energy of the incoming ion is

transferred to displace the nuclei absorbed this impart. These displaced nuclei may also have enough energy to displace other nuclei, leading to a cascade of recoiled atoms.

Nuclear energy loss dominates at intermediate energies, and leads to the creation of deep-level compensating defects. At high energies, the contribution from this process tends to be small because fast ions have only a short time to interact with a target nucleus, and cannot transfer energy efficiently. Fig. 2.1 shows a schematic of the relative energy loss due to electronic and nuclear stopping processes as a function of ion energy.⁶⁴ The relative importance of these two stopping mechanisms also depends on the mass of the implanted ions, the mass and atomic density of the target.

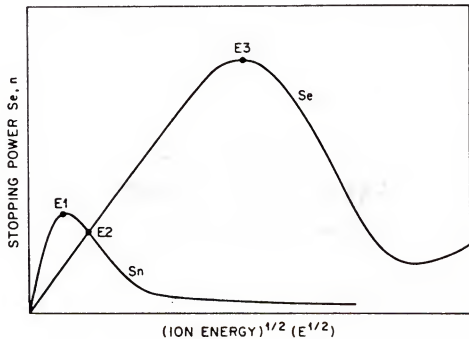


Fig. 2.1 Schematic of the cross section S (proportional to the energy loss per unit distance) for electronic (S_e) and nuclear (S_n) stopping processes as a function of ion energy. Typical values for the parameters E_1 , E_2 and E_3 for O implanted in GaAs are: $E_1=10$ keV, $E_2=20$ keV, $E_3=4$ MeV.

Both the stopping effects produce an energy loss rate of some tens of eV per angstrom in semiconductors. The total value of dE/dx is roughly constant for many ions over the ranges of energies of interest for implantation. The projected range R_p is then essentially proportional to the initial incident ion energy. With an amorphous target material, the ion profile follows purely Gaussian stopping distribution, which is related to the projected range R_p , standard deviation ΔR_p and implant dose Φ :

$$N(x) = \frac{\Phi}{\sqrt{2\pi}\Delta R_p} \exp\left[-\frac{(x - R_p)^2}{2\Delta R_p^2}\right] \quad (2.1)$$

The peak concentration $N_p = \frac{\Phi}{\sqrt{2\pi}\Delta R_p}$ occurs at R_p , and $N(x) = \frac{N_p}{\sqrt{e}}$ at $x = R_p \pm \Delta R_p$.

Considering the single crystal nature of the target, the channeling effect must be taken into account. Channeling takes place when implanted ions enter regions between rows of atoms, so that few nuclear collisions occur. The ions penetrate much deeper under these conditions than for implantation in a random direction, leading to large tails on the substrate side of the final profiles. It is better described by using joined Gaussians or by taking into account higher order moments such as skewness and kurtosis. Channeling can be minimized by rotating and tilting the sample with respect to the beam direction. The only completely effective method to eliminate it is to preamorphize the semiconductor. This is a successful procedure for implantation in Si, but is not appropriate for III-V materials.⁶⁴

Light ions slow down initially primarily by electronic stopping with little displacement damage until eventually nuclear stopping becomes dominant at the end of this range. By contrast, heavy ions undergo a relatively higher degree of nuclear stopping, displacing target atoms right from the surface inwards, producing collision cascades,

leading to considerable lattice damage within a small volume. Depending on the ion, the dose, and the implant temperature, the implant damage can consist of either amorphous layers or extended crystalline defects (dislocations and stacking faults). In III-Vs damage accumulation and possible amorphization are modeled by either a heterogeneous mechanism, in which individual damage clusters are considered to be amorphous and overlapping of these regions results in complete amorphization (heavy ions), or a homogeneous mechanism in which the crystal becomes unstable and collapses to an amorphous state when the defect density reaches a critical value (light ions). Since ions require certain threshold energy for the production of damage, the maximum of damage distribution is always closer to the surface than that of the ion profile. Note that for a particular ion to completely penetrate a doped semiconductor layer and render it semi-insulating, it is the ion damage profile that is important, not the ion profiles itself. Both the damage profile and dopant profile can be simulated by Monte Carlo calculations of energy deposition given up in atomic stopping processes.

In III-V semiconductors implantation can also lead to the creation of regions with local deviations from stoichiometry resulting from the different displacement properties of the lattice constituents, which have unequal masses.^{64,65} The lighter element recoils further, resulting in an excess of the heavier elements near the surface and an excess of the lighter elements at greater depths. Repair of the lattice during subsequent annealing requires displaced atoms diffusing back to appropriate sites. However, in III-V's, the displaced atoms are unable to move quickly enough to keep up with the regrowth front, leading to highly twinned materials. The electrical activation in regrown material is significantly worse due to the remnant disorder than if amorphization is avoided. The

formation of an amorphous layer can be prevented through elevated-temperature implantation, where more point defects are able to recombine and annihilate each other due to higher mobility. At very high dose rates, the sample may heat up, resulting in dynamic annealing, in which case an amorphous layer may never form. It has been observed that GaN has a very high threshold of amorphization, on the order of $\sim 10^{16} \text{ cm}^{-2}$ (Si implant, 100 keV).⁶⁶ This is in sharp contrast to GaAs where an amorphous region forms for room temperature implants near a dose of $\sim 10^{14} \text{ cm}^{-2}$,⁶⁷ and amorphization of InP occurs at even lower ion doses ($\sim 10^{13} \text{ cm}^{-2}$).⁶⁸

2.1.2 Implant Isolation and Doping

The damage produced by implantation reduces the carrier mobility in the material, and creates deep level centers, which trap free carriers. The material after implantation but before annealing tends to exhibit high resistivity. This is the basis for damage-induced isolation schemes widely used for III-V semiconductors. Due to hopping conduction effects the as-implanted resistivity in ion-bombarded material is generally not the maximum achievable, and subsequent annealing can increase the resistivity by several orders of magnitude as some of the damage is annealed and trapped carriers cannot hop from one damage site to another. At some characteristic temperature, the trap density falls below the carrier density in the material and carriers go back into the conduction or valence bands, reducing the resistivity back towards its initial value. The heavier ions are observed to have high carrier removal rates and high thermal stability of the compensation effect than for light ions. Usually a single-energy implant is inadequate to create uniform resistivity, because it fails to isolate the near-surface region. Particularly light ions do not create much damage at the surface due to large projected ranges, even

though multi-energy implant scheme is employed. One method to circumvent this problem is to implant through a surface dielectric layer.

Another important mechanism for production of high-resistivity regions in compound semiconductor relies on the implantation of a species, which either by itself or in combination with impurities or dopants already present in the materials, create a chemically active deep-level state. This type of compensation usually requires the implanted species to be substitutional, and hence annealing is required to promote the ion onto a substitutional site. The postimplantation resistance initially increases with annealing temperature, but then stabilizes at a high value as a compensating deep level formed. In the absence of out-diffusion or precipitation of this species, the isolation is thermally stable. In many respects this mechanism is complementary to the damage-induced method because the latter is thermally stable only up to the temperature at which damage is annealed out, which in most III-V materials is also the temperature at which chemically-active species become substitutional (typically ≥ 600 °C). This technique is particularly significant for GaN, since the thermally stable isolation may be necessary for high temperature and high power applications.

The temperature dependence of resistivity of the implant isolated material after optimally annealed could be described by:

$$\rho = \rho_0 \exp(E_a / kT) \quad (2.2)$$

where E_a is the activation energy corresponding to that required for promotion of an electron from the defect level to the conduction band, or a hole to the valence band. The value of E_a can be determined by temperature-dependent measurement of resistivity.

To achieve implant doping in semiconductors, annealing is required to remove the ion-induced compensation defects and to move the interstitial dopants to substitutional sites by short-range diffusion. The activation kinetics and maximum doping levels in III-V materials are strongly dependent on the nature and concentration of native point defects remaining after implantation and annealing. Activation efficiency could be limited by rapid diffusion, low solubility, or electrical self-compensation for some species. In some cases, co-implantation is used to improve the doping capability (e.g. Group II acceptors co-implanted with a Group V element). The purpose is to create a sufficient number of vacant sites that the initially interstitial dopant ions can occupy upon annealing. This maximizes occupation of lattice site by the dopants, and reduces the effective diffusivity of the dopants, thus increases their activation. The additional possible advantage gained from co-implant is higher dopant solubility due to formation of some chemical complexes.

Generally, higher n-type doping is achieved in InP and related compounds (also in III-V nitrides), and higher p-type doping is obtained in GaAs and related materials. The differences are thought to be due to differences in relative formation energies for the compensating native point defects that occur in doped III-V materials.⁶⁴

2.2 Rapid Thermal Processing

After implantation, the ions are in random positions and there is considerable lattice damage created by the stopping process. Post-implant annealing is required to repair the disorder and activate the implanted ions by causing their short-range diffusion to a lattice position.

The annealing of continuous amorphous layers proceeds by solid-phase regrowth in which the layer recrystallizes and the grown front proceeds towards the sample surface. Amorphous layers in III-V materials show poor crystallization, and exhibit high degrees of residual disorder in the form of microtwins, stacking faults and point defects. This is in sharp contrast to the regrowth of amorphous Si, which leads to defect-free layers in a single, solid phase epitaxial step at a temperature around 550 °C.⁶⁴

The residual disorder in the III-V semiconductors will compensate the electrical activity of dopants. (Residual damage in GaN has the nature of n-type conductivity due to more N displaced). Carrier activation does not occur until most of the implant damage is removed. Provided that the material is not annealed at high enough temperature to remove these defects, then it is in highly resistive state. It has been demonstrated that for most semiconductors, the implant activation temperature generally follows a two-thirds rule with respect to the melting point.⁶⁹ For GaN ($T_m > 2200$ °C), although good dopant activation can be achieved at 1100 °C, the optimum annealing temperature may be very well closer to 1700 °C to fully remove the implant damage.⁷⁰ Annealing conditions consisting of a high temperature, short duration (1-30 seconds) is desirable for III-V materials, which can give good electrical properties in the implanted layer, and restrict surface degradation, dopants redistribution and mobility degradation in device structures. However, the temperatures required for GaN and other wide bandgap compound semiconductors are beyond the capability of most rapid thermal annealing systems, which typically rely on a series of tungsten-halogen lamps as heat sources to rapidly heat up the wafers. New annealing apparatus must be developed to optimize GaN processing techniques.

In III-V semiconductors, the post-implant annealing temperature required to activate the dopant or remove the damage always exceeds that at which the surface of material is degraded by the loss of group V element (N for GaN). Some forms of surface protection must be provided. With conventional III-V materials such as GaAs and InP this is achieved in several ways: (1) capless proximity annealing, in which the wafer is placed face-to-face with another wafer of the same type, so that the onset of preferential As or P loss quickly suppresses further loss. The disadvantages of this method include the fact that some group V atoms are lost from the near surface. There is also a possibility of mechanical abrasion of the face of the sample of interest, and contamination transferred from the dummy wafer. Despite these drawbacks, it is still the most commonly used method in III-V research. (2) placing the wafer in a SiC-coated graphite susceptor, which either has had its internal surfaces coated with As or P by heating a sacrificial wafer in it, or in which granulated or powdered GaAs or InP is placed in reservoirs connected to the region in which the wafer is contained. In both cases subsequent heating of the susceptor produces an As or P vapor pressure above the surface of the process wafer, suppressing loss of the group V element. This approach is widely used in industry for GaAs and to a less extent InP. Since the susceptors are essentially black-body radiators and do not have temperature differentials between center and edge of the wafer, the crystallographic slip on large III-V wafers during annealing can be avoided. In the conventional geometry, the very rapid heating and cooling during RTA could induce substantial crystallographic slip due to generation of thermal stresses by radiative losses around the edges of the wafer. (3) encapsulation of the wafer with a dielectric film which has similar expansion coefficient. A protection film with quite different thermal properties could introduce

considerable near-surface strain, which can lead to a significant enhancement in the diffusivity of some implanted dopants.

The equilibrium N₂ pressure over GaN at 1400 °C is >1000 bar,⁷¹ and at that temperature only two methods have proven effective in preventing surface decomposition: using of high N₂ pressure (15 kBar)⁷² and deposition of AlN encapsulation layers⁷³ (the equilibrium N₂ pressure above AlN is only 10⁻⁸ bar at 1400 °C, and the activation energy of N₂ loss for AlN is larger than that for GaN). AlN has similar thermal expansion coefficients with GaN, and can be selectively removed in KOH solution.⁷⁴

2.3 Metal/Semiconductor Contacts

2.3.1 Schottky Contact

When metal is making intimate contact with a semiconductor, the Fermi levels in the two materials must be coincident at thermal equilibrium. This can be achieved through a charge flow from semiconductor to metal. Thus a barrier forms at the interface and an equal and opposite space charge is distributed over the barrier region near the semiconductor surface. With an n-type semiconductor in the absence of surface state, the barrier height $q\phi_{bn}$ is given by:

$$q\phi_{bn} = q(\phi_m - \chi) \quad (2.3)$$

where $q\phi_m$ is the metal work function, $q\chi$ is the electron affinity of the semiconductor.

For an ideal contact between metal and a p-type semiconductor, the barrier height $q\phi_{bp}$ is given by:

$$q\phi_{bp} = \varepsilon_g - q(\phi_m - \chi) \quad (2.4)$$

When surface states are present on the semiconductor surface, and the density is sufficiently large to accommodate any additional surface charges without appreciably altering the occupation level E_F , the space charge in the semiconductor will remain unaffected. As a result, the barrier height is determined by the property of the semiconductor surface, and is independent of the metal work function. In practice, some surface states always present at the semiconductor surface, and continuously distributed in energy within the energy gap. The Schottky barrier heights of metal–semiconductor systems with intimate contact are, in general, determined by both the metal work function and the surface states.

In a simple model for all semiconductors, the Schottky barrier height $q\phi_b$ can be expressed as:⁷⁵

$$q\phi_b = q(S\chi_m + \phi_0) \quad (2.5)$$

where χ_m is metal electronegativity, ϕ_0 represents the contribution of surface states of semiconductors, and interface index $S = \frac{d\phi_b}{d\chi_m}$, is found to be a function of the electronegativity difference $\Delta\chi$ between cation and anion of compound semiconductor, as shown in Fig. 2.2 (a). Note a sharp transition around $\Delta\chi=1$. For ionic semiconductors, $\Delta\chi>1$, the index S approaches 1, and ϕ_b is strongly dependent of the metal electronegativity (or work function). On the other hand, for covalent semiconductors with $\Delta\chi<1$, S is small, ϕ_b is affected by high density surface states from dangling bonds and only weakly depends on metal work function. GaN has an electronegativity difference of 1.4 (Ga: 1.6, N: 3.0), which would predict the Schottky barrier heights depend on metal work function, and are given by eq. 2.3 and eq. 2.4 for metal on n-type and p-type

material respectively. A summary of reported Schottky barrier heights of a variety of elemental metals on n-GaN is shown in Fig. 2.2 (b).⁵⁴ It is clear that the barrier height indeed varies with the metal work function within experimental scattering.

The current transport in metal-semiconductor contacts is mainly due to majority carrier, in contrast to p-n junctions. Two major processes under forward bias are (1) transport of electrons from the semiconductor over the potential barrier into the metal; (2) quantum-mechanical tunneling of electrons through the barrier. In addition, we may have recombination current in the space-charge region and leakage current at the contact periphery. The transport of electrons over the potential barrier is often the dominant process for Schottky diodes on moderately doped semiconductors. It can be adequately described by thermionic emission theory for high mobility semiconductor (for low mobility materials, the diffusion theory is also applicable), and the electric current density over the barrier has the following expression:

$$J = J_s [\exp\left(\frac{qV}{kT}\right) - 1] = A^{**} T^2 \exp\left(-\frac{q\phi_b}{kT}\right) [\exp\left(\frac{qV}{kT}\right) - 1] \quad (2.6)$$

where J_s is the saturation current density, A^{**} is the effective Richardson constant. In practical device, the barrier height dependent on bias voltage, and the current-voltage characteristics is more accurately described by:

$$J = A^{**} T^2 \exp\left(-\frac{q\phi_b}{kT}\right) [\exp\left(\frac{qV}{nkT}\right) - 1] \quad (2.7)$$

Factor n is called the ideality factor. The barrier height and ideality factor can be obtained from the forward J-V characteristics (for $V > 3kT/q$):

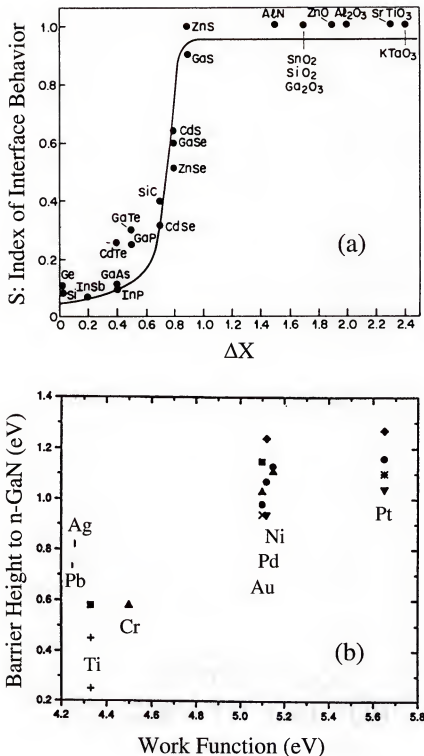


Fig. 2.2 (a) Index of interface behavior S as a function of the electronegativity difference of the semiconductors. (b) Barrier height versus work function of metals deposited on n-GaN reported from various groups.

$$n = \frac{q}{kT} \frac{\partial \mathcal{V}}{\partial \ln J} \quad (2.8)$$

$$\phi_b = \frac{kT}{q} \ln\left(\frac{A^{**}T^2}{J_s}\right) \quad (2.9)$$

For a heavily doped semiconductor or for operation at low temperatures, the tunneling current may become the dominant transport process. The tunneling current has an expression:

$$J_t \sim \exp\left(\frac{2\phi_b}{\hbar} \sqrt{\frac{\epsilon_s m^*}{N_D}}\right) \quad (2.10)$$

where ϵ_s is permittivity of semiconductor, m^* is effective mass of carrier, N_D is carrier concentration. It indicates the current will increase exponentially with $N_D^{0.5}$.

2.3.2 Ohmic Contact

It is imperative that a semiconductor device be connected to the outside world with no adverse change to its current-voltage characteristics. This can be accomplished through ideal ohmic contacts to the semiconductor. An ohmic contact is defined as a metal/semiconductor contact that has negligible contact resistance relative to the bulk or spreading resistance of the semiconductor. A satisfactory ohmic contact can supply the required current with a voltage drop that is sufficiently small compared with the drop across the active region of the devices. One important figure of merit for ohmic contact is specific contact resistance r_c , which is defined as:

$$r_c = \left(\frac{\partial J}{\partial V}\right)_{V=0}^{-1} \quad (2.11)$$

For contact with lower doping concentration, at relatively high temperature, conduction across the M/S interface is dominated by thermionic-emission over the potential barrier, as given in eq. 2.6. Therefore,

$$r_c = \frac{k}{qA^{**}T} \exp\left(\frac{q\phi_b}{kT}\right) \quad (2.12)$$

It is obvious that low ϕ_b should be used for small r_c . Ideally a metal with a lower work function than an n-type semiconductor or higher work function than a p-type semiconductor should be used for ohmic contact to this semiconductor. Unfortunately, very few practical material systems satisfy this condition, and metals usually form Schottky barriers at semiconductor interface. A practical way to obtain a low resistance ohmic contact is to create a highly doped region near the surface by ion implantation, or increase the doping by alloying the contacts. In this case, the depletion layer cause by the Schottky barrier becomes very thin, and current transport through the barrier is enhanced by tunneling. The contact resistance can be obtained from eq. 2.10,

$$r_c \sim \exp\left(\frac{2\sqrt{\epsilon_s m^*} \phi_b}{\hbar \sqrt{N_D}}\right) \quad (2.13)$$

Note that r_c depends strongly on N_D . Under intermediate conditions, thermionic field emission is important, where there is enough kinetic energy for the carrier to be excited to an energy level at which the potential barrier is thin enough for tunneling to occur. Typical ohmic conduction is usually related to a large tunneling component.

The resistance of ideal planar contacts may be found using a transmission-line method (TLM). This technique is based on the assumption that specific contact resistance is determined by either the metal-semiconductor interface or by the interface between the alloyed and nonalloyed portions of the active layer, and that the semiconductor resistivity

under the contact is uniform (though it may be different from that outside the contact).

The typical TLM pattern used for the measurements is shown in Fig. 2.3 (a). The resistance between two adjacent pads of width W and length d separated by distance L is given by:

$$R = R_s L/W + 2R_c \quad (2.14)$$

where R_s is the sheet resistance of the active layer between the contacts (i.e. the film resistance per square), R_c is the contact resistance. The values of R_c and R_s are determined from the intercept and the slope of the R vs. L curve, as shown in Fig. 2.3 (b).

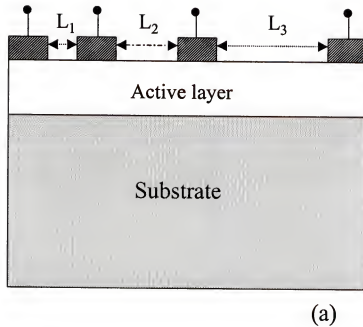
In the simple case of nonalloyed contacts, where the sheet resistance of the active layer under the contacts is equal to R_s , the specific contact resistance r_c may be determined from R_c and R_s using equations of the transmission-line model:⁷⁶

$$R_c = R_s (L_T/W) \coth(d/L_T) \quad (2.15)$$

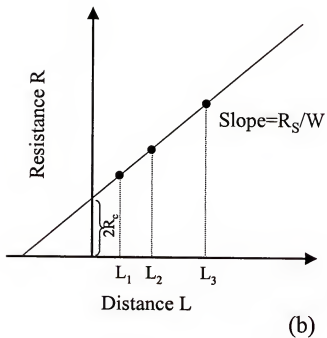
where $L_T = (r_c/R_s)^{1/2}$ is called the transfer length. For $d/L_T \gg 1$, we obtain:

$$r_c = \frac{R_c^2}{R_s} W^2 \quad (2.16)$$

The TLM method is not accurate for specific contact resistances near and below $10^{-7} \Omega \cdot \text{cm}^2$, in which case the Kelvin probe measurements can be employed. In the four-terminal (Kelvin) resistor method,⁷⁷ the test pattern consists of four metal pads on an insulator. Two are connected to a semiconductor bar by means of large-area contacts. The other two touch the semiconductor at the contact opening. In contrast to the TLM case, the resistance of the line outside the contact area does not contribute to the contact resistance of this test structure. This allows a more precise measurement of a very small contact resistance.



(a)



(b)

Fig. 2.3 Determination of contact and sheet resistance using the TLM measurements: (a) TLM pattern (b) resistance between the contact pads (width W) vs. distance between the contacts.

It is difficult to make ohmic contacts on wide-bandgap semiconductors, such as GaN ($\epsilon_g=3.4$ eV, $\chi=4.1$ eV) and SiC. Generally the doping concentration is relatively low due to the high ionization level of typical dopants. A metal does not have high enough work function to yield a low barrier on p-type material ($q\phi_m < 5$ eV for most metals). In addition, the tendency to lose N during thermal processing which would contribute to n-type conductivity makes the achievement of low-resistance ohmic contacts on p-GaN particularly challenging. Other techniques for making an ohmic contact should be explored, involving the establishment of a heavily doped surface layer by interface reaction, alloys regrowth, or deposition of strained-layer superlattices and graded materials to eliminate the barrier over the thickness of the contact layer.

2.4 Dry Etching

Wet chemical etching enjoys many advantages for device fabrication, including simplicity, high selectivity, high throughput, low cost and low damage to the wafer. However, its isotropic nature, which results in roughly equal removal of material in all directions, makes it incapable of patterning submicron features. Dry etching, which provides higher resolution potential by overcoming the problem of isotropy, has become a favorable etching technique for VLSI/ULSI technology. In addition, it offers advantages such as superior uniformity and compatibility with multichamber processing. Especially for III-V nitrides, due to the lack of efficient wet etch recipes, dry etching has become the dominant patterning technique.

Dry plasma etching proceeds by either physical sputtering, chemical reaction, or a combination of the two often referred to as ion-assisted plasma etching. Physical

sputtering is dominated by the acceleration of energetic ions formed in the plasma to the substrate surface at relatively high energies, typically >200 eV. Due to the transfer of energy and momentum to the substrate, material is ejected from the surface. This sputtering mechanism tends to yield anisotropic profiles. However it can result in rough surface morphology, trenching, poor selectivity and nonstoichiometric surfaces thus minimizing device performance. The etching rates are sensitive to the magnitude of bonding force and structure of the surface, and typically quite slow.

Chemically dominated etch mechanisms rely on the formation of reactive species in the plasma which adsorb to the surface, form volatile etch products, and then desorb from the surface. Since ion energies are relatively low, etch rates in the vertical and lateral direction are often similar thus results in isotropic etch profiles and loss of critical dimensions. However, good etch rate and selectivity can be achieved, and the plasma-induced damage is minimized.

The chemical etching is rapid, but isotropic, whereas the physical etching is slow, but anisotropic. Provided the chemical and physical components of the etch mechanism are balanced, high-resolution features and high etch rates with minimal damage can be realized. This ion-assisted plasma etching is the typical mechanism of most current dry etching techniques.

Reactive ion etching (RIE) is one of the dry etching techniques in common usage, which utilizes both the chemical and physical components of an etch mechanism. RIE plasmas are typically generated by applying radio frequency (rf) power of 13.56 MHz between two parallel electrodes in a reactive gas (see Fig. 2.4(top)). The sample to be etched is placed on the powered electrode where a potential is induced, and is subject to

the ion bombardment and impingement of neutral gas atoms and molecules from the plasma. Ion energies, defined as they cross the plasma sheath, are typically a few hundred eV. Etching is typically performed at low pressures, ranging from a few mTorr up to 200 mTorr, which promotes anisotropic etching due to increased mean free paths and reduced collisional scattering of ions during acceleration in the sheath. RIE is by far the most popular dry etching technique used for conventional III-V materials, and takes advantage of the fact that there is a synergism between the physical and chemical etching mechanisms. The observed etch rates are faster than the sum of these two components. This is usually ascribed to the fact that the volatile etch products formed by chemisorption of active species from the plasma onto the semiconductor surface are quickly removed by physical sputtering, exposing a fresh layer of the material. Good results for the III-V nitrides have been obtained in chlorine-based plasma under high ion energy conditions where the III-N bond breaking and the sputter desorption of etch products are most efficient. Unfortunately, the high energy plasma may induce significant damage and degrade both electrical and optical device performances. Lowering the ion energy and increasing the chemical activity in the plasma often results in much slower etch rates and less anisotropic profiles. It is necessary to pursue alternative etch platforms which combine high quality etch characteristics with low damage for III-V nitrides.

The use of high-density plasma etch systems, such as inductively coupled plasma (ICP)⁶¹ and electron cyclotron resonance (ECR)⁶³, has resulted in improved etch characteristics for the III-V nitrides as compared to RIE. This observation is attributed to plasma densities which are 2-4 orders of magnitude higher than RIE thus improving the III-N bond breaking efficiency and the sputter desorption of etch products for the surface.

Additionally, since ion energy and ion density can be more effectively decoupled, plasma induced damage is more readily controlled. Fig. 2.4 (bottom) shows a schematic diagram of a typical ICP etch system. High density ICP plasmas are formed in a dielectric vessel encircled by an inductive coil into which rf power is applied. The alternating electric field between the coils induces a strong alternating magnetic field trapping electrons in the center of the chamber and generating plasmas with uniform density and energy distribution. By keeping ion and electron energy low, we can obtain low damage etching while maintaining fast etch rates. Anisotropy is achieved by superimposing a rf bias on the sample. Generally, etch characteristics are dependent upon plasma parameters including ion energy (controlled by rf chuck power), plasma density (controlled by ICP source power), and operation pressure (the change in collisional frequency can result in changes in both ion energy and plasma density). Compared to ECR, where high-density plasmas are formed through magnetic confinement of electrons in the source region, ICP etching is generally believed to have several advantages including easier scale-up for production, improved plasma uniformity and lower cost of operation.

It is important to choose appropriate plasma chemistries to achieve good etch rates, anisotropy, selectivity, and morphology. The fragmentation pattern and gas-phase kinetics associated with the source gas can have a significant effect on the concentration of a reactive neutrals and ions generated in the plasma thus affecting the etch characteristics. Secondary gases such as Ar, N₂, H₂, or SF₆ can be added to change the chemical : physical ratio of the etch mechanism, and therefore achieve better profiles or higher rates. Another important factor affecting the etch characteristics is the volatility of the etch products formed. Table 2.1 shows the boiling points of possible etch products for

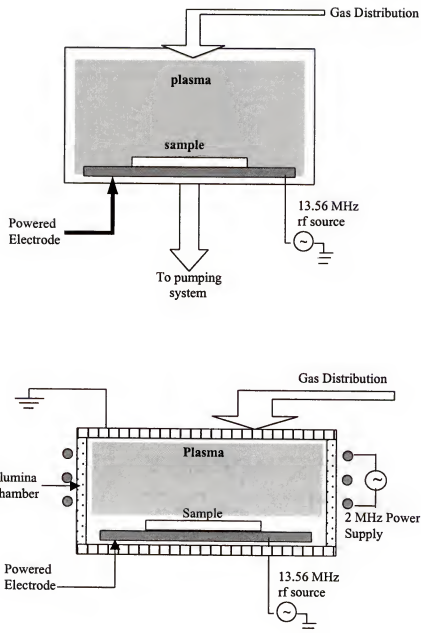


Fig. 2.4 Schematic diagram of RIE (top) and ICP (bottom) etch systems.

Table 2.1 Boiling points for possible etch products of III-V nitrides etched in halogen- or CH₄/H₂-based plasmas.

Etch products	Boiling point (°C)
AlCl ₃	183
AlF ₃	Na
AlI ₃	360
AlBr ₃	263
(CH ₃) ₃ Al	126
GaCl ₃	201
GaF ₃	1000
GaI ₃	Sublimes 345
GaBr ₃	279
(CH ₃) ₃ Ga	55.7
InCl ₃	600
InF ₃	>1200
InI ₃	Na
InBr ₃	Sublimes
(CH ₃) ₃ In	134
NCl ₃	<71
NF ₃	-129
NBr ₃	Na
NI ₃	Explodes
NH ₃	-33
N ₂	-196
(CH ₃) ₃ N	-33

III-V nitrides exposed to halogen- and hydrocarbon-based plasmas. For halogen-based plasmas, etch rates are often limited by the volatility of the group III halogen etch products. Cl-based plasmas typically yield fast rates with anisotropic, smooth etch profiles for Ga- and Al-containing films. In a contrast, etch rates for In-containing

materials in room temperature Cl-based plasmas tend to be slow with rough surface morphology and overcut profiles due to the low volatility of InCl_3 and preferential loss of the group V etch products. Significant better room temperature etch results are obtained in CH_4/H_2 -based plasma due to the formation of more volatile $(\text{CH}_3)_3\text{In}$.⁶³ Based only on Table 2.1, high etch rates can also be expected for Ga-containing films in CH_4/H_2 -based plasmas since the $(\text{CH}_3)_3\text{Ga}$ has a much lower boiling point than GaCl_3 . However, in practice very slow rates are observed, which demonstrates the complexity of the etch process where redeposition, polymer formation, and gas-phase kinetics can influence the results.

CHAPTER 3

ULTRA-HIGH TEMPERATURE ACTIVATION OF IMPLANT DOPING IN GaN

3.1 Introduction

Ion implantation is an enabling technology for selected-area doping or isolation of advanced semiconductor devices. Implantation of donors at high doses can be used to decrease source and drain access resistance in FETs, at lower doses to create channel regions for FETs, while sequential implantation of both acceptors and donors may be used to fabricate p-n junctions. In addition, ion implantation is a suitable technological tool to explore doping, compensation effects, and redistribution properties of the potential dopant species.

The first work on implantation in GaN was performed by Pankove and co-workers in the earlier 1970s.⁷⁸ They reported primarily on the photoluminescence properties of a large array of implanted impurity in GaN. The work was successful in identifying Mg as the shallowest acceptor found to date for GaN. In 1995, Pearton et al.³⁰ achieved electrically active n- and p-type dopants in GaN by implantation of Si and Mg respectively. Subsequently, implanted O was shown to also be a donor and implanted Ca an acceptor in GaN.³¹ Two different GaN based device structures have been demonstrated using implant doping, namely a junction field effect transistor⁴⁶ and a planar homojunction LED.⁷⁹

Tan et al.⁸⁰ have observed that low dose ($\leq 5 \times 10^{14} \text{ cm}^{-2}$) implants in GaN anneal poorly up to 1100 °C, leaving a coarse network of extended defects, while high dose (\geq

$2 \times 10^{15} \text{ cm}^{-2}$) implants may lead to amorphization. Amorphous layers recrystallize in the range 800-1000 °C to form defective polycrystalline material. Quite good activation efficiencies have been obtained for n-type implanted dopants in spite of high residual damage.^{30,51} It is also clear that annealing temperatures above 1300 °C are desirable for optimal electrical properties in the implanted layers.⁵¹ At these temperatures, the equilibrium N₂ pressure over GaN is very high, thus surface protection is necessary to prevent dissociation of the GaN. The most effective and convenient approach is use of an AlN encapsulant that can be removed selectively in KOH after annealing. This technique is attractive for processing of GaN devices in a conventional fabrication-line environment, without the need for specialized high-pressure furnaces.

In this chapter we first introduced a novel rapid thermal processing (RTP) up to 1500 °C to the GaN material system, used in conjunction with AlN cap layers. The high temperature activation characteristics of implanted Si and Group VI donors were then examined. The activation of Mg, Be and C for p-type doping has also been investigated, along with the redistribution of all these species in GaN. Finally the effectiveness of the new RTP for removing lattice damage in implanted GaN was studied by TEM.

3.2 High Temperature Annealing and AlN Encapsulation

In the development of advanced electronic devices, the technology of rapid thermal processing plays a critical role at numerous points such as implant activation of dopant species, implantation-induced damage removal, alloying of ohmic contacts, maximization of sheet resistance in implant isolation regions, etc. The existing commercial RTP equipment typically relies on a series of tungsten-halogen lamps as heat sources to

rapidly heat up the semiconductor wafers, and only has modest temperature capacity (<1100 °C), primarily because of the point-like nature of the sources and large thermal mass of the systems. Recent interest in developing wide bandgap compound semiconductors such as SiC and GaN has pushed the processing temperature requirements to much higher values (up to 1500 °C).

To meet thus an urgent need, MHI Inc., in collaboration with the University of Florida, has recently developed a unique high temperature RTP unit called Zapper™, which can achieve such high processing temperatures. To realize higher temperature capacity, novel molybdenum intermetallic composite heat sources have been employed, which may be used in air at temperatures up to 1900 °C. These heaters have high emissivity (up to 0.9) and allow heat-up time of the order of seconds and heat fluxes up to 100 W/cm². The Zapper™ unit relies on wafer movement (in/out of the furnace horizontally) to achieve rapid ramp-up or ramp-down rates (~50 °C /s and 25 °C /s respectively). Excellent temperature uniformity ($\leq \pm 4$ °C over a 9×6" area at 1500 °C), good reproducibility can be obtained. Fig. 3.1 shows the typical temperature-time profiles for an annealing cycle at 1400 °C and 1500 °C.

To examine the thermal stability of the nitrides, a variety of undoped GaN and AlN wafers were sealed in quartz ampoules under N₂ gas, and annealed in Zapper™ unit at different time-temperature combinations. The GaN layers ~ 3 μm thick were grown at ~1050 °C by MOCVD using trimethylgallium and ammonia. Growth was preceded by low-temperature deposition of thin (~200 Å) AlN buffers on Al₂O₃ substrates. Some AlN layers were deposited by reactive sputtering of pure AlN targets in 300 mTorr of 20% N₂Ar at 400 °C. The others were grown by metal organic molecular beam epitaxy

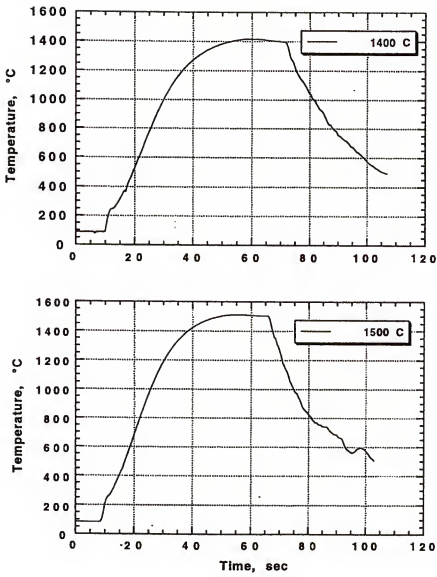


Fig. 3.1 Time-temperature profiles for Zapper™ RTP annealing at 1400 °C and 1500 °C.

(MOMBE) at 750 °C using dimethylamine alane and plasma dissociated nitrogen.⁸¹ The N₂ pressure in the quartz ampoules was ~15 psi. This negative pressure was necessary to prevent blowout of the ampoule at elevated annealing temperatures. The samples were then annealed at 1100 °C – 1500 °C for a dwell time of ~10 s.

Fig. 3.2(top) shows scanning electron microscopy (SEM) micrographs of the GaN surfaces annealed at 1200 -1500 °C. The 1200 °C annealing does not degrade the surface, and the sample retains the same appearance as the as-grown material. After 1300 °C annealing, there is a high density ($\sim 10^8$ cm⁻²) of small hexagonal pits due to incongruent evaporation from the surface. The 1400 °C treatment produces complete dissociation of the GaN, and only the underlying AlN buffer survives. Annealing at 1500 °C also causes loss of this thin buffer layer, and a smooth exposed Al₂O₃ substrate is evident. The corresponding root-mean-square (RMS) surface roughness of these samples measured by atomic force microscopy (AFM) scans is shown in Fig 3.2 (bottom).

In sharp contrast, both the sputtered and MOMBE-grown AlN were found to survive annealing up to 1400-1500 °C. However, for the sputtered materials, we often observed localized failure of the film (Fig 3.3(top)), possibly due to residual gas (Ar or H₂) agglomeration to form bubbles. The surface roughness tends to go through a maximum at ~ 1300 °C, partially due to some initial localized bubbling, followed by the film densification at temperatures \geq 1400 °C, as shown in Fig. 3.3 (bottom). The film retains its integrity even at 1450 °C, and appears to be more thermally stable than the AlN buffer layer under the GaN (Fig. 3.2). This can be attributed to the fact that the AlN was deposited at higher temperature (400 °C compared to 300 °C for the buffer layers) and

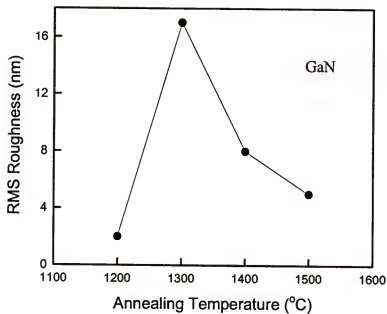
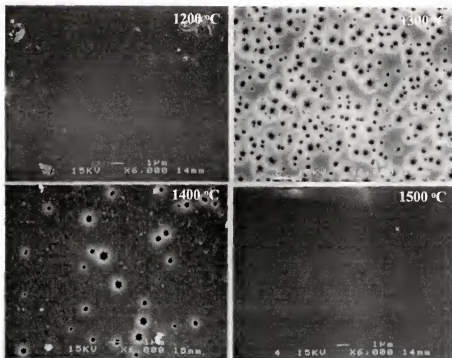


Fig. 3.2 SEM micrographs (top) and RMS roughness (bottom) of GaN surfaces annealed at 1200 -1500 °C.

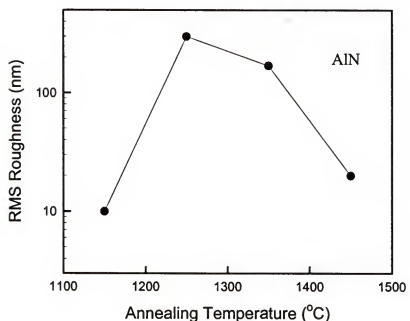
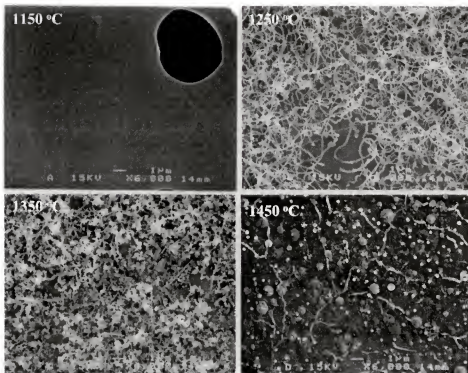


Fig. 3.3 SEM micrographs (top) and RMS roughness (bottom) of AlN surfaces annealed at 1150 -1450 °C.

therefore is denser and contains less residual entrapped gas. For the MOMBE grown films, the localized material failure was basically absent.

There is clear evidence from previous work that temperatures above 1300 °C are required to completely remove implantation damage and to achieve the optimal dopant activation in GaN. However, the above results show that a premium is placed on prevention of loss of nitrogen or even surface dissociation under those conditions. AlN encapsulation can preserve the surface quality to 1500 °C, which is quite promising for the high temperature activation processes.

3.3 N-type Implant Doping

Nominally undoped ($n \sim 5 \times 10^{16} \text{ cm}^{-3}$) GaN was grown on c-plane Al_2O_3 substrates MOCVD. Samples were implanted at room temperature in a non-channeling direction with 150 keV $^{28}\text{Si}^+$ ions at a dose of $5 \times 10^{15} \text{ cm}^{-2}$, 200 keV $^{32}\text{S}^+$ and 600 keV $^{128}\text{Te}^+$ ions at doses of $5 \times 10^{14} \text{ cm}^{-2}$ for n-type doping. The Si implant is a standard condition for producing very high n-type doped regions in GaN when combined with high temperature RTA. All samples were capped with $\sim 1000 \text{ \AA}$ reactively sputtered AlN, and annealed at 1200-1500 °C under a N_2 ambient in the Zapper™ furnace for a dwell time of ~ 10 secs. Following annealing, the AlN was removed in aqueous KOH at ~ 80 °C, and the samples were characterized. For measurement of the electrical properties, HgIn ohmic contacts were alloyed to the corners of $3 \times 3 \text{ mm}^2$ sections, and Hall effect data was recorded at 25 °C in all cases.

Fig. 3.4(a) shows an Arrhenius plot of sheet carrier concentration in Si^+ implanted material. As a comparison, the electrical results for the unencapsulated samples are also

shown. In these uncapped wafers, the sheet electron density increases with annealing temperature up to 1300 °C, but this was the highest temperature we would obtain data due to loss of the film. By contrast, the AlN encapsulated samples show a peak in the sheet electron density and the 300 K electron mobility (Fig. 3.4 (b)) at 1400 °C. The activation occurs with an activation energy of ~5.2 eV, which we interpret as the average required to move the interstitial Si atom to a vacant substitutional site by short-range diffusion and to simultaneously remove compensating point defects so that the Si is electrically active. Note that both the electron density and the mobility decreases at 1500 °C, indicating that the material is becoming more compensated. This behavior is fairly typical of Si implant activation in III-V materials, and is usually ascribed to self-compensation through Si site-switching, i.e. some of the Si_{Ga} donors move to Si_{N} sites, producing self-compensation. A peak Si activation efficiency of ~90% is obtained at 1400 °C (with the ionization level of ~30 meV, Si was fully ionized at room temperature), which corresponds to a peak electron concentration of $\sim 5 \times 10^{20} \text{ cm}^{-3}$. This very high doping level can enhance emission over the barrier on metal contacts deposited on the material and reduce contact resistances in GaN electronic devices.

Fig. 3.5(a) shows an Arrhenius plot of S^+ activation in GaN. The sheet carrier concentration measured at 25 °C shows an activation energy of 3.2 eV for the annealing temperature range between 1000-1200 °C, and the physical origin of this energy is essentially same as that of Si implant activation. The sheet carrier concentration is basically saturates thereafter. The maximum sheet electron density, $\sim 7 \times 10^{13} \text{ cm}^{-2}$, corresponds to a peak volume density of $\sim 5 \times 10^{18} \text{ cm}^{-3}$. This is well below that achieved with Si^+ implantation and annealing ($> 10^{20} \text{ cm}^{-3}$). Even though implanted Si^+ at the same

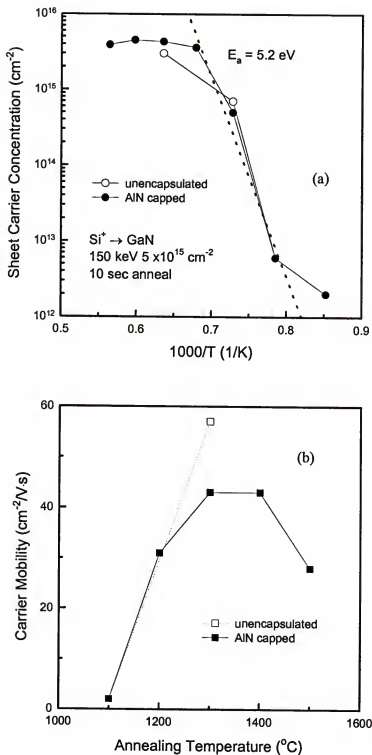


Fig. 3.4 Sheet carrier concentration (a) and electron mobility (b) in Si-implanted GaN after uncapped and AlN-capped annealing.

dose showed evidence of site-switching and self-compensation, it still produces a higher peak doping level than the non-amphoteric donor S, which is only slightly heavier (^{32}S vs. ^{28}Si). From temperature-dependant Hall measurements, we find a S^+ donor ionization level of 48 ± 10 meV, so that the donors are fully ionized at room temperature.

Similar data is shown in Fig. 3.5 (b) for Te^+ implantation. The activation starts around the same temperature as for S, but much lower sheet electron densities are obtained, the activation energy is significantly lower (1.5 eV) and the carrier concentration does not saturate, even at 1400 °C. It is likely that because of the much greater atomic weight of ^{128}Te , even higher annealing temperatures would be required to remove all its associated lattice damage, and that the activation characteristics are still being dominated by this defect removal process. Residual lattice damage from the implantation is electrically active in all III-V semiconductors, producing either high resistance behaviors (GaAs) or residual n-type conductivity (InP, GaN). The only data available on group VI doping in epitaxial material is from Se-doped MOCVD material, where maximum electron concentrations of $2\times10^{18} - 6\times10^{19} \text{ cm}^{-3}$ were achieved.⁸² These are also below the values reported for Si-doping, and suggests the group VI donors do not have any advantage over Si for creation of n-type conductivity in GaN. From limited temperature-dependent Hall data, we estimate the Te ionization level to be 50 ± 20 meV.

3.4 P-type Implant Doping

Similar GaN samples were implanted with 80 keV $^9\text{Be}^+$, 80 keV $^{12}\text{C}^+$, or 150 keV $^{24}\text{Mg}^+$ at doses of $3\text{-}5\times10^{14} \text{ cm}^{-2}$ for p-type doping. Post-implant annealing was

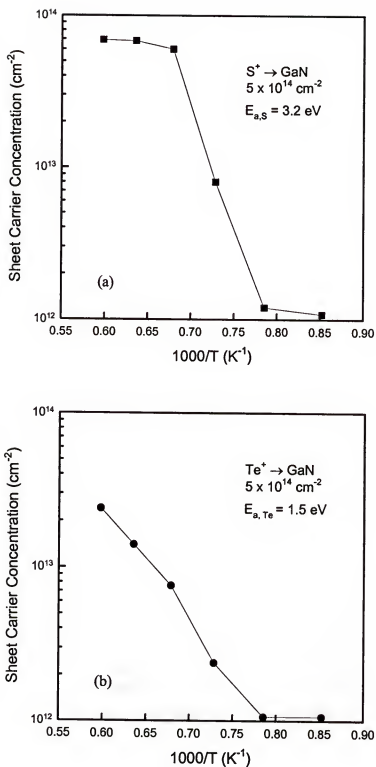


Fig. 3.5 Arrhenius plots of sheet electron density in S (a) and Te (b) implanted GaN as a function of annealing temperature.

performed at 1000-1400 °C under a N₂ ambient in the ZapperTM furnace for ~10 secs in conjunction with ~1000 Å AlN encapsulation.

The effects of the annealing temperature on the sheet carrier concentrations in Mg⁺ and C⁺ implanted GaN are shown in Fig. 3.6. There are two important features of the data: first, we did not achieve p-type conductivity with carbon, and second only ~1% of the Mg produces a hole at 25 °C. Carbon has been predicted previously to have a strong self-compensation effect,⁸³ and it has been found to produce p-type conductivity only in metal organic molecular beam epitaxy where its incorporation on a N-site is favorable.⁸⁴ Based on an ionization level of ~170 meV, the hole density in Mg-doped GaN would be calculated to be ~10% of the Mg acceptor concentration when measured at 25 °C. In our case we see an order of magnitude less holes than predicted. This should be related to the existing n-type carrier background in the material and perhaps to residual lattice damage which is also n-type in GaN. At the highest annealing temperature (1400 °C), the hole density falls, which could be due to Mg coming out of the solution or to the creation of further compensating defects in the GaN. The results of Be implant are similar with those of C implant, i.e. remaining n-type after annealing, probably also due to a strong compensation effect. This data indicates that ion implantation is not so efficient for creating p-type conductivity in state-of-the-art GaN as epitaxial growth doping.

3.5 Dopant Redistribution

Fig. 3.7 shows the calculated, as-implanted Si atomic profile, and the secondary ion mass spectroscopy (SIMS) profiles of as-implanted and 1400 °C annealed samples. The calculated profile does not produce a good match to the experimental profile, and some

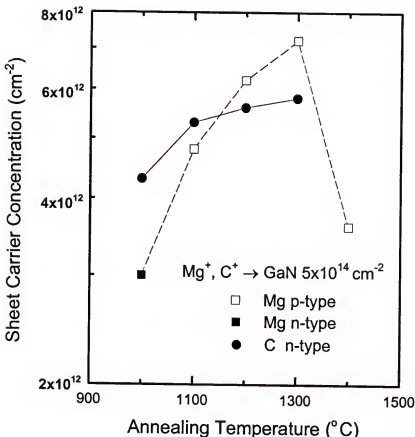


Fig. 3.6 Sheet carrier concentrations in Mg^+ and C^+ implanted GaN as a function of annealing temperature.

work will need to be done to obtain better stopping power data for the ions in GaN. There is little redistribution of the Si at 1400 °C, with the diffusivity $\leq 10^{-13} \text{ cm}^2 \cdot \text{sec}^{-1}$ calculated from the change in width at half-maximum. This result emphasizes the extremely stable nature of Si dopant in GaN even at very high processing temperatures.

Fig. 3.8 (top) shows SIMS profiles before and after 1450 °C annealing of implanted S in GaN. There is clearly no motion of the sulfur under these conditions and the profiles

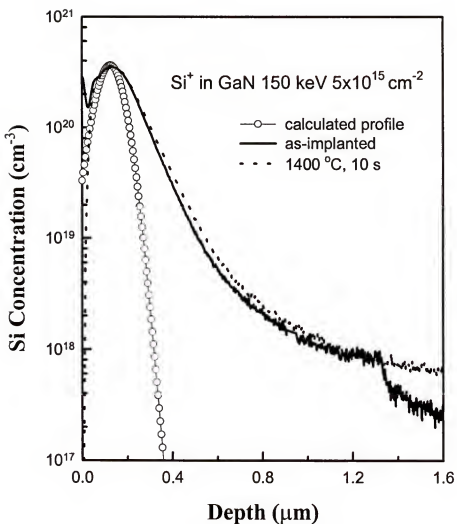


Fig. 3.7 Calculated and experimentally measured (by SIMS) profiles of implanted Si (150 keV, $5 \times 10^{15} \text{ cm}^{-2}$) in GaN.

are essentially coincident. Wilson⁸⁵ reported some redistribution of implanted S after annealing at 700-1000 °C in relatively thin layers of GaN, which might have been influenced by the high crystalline defect density in the material. The samples in the present experiment are much thicker and the extended defect density will be correspondingly lower in the implanted region ($\sim 5 \times 10^8 \text{ cm}^{-2}$ compared to $\sim 10^{10} \text{ cm}^{-2}$ in the thin samples). The other group VI donors, Se and Te, have low diffusion coefficients in all compound semiconductors (for example $D_{\text{Se}} = 5 \times 10^{-15} \text{ cm}^2 \cdot \text{sec}^{-1}$ at 850 °C in GaAs),⁶⁴ and we find a similar result for these species implanted into GaN, as shown in Fig. 3.8 (bottom). Given the resolution of SIMS measurement ($\sim 200 \text{ \AA}$ under these conditions), we can obtain the diffusivity at this temperature $\leq 2 \times 10^{-13} \text{ cm}^2 \cdot \text{sec}^{-1}$ using a simple $2\sqrt{Dt}$ estimation.

Fig. 3.9 (top) shows SIMS profile of implanted Mg in GaN, both before and after annealing at 1450 °C. Again, within the resolution of SIMS, there is no motion of the Mg. This is in sharp contrast to its behavior in GaAs,^{86,87} where the rapid diffusion of the Ga-site acceptors during annealing can only be suppressed by co-implanting a group V element to create a sufficient number of vacant sites for the initially interstitial acceptor ions to occupy upon annealing. This reduces the effective diffusivity of the acceptor and increases its electrical activation. In addition, implanted Mg in GaAs often displays out-diffusion toward the surface (in most case up, rather than down, the concentration gradient), leading to loss of dopant into the annealing cap.⁸⁸ This has been suggested to be due to non-equilibrium levels of Ga interstitials created by the implantation process. This mechanism is clearly absent for implanted Mg in GaN.

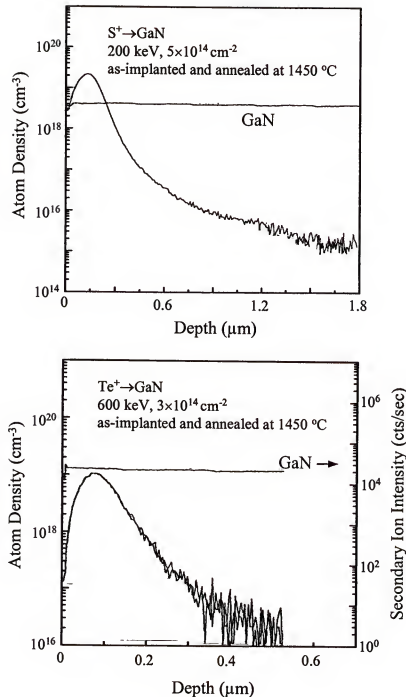


Fig. 3.8 SIMS profiles of S^+ (top) and Te^+ (bottom) implanted GaN before and after annealing at 1450 °C (the profiles are essentially coincident).

Carbon is typically a very slow diffuser in all III-V compounds, since it strongly prefers substitutional lattice sites.^{88,89} In general carbon occupies both Ga and N sites in GaN, and the material containing high concentrations of carbon is found to be self-compensated. Fig. 3.9 (bottom) shows that it is also an extremely slow diffuser when implanted into GaN, with $D_{\text{eff}} \leq 2 \times 10^{-13} \text{ cm} \cdot \text{sec}^{-1}$ at 1400 °C.

Fig. 3.10 shows a series of profiles for ⁹Be before and after annealing up to 1200 °C. Note that there is an initial broadening of the profile at 900 °C, corresponding to an effective diffusivity of $\sim 5 \times 10^{-13} \text{ cm}^2 \cdot \text{sec}^{-1}$ at this temperature. However there is no subsequent redistribution at temperatures up to 1200 °C. It appears that in GaN, the interstitial Be undergoes a type of transient-enhanced diffusion until these excess point defects are removed by annealing, at which stage the Be is basically immobile. Implanted Be shows several types of anomalous diffusion in GaAs, including up-hill diffusion and movement in the tail of the profile, in addition to normal concentration-dependent diffusion,⁹⁰ which also result from the non-equilibrium concentrations of point defects created by the nuclear stopping process of the implanted ions.

The above results show that most of the common acceptor and donor species implanted into GaN, with the exception of Be, are extremely slow diffusers at high temperatures. This bodes well for the fabrication of GaN-based power devices such as thyristors and insulated gate bipolar transistors that will require creation of doped well or source/drain regions by implantation. The low diffusivities of implanted dopants in GaN means that junction placement should be quite precise and there will be less problems with lateral diffusion of the source/drain regions towards the gate. In addition, these results also show the effectiveness of the AlN cap in protecting the GaN surface from

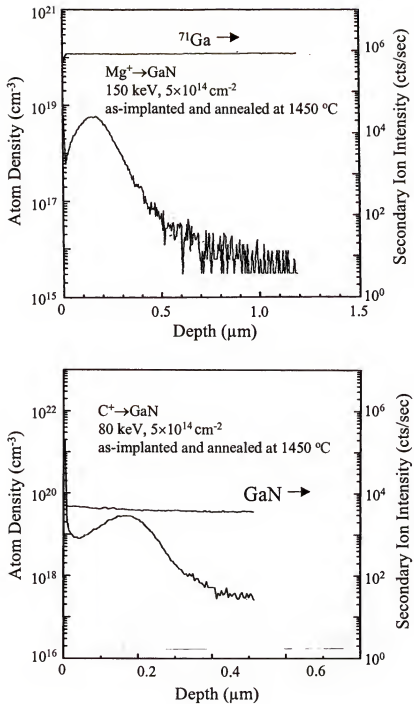


Fig. 3.9 SIMS profiles of Mg^+ (top) and C^+ (bottom) implanted GaN before and after annealing at 1450°C (the profiles are essentially coincident).

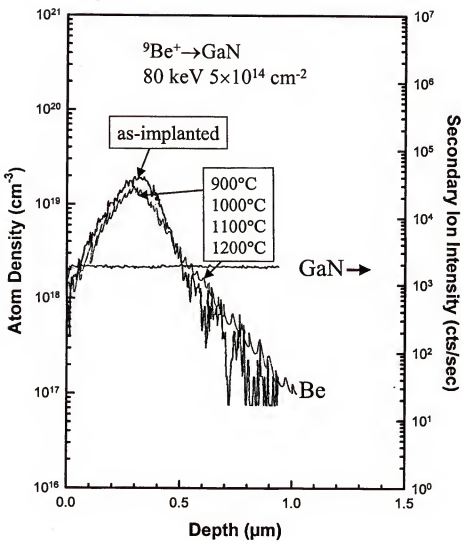


Fig. 3.10 SIMS profiles of Be^+ implanted GaN before and after annealing at different temperatures.

dissociation, since if any of the surface was degraded during annealing, the implant profiles would no longer overlap.

3.6 Residual Damage

Fig. 3.11 shows a plan view TEM and selected area electron diffraction pattern from a Si-implanted sample (150 keV, $5 \times 10^{15} \text{ cm}^{-2}$) after annealing at 1100 °C for 10 secs. This is a high dose implant of the type used for making n^+ ohmic contact regions, and represents a worst-case scenario in terms of damage removal. It also allows comparison to damage expected with other dopants such as S, Ca and Mg due to the representative mass number of Si. The sample is still single-crystal as determined by the diffraction pattern, but contains a high density of extended defects ($\sim 10^{10} \text{ cm}^{-2}$). This is consistent with past reports of high backscattering yields in implanted GaN annealed at these conditions.^{66,91} We ascribe these defects to the formation of dislocation loops in the incompletely repaired lattice.

By sharp contrast, annealing at 1400 °C for 10 secs brings a substantial reduction in the implant-induced defects, as shown in Fig. 3.12. The sample is again single-crystal, but the only contrast in the TEM plan view is due to the lower density ($\sim 10^9 \text{ cm}^{-2}$) of threading dislocations arising from lattice-mismatch in the heteroepitaxy. This appears to correlate well with the fact that the highest electron mobility and carrier density in these samples was observed for 1400 °C annealing. Clearly the ultra-high temperature annealing is required to completely remove lattice damage in GaN implanted with high doses. However it may not be needed for the material implanted with lower dose ($\leq 5 \times 10^{13} \text{ cm}^{-2}$) where the amount of damage created is correspondingly less.

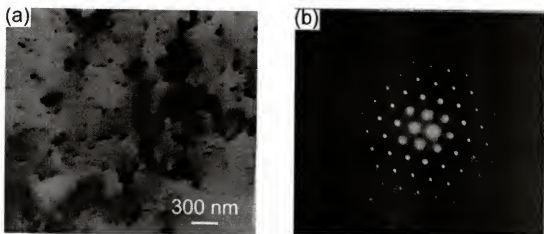


Fig. 3.11 TEM plan view (a) and selected -area diffraction pattern from Si^+ -implanted GaN after $1100\text{ }^{\circ}\text{C}$, 10 s annealing.

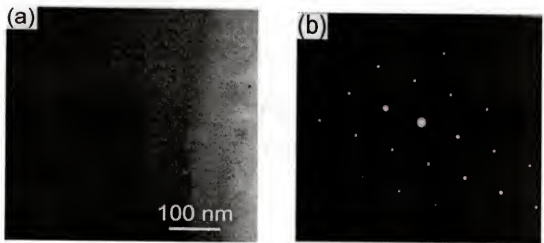


Fig. 3.12 TEM plan view (a) and selected-area diffraction pattern from Si^+ -implanted GaN after $1400\text{ }^{\circ}\text{C}$, 10 s annealing.

CHAPTER 4

HIGH RESISTANCE IMPLANT ISOLATION IN GaN

4.1 Introduction

Implant isolation has been widely used in compound semiconductor devices for inter-device isolation such as in transistor circuits or to produce current channeling such as in lasers. The implantation process can compensate the semiconductor layer either by a damage or chemical mechanism, maintaining a planar device morphology without the need for etched mesa isolation. For the former compensation, high resistivity is created due to introduction of mid-gap, damage-related levels, which trap the free carriers in the materials. This effect is stable only to the temperature at which the damage is annealed out. For the latter case, the implanted species occupy the substitutional sites and create chemically induced deep levels in the middle of the bandgap. The compensation is thermally stable in the absence of outdiffusion or precipitation of the species. There is a strong need for an understanding of the implant isolation process in GaN because of the emerging applications for high temperature, high power electronics based on this material and its alloys.

To date in the GaN materials system there has only been an examination of damage-induced isolation. Binari et al.⁵² investigated H^+ and He^+ isolation of n-GaN, with the material remaining compensated to over 850 °C with He^+ and 400 °C with H^+ . Subsequent work focused on N^+ implantation into both n- and p-type GaN, producing defect levels of 0.83 eV and 0.90 eV, respectively.³⁰ The implantation damage was

annealed out at 850 °C in n-type and 950 °C in p-type material. Very effective isolation of AlGaN heterostructure field effect transistor structures has been achieved with a combined P⁺/He⁺ implantation leading to sheet resistances of $\geq 10^{12} \Omega/\square$ and an activation energy of 0.71 eV for the resistivity.⁹² Some work has also been reported for isolation of In-containing nitrides using O⁺, F⁺ or N⁺.⁵³ Basically, the implantation in InN and InGaN ternaries produced only one or two orders of magnitude increase in sheet resistance after an optimum anneal. The relatively low sheet resistance ($\sim 10^4 \Omega/\square$) achieved is not sufficient for inter-device isolation in electronic circuits.

To create chemically-induced isolation, it is necessary to implant impurities with electronic levels in the GaN bandgap, and usually a minimum dose (dependent on the doping level of the sample) is required. In other compound semiconductors, species such as Fe, Cr, Ti and V have been employed, with other examples being O in AlGaAs (where Al-O complexes are thought to form)⁹³ and N in GaAs (C) (where C-N complexes are thought to form).⁹⁴

In this chapter multi-energy O⁺, Ti⁺, Fe⁺ or Cr⁺ were implanted into n- and p-type GaN to create high resistivity. The annealing temperature dependence of the sample sheet resistance was measured up to 900 °C. The defect levels in the materials of both types were determined by temperature-dependent TLM measurements. The thermally stable, electrically active concentration of deep states produced by these species was found to be $< 7 \times 10^{17} \text{ cm}^{-3}$ in both conductivity types of GaN, with the sample resistivity approaching its original, unimplanted value by ~900 °C in all cases. The defect levels created in the implanted material are within 0.5 eV of either bandedge.

4.2 O-implantation for Selective Area Isolation

0.3 μm thick n (Si-doped) or p (Mg-doped) type GaN layers were grown on 1 μm thick undoped GaN on (0001) sapphire substrates by rf plasma activated Molecular Beam Epitaxy. The carrier concentration in the doped layers was $7 \times 10^{17} \text{ cm}^{-3}$ in each case. Ohmic contacts were formed in a transmission line pattern (gap spacings of 2, 4, 8, 16 and 32 μm) by e-beam evaporation and lift-off of Ti/Au (n-type) and Ni/Au (p-type) annealed at 800 $^{\circ}\text{C}$ and 700 $^{\circ}\text{C}$, respectively, for 30 s under N_2 . The total metal thickness was 4000 \AA , so that these regions could act as implanted masks. A schematic of the resultant structure is shown in Fig 4.1.

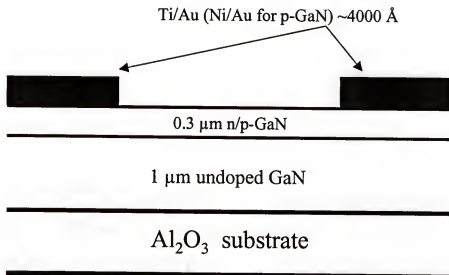


Fig. 4.1 Schematic of GaN structure for measurement of sheet resistance after ion implantation.

The samples were then implanted at 25 °C using multiple-energy O⁺ ions at different doses: 50 keV, $1 \times 10^{14} \text{ cm}^{-2}$; 100 keV, $2 \times 10^{14} \text{ cm}^{-2}$; 200 keV, $3 \times 10^{14} \text{ cm}^{-2}$. The total dose was therefore $6 \times 10^{14} \text{ cm}^{-2}$. The sheet resistance was obtained from TLM measurements for both the as-implanted sample and those annealed at increasing temperatures to 900 °C. Measurement temperatures in the range of 25 °C-200 °C were employed to determine the defect levels in the material.

In the case where the implanted species is chemically active in the GaN it is the ion profiles that are the important feature, since it is the electrically active fraction of these implanted species that determines the isolation behavior. In the case where the isolation simply results from damage-related deep levels, then it is the profile of ion damage that is important. Fig. 4.2 shows both the calculated ion profiles (top, from P-CODETM simulations) and damage profiles (bottom, from Transport-of-Ions-in-Matter (TRIM) simulations) for the multiple energy O⁺ implant scheme. Note that the defect density is generally overstated in these calculations due to recombination of vacancies and interstitials. In any case, the doses are below the amorphization threshold for GaN.

Fig. 4.3 (top) shows the evolution of the sheet resistance for O⁺ implanted n- and p-type GaN with annealing temperature. For n-type sample, the as implanted sheet resistance was $4 \times 10^9 \Omega/\square$, and gradually decreased over the entire annealing temperature range. We do not believe this is a result of O-related shallow donor states because these are not activated until annealing temperatures above 1100 °C.³⁰ By contrast, the trend in the sheet resistance in p-type GaN is typical of those observed with damage-related isolation.⁶⁴ The as-implanted resistance is 5 orders of magnitude higher than that of the unimplanted material due to creation of deep traps that remove holes from the valence

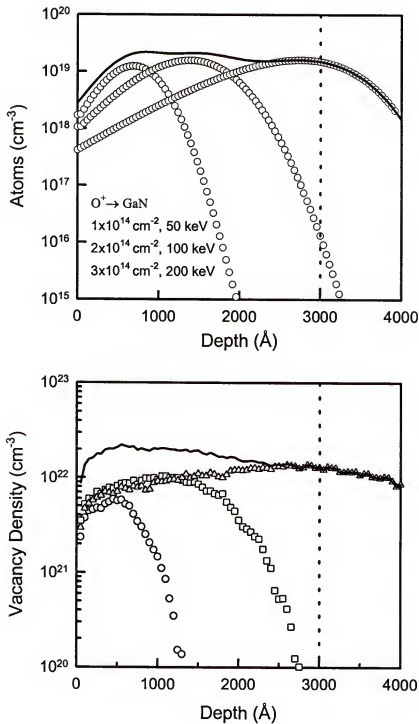


Fig. 4.2 Ion (top) and Damage (bottom) profiles for multiple energy O⁺ implant sequence into GaN.

band. Subsequent annealing tends to further increase the sheet resistance, by reducing the probability for hopping conduction as the average distance between trap sites is increased.⁹⁵ Beyond particular annealing temperature (600 °C in this case) the trap density begins to fall below the carrier concentration and holes are returned to the valence band. This produces a decrease in sheet resistance toward the original, unimplanted values. Note that even after 900 °C anneal, the sheet resistance is still two orders of magnitude above the unimplanted value. A general rule of thumb for achieving acceptable device isolation is that the implanted region should have a sheet resistance $\geq 10^7 \Omega/\square$.⁹⁶ In this implant process, sheet resistances above this value were achieved for annealing temperatures up to 600 °C for n-type and 800 °C for p-type.

Fig. 4.3 (bottom) shows Arrhenius plots of the sheet resistance of the implanted n- and p-type GaN annealed at either 300 °C (n-type) or 600 °C (p-type). The annealing temperature for the p-type sample was chosen to be close to the point where the maximum in the sheet resistance occurs. The activation energies derived from these plots represent the Fermi level positions for the material at the particular annealing temperatures employed. Note that the values are far from midgap (1.7 eV for hexagonal GaN). Particularly, the defects created in n-GaN are much shallower, and could not produce efficient compensation in this material.

From Fig. 4.2, we find that there is a region at the immediate surface (<300 Å) that receive much lower concentration of cumulative damage, simply because the projected range of the 50 keV O⁺ ions is ~400 Å. Inadequate coverage of this near surface region is a common problem in implant isolation processes because conventional implant systems typically have minimum operating voltages in the 20-30 keV range. One solution to this

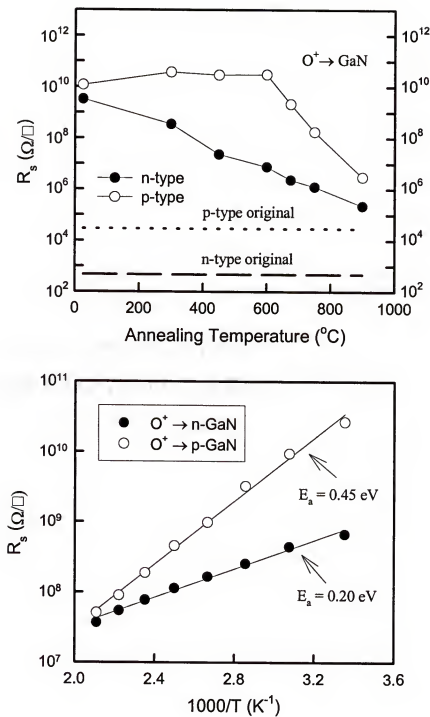


Fig. 4.3 Evolution of sheet resistance of n- and p-type GaN with annealing temperature after O^+ implantation (top), and Arrhenius plots of sheet resistance after either 300 $^{\circ}\text{C}$ (n-type) or 600 $^{\circ}\text{C}$ (p-type) annealing (bottom).

problem is to implant through a surface layer which acts to move the projected range of the lowest energy implant closer to the semiconductor surface. Titanium is a good choice, since it can be readily removed after the implant step with HF solutions. To achieve good compensation in the near surface region, ~ 500 Å Ti was deposited on top of the GaN. The implantation performed under same conditions through this Ti overlayer produced a maximum sheet resistance 50 times higher than that without the implant overlayer. The subsequent evolution of the resistance with annealing temperature was similar.

4.3 Creation of High Resistivity GaN by Ti, Fe and Cr Implantation

For a better understanding of the implant isolation mechanism in GaN, Ti^+ , Fe^+ and Cr^+ were implanted into n- and p-type samples at 100 keV (10^{14} cm^{-2}), 300 keV ($2 \times 10^{14} \text{ cm}^{-2}$) and 500 keV ($3 \times 10^{14} \text{ cm}^{-2}$). The wafer structure is the same as shown in Fig. 4.1. The doses and energies were chosen to create an average ion concentration of $\sim 10^{19} \text{ cm}^{-3}$ throughout the $0.3 \mu\text{m}$ thick doped GaN layers. Both The ion and vacancy profiles for the Fe^+ implants are shown at the top and bottom, respectively, of Fig. 4.4. It is very clear that implant with these heavier ions produced much more cumulative damage than the O^+ implantation.

Fig. 4.5 shows the annealing temperature dependence of sheet resistance for Cr^+ (top) and Fe^+ (bottom). The as-implanted resistance is 6-7 orders of magnitude higher than that of the unimplanted material. The sheet resistances peak at some particular annealing temperatures (500-600 °C). There is a significant improvement in the maximum R_s in n-type sample compared to the O^+ implantation described earlier ($\sim 10^{12}$ vs. $\sim 10^{10} \Omega/\square$), because of the higher vacancy and interstitial concentrations created. The

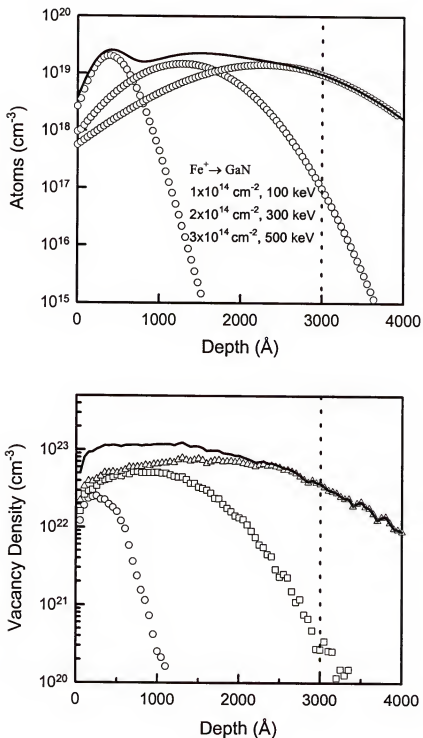


Fig. 4.4 Ion (top) and damage (bottom) profiles for multiple energy Fe^+ implant sequence into GaN.

trends in the sheet resistance show that the isolations are all typically damage-related. If Cr or Fe produced electrically active deep states related to their chemical nature in the bandgap with concentrations greater than the carrier density in the material, then the sheet resistance would remain high for annealing temperatures above 600 °C. For these two impurities it is clear that the electrically active concentration of deep states is $<7 \times 10^{17}$ cm⁻³, otherwise all the carriers would remain trapped beyond an annealing temperature of ~600 °C.

Fig. 4.6 shows the sheet resistance of Cr⁺ (top) or Fe⁺ (bottom) implanted n- and p-type GaN annealed at either 450 °C (n-type) or 600 °C (p-type), as a function of the measurement temperature. The activation energies derived from these plots are 0.49 eV and 0.45 eV in n-type and p-type GaN respectively, which give a rough estimate of the position of the Fermi levels. These implant induced defect states, although relatively shallow, efficiently compensated the wide-bandgap material.

Similar results were obtained from Ti⁺ implantation in both n- and p-GaN. Within the experimental error (± 0.04 eV), the activation energies are the same for all these implants for both conductivity types. This again suggests the defect states created are damage-related and not chemical in nature. Note that the activation energy obtained with O⁺ implant into n-GaN is much smaller. This difference may be related to the lower damage density with O⁺ implantation. The defect states in the gap are most likely due to point defect complexes of vacancies and/or interstitials, and the exact microstructure of these complexes and their resultant energy levels are expected to be very dependent on damage density and creation rate.⁹⁷ This might also explain the differences reported in the literature for the activation energies obtained with different implant species.

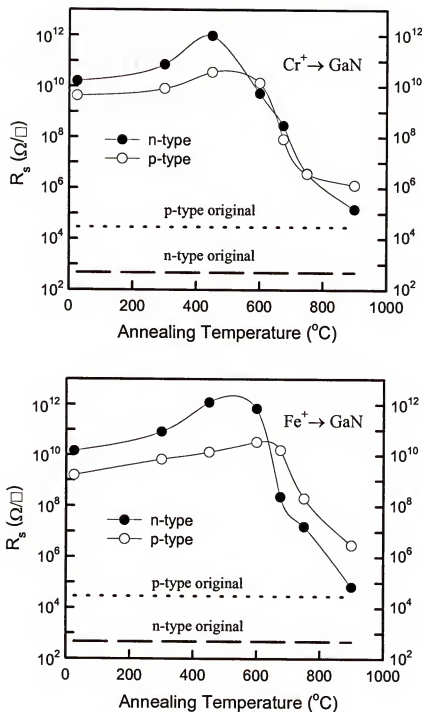


Fig. 4.5 Evolution of sheet resistance of GaN with annealing temperature after Cr⁺ (top) and Fe⁺ (bottom) implantation.

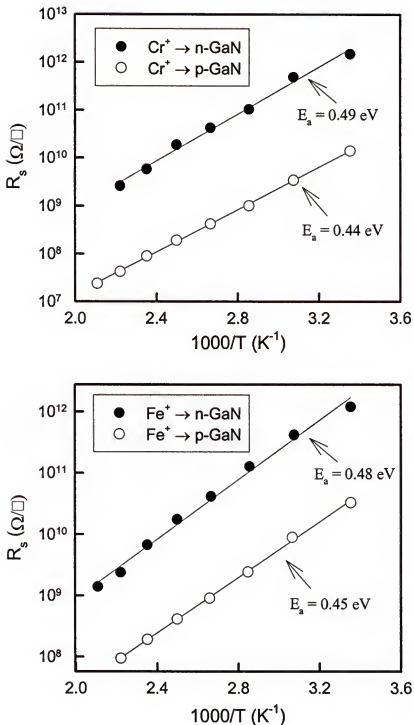


Fig. 4.6 Arrhenius plots of sheet resistance in Cr^+ (top) and Fe^+ (bottom) implanted n- and p-type GaN after annealing at either 450 $^\circ\text{C}$ (n-type) or 600 $^\circ\text{C}$ (p-type).

Fig. 4.7 shows a schematic of the energy level positions found in this work for Ti, Cr, Fe and O implanted p- and n-type GaN annealed to produce the maximum sheet resistance. Although the levels are not at midgap as is ideal for optimum compensation, they are sufficiently deep to produce high resistivity material ($\sim 10^{12} \Omega/\square$ in n-GaN and $\sim 10^{10} \Omega/\square$ in p-GaN). In GaN contaminated with transition metal impurities, non-phonon-assisted photoluminescence lines attributed to Fe^{3+} at 1.3 eV and Ti^{2+} at 1.19 eV have been reported,⁹⁸ but to date there are no electrical measurements.

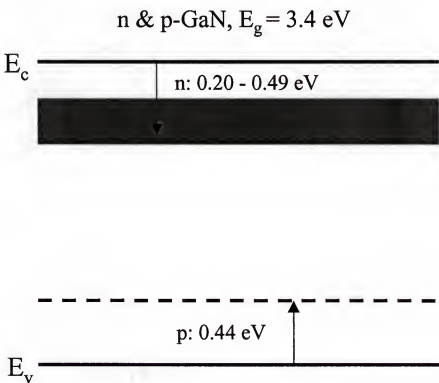


Fig. 4.7 Schematic representation of the positions in the energy band gap of defect levels created by O, Fe, Cr and Ti implant into GaN.

CHAPTER 5 ELECTRICAL CONTACTS TO GaN

5.1 Introduction

GaN is attractive for optical devices with blue or ultraviolet wavelengths as well as for high power and high temperature electronics. Critical to the success of these devices, however, are the ohmic contacts, and in some cases Schottky contacts to the semiconductors. In general, making low-resistance ohmic contact is difficult for wide bandgap materials, especially for p-type GaN due to the difficulty in doping. This creates a large voltage drop across the GaN/metal interface for ohmic contacts, which leads to poor device performance and reliability. For most devices, ohmic contacts with resistances lower than $10^{-5} \Omega \cdot \text{cm}^2$ are desired.

Ti-based contacts with contact resistances of $10^{-6} - 10^{-5} \Omega \cdot \text{cm}^2$ have been demonstrated on n-type GaN.^{23,55,99} These contacts are found to take advantages of the formation of a thin interfacial TiN layer, which is refractory, exhibit metallic conductivity, and possess low work function (<4 eV).¹⁰⁰ However, no satisfying ohmic contact to p-type GaN has been developed so far. In the search for improved contact characteristics, a wide variety of metallizations have been investigated on p-GaN besides the standard Ni/Au,^{18,56,101,102} including Ni,^{101,102} Au,^{101,103} Pd,¹⁰¹ Pd/Au,¹⁰⁴ Pt/Au,¹⁰⁵ Au/Mg/Au,¹⁰⁶ and Pd/Pt/Au.¹⁰⁵ Typically metals with large work function such as Ni, Pd or Pt are in direct contact with the GaN, and the structure is annealed at 400 - 750 °C. This produces contact resistances in the $10^{-1} - 10^{-3} \Omega \cdot \text{cm}^2$ range. Reports have also

appeared on the effect of annealing in O₂ ambient in reducing r_c,¹⁰⁷ oxidation of Ni/Au metallization and its role in improving contact quality,¹⁰⁸ the role of surface treatments in determining contact quality^{109,110} and the use of Ta/Ti contacts with low, but unstable contact resistances.¹¹¹

Another approach to achieve low-resistance contact is through semiconductor bandgap engineering. Schubert et al.¹¹² proposed the use of AlGaN/GaN superlattices as a technique to increase the average hole concentration. The periodic oscillation of the valence band edge is superimposed with the oscillation generated by piezoelectric field, would significantly reduce the Mg acceptor ionization energy and therefore increase the hole concentration. Ti/Pt/Au contacts with specific contact resistance of $\sim 4 \times 10^{-4} \Omega \cdot \text{cm}^2$ have been achieved on this structure.¹¹³ However, this scheme may not easily be applied to real devices, since the free carriers are separated into parallel sheets.

The Schottky contacts to n-GaN for a variety of elemental metals have been extensively studied. The reported Schottky barrier height increases monotonically, but does not scale proportionally with metal work function, with a considerable amount of scatter in the experimental results for a given metal (see Fig. 2.2(b)). The I-V ideality factor is usually significantly larger than 1, and the measured values of the Richardson's constant A^{**} are quite small.⁵⁴ These non-ideal behavior of GaN Schottky diodes appears to result from the presence of several transport mechanisms, and to materials and process factors such as defects present in these films, the effectiveness of surface cleans prior to metal deposition, local stoichiometry variations, and variations in surface roughness.

There is not much information on Schottky contacts on p-GaN. Measurement of the barrier height is very difficult, due to the general difficulty in growing high quality p-type

material, and the lack of low resistance ohmic contact. The experimental values from conventional I-V and C-V methods are usually inconsistent, but also appear to be affected by the work function of the metals.¹⁰¹

One of the important issues in making high quality Schottky and ohmic contacts to GaN is the surface cleanliness. The ideal metal/semiconductor interface should be oxide- and defect-free, atomically smooth, uniform, and thermally stable, with the metal epitaxial. Analysis by spectroscopic ellipsometry showed that >30 Å of overlayer consisting organic and inorganic, and native oxide is present on air-exposed GaN.¹¹⁴ *In situ* treatments, such as N ion sputtering, were reported to remove oxide layer on the GaN surface without significant modification of the N to Ga atomic ratio.^{101,115} For Practical contacts, the samples are treated with various acidic or base solutions before deposition of metal layers. It was found that HCl-based solution is more effective in removing oxides and leaves less oxygen residue, but HF is more effective in removing carbon and hydrocarbon contamination.¹¹⁶ These *ex situ* treatments can remove significant part of the surface overlayer, but cannot produce atomically clean surfaces. The residual oxide layer is expected to act as a barrier to current flow through the metal/GaN interface, therefore has a profound influence on the electrical characteristics of contacts to GaN.

The thermal stability of metal/GaN contacts is also critically important for practical device operation (especially power electronics). The thermal limits of most of the metal/GaN combinations are between 300 °C and 600 °C.⁵⁴ At higher temperatures, severe degradation in contact morphology is observed, usually resulting from the formation of new interfacial phases, such as metal gallides.

In this chapter, as a first step to explore the improved ohmic contact to p-GaN, the effects of $(\text{NH}_4)_2\text{S}$ treatment of the GaN surface on the electrical properties were studied. Reductions in Schottky barrier height (SBH) by ~ 0.2 eV were observed. This reduction in SBH was ascribed to removal of the native oxide of thickness 1-2 nm that was present after conventional cleaning, and formed an interfacial insulating layer at the metal/GaN interface. In the second part, the thermal stability of W and WSi contacts on n- and p-type GaN was examined. Specific contact resistances in the range $10^{-5} \Omega \cdot \text{cm}^2$ were obtained for W on high dose Si-implanted GaN, while true ohmic characteristics could only be achieved at elevated temperatures for contacts on p-GaN.

5.2 Effects of Interfacial Oxides on Schottky Contact

5.2.1 $(\text{NH}_4)_2\text{S}$ Treatment to Reduce Schottky Barrier Height

Three different types of samples were employed with n-type doping of either $8 \times 10^{16} \text{ cm}^{-3}$, or 10^{18} cm^{-3} , or p-type doping (hole concentration) of 10^{17} cm^{-3} . These GaN layers were 1-3 μm thick and were grown on c-plane Al_2O_3 substrates by rf plasma-assisted Molecular Beam Epitaxy. Each of the samples was treated in one of two different ways. The first involved a conventional cleaning process that involved sequential rinsing in acetone, isopropyl alcohol and deionized water prior to lithography for defining the contact areas. After lithography, the samples were rinsed 60 secs in 30% HCl (25 °C) and 30 secs in buffered HF to remove the native oxide and then immediately loaded into the e-beam evaporator. The second cleaning process was the same as the first, but the last step was a 20 min boil in $(\text{NH}_4)_2\text{S}$. This solution does not affect the photoresist mask. The $(\text{NH}_4)_2\text{S}$ solution is effective in removing native oxide and prevention of

immediate reoxidation, since a Ga-S monolayer is formed on the surface. This should be far less of a hindrance to current flow than the presence of a much thicker native oxide. The samples had Ti/Al or Ni/Au for ohmic contacts, each annealed at 750 °C for 30 secs to produce low r_c . The Pt (400 Å)/Au (1500 Å) rectifying contacts were e-beam deposited with diameters 50-200 μm. The effective barrier heights were obtained from the forward current-voltage (I-V) characteristics, according to the eq. 2.6

$$J = A'' T^2 \exp\left(-\frac{\phi_b}{kT}\right) \left[\exp\left(\frac{eV}{nkT}\right) - 1\right]$$

where A'' is 26.4 A·cm⁻²·K⁻² for n-GaN, 96.1 A·cm⁻²·K⁻² for p-GaN.

Fig. 5.1 shows forward (top) and reverse (bottom) I-V characteristics from the n⁺ GaN diodes, either with or without the (NH₄)₂S treatment prior to Schottky contact deposition. There are several key points in this data. First, the forward current increases as a result of the (NH₄)₂S treatment due to a decrease in barrier height from 0.81 eV on the control diode to 0.58 eV on the treated diode. Second, in the linear region of the forward characteristics, the scaling of current with contact diameter is much greater than a power of two. This suggests that there is a non-uniform concentration of defects, which are generation-recombination centers. Finally, the reverse leakage current is also increased by the (NH₄)₂S treatment.

Similar data is shown in Fig. 5.2 for the n-GaN diodes, at two different rectifying contact diameters. The average barrier height decreased from ~0.99 eV on the control diodes to ~0.83 eV on the (NH₄)₂S treated samples. Both the forward and reverse current increased as a result of the (NH₄)₂S step.

Fig. 5.3 shows I-V characteristics from the p-GaN diodes. These structures showed high currents due to the difficulty in forming high barriers to p-GaN. The control diodes

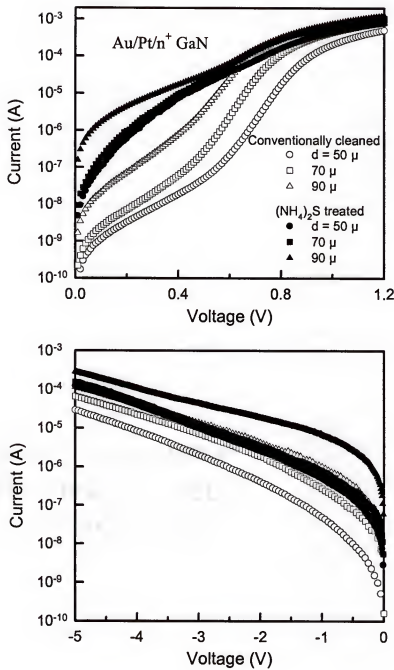


Fig. 5.1 Forward (top) and reverse (bottom) I-V characteristics from AuPt/n^+ -GaN diodes of different diameters, either cleaned in a conventional fashion prior to metal deposition or with an additional $(\text{NH}_4)_2\text{S}$ treatment.

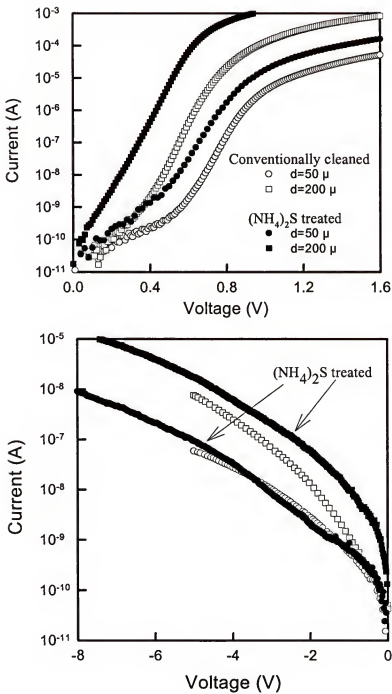


Fig. 5.2 Forward (top) and reverse (bottom) I-V characteristics from AuPt/n-GaN diodes of different diameters, either cleaned in a conventional fashion prior to metal deposition or with an additional $(\text{NH}_4)_2\text{S}$ treatment.

showed average barrier heights of 0.49 eV, which was slightly reduced to 0.47 eV as a result of the $(\text{NH}_4)_2\text{S}$ treatment. In these diodes the low bias current scaled with contact diameter, indicating that surface leakage is important. We did not passivate the perimeters of the devices in this work.

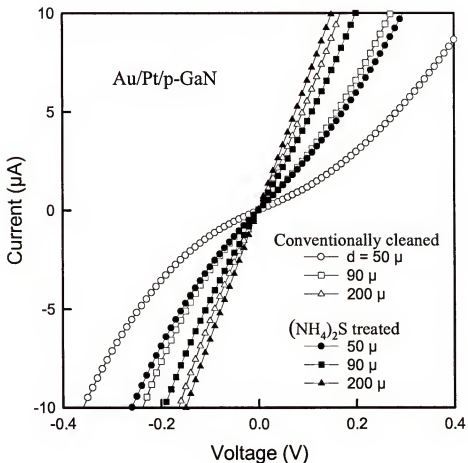


Fig. 5.3 I-V characteristics from AuPt/p-GaN diodes of different diameters, either cleaned in a conventional fashion prior to metal deposition or with an additional $(\text{NH}_4)_2\text{S}$ treatment.

Table 5.1 shows a compilation of the barrier heights and ideality factors for the n^+ , n and p diodes. The clear effect of the boiling $(\text{NH}_4)_2\text{S}$ exposure is to decrease ϕ_b , suggesting it could be promising for fabrication of high quality ohmic contacts on GaN. $(\text{NH}_4)_2\text{S}$ solution was also employed to treat completed GaN mesa Schottky diodes. Fig. 5.4 shows I-V characteristics from control and the passivated devices. Both the forward and reverse current densities increase slightly after the treatment. This probably can be ascribed to the same reason as described earlier, i.e. $(\text{NH}_4)_2\text{S}$ passivation reduced the barrier height, and the leakage current on the periphery increased. The forward section of the I-V characteristics shows only a slight improvement in ideality factor, and little change in this parameter is also showed in Table 5.1. Note that the $2kT$ leakage current in a diode of this type has contributions from both the bulk space-charge region and the mesa surface, and that sulfide passivation would only affect the latter. The fact that the

Table 5.1. Summary of electrical data for test diodes.

Sample	n		ϕ_b (eV)	
	Conventionally cleaned	$(\text{NH}_4)_2\text{S}$ treated	Conventionally cleaned	$(\text{NH}_4)_2\text{S}$ treated
AuPt/ n^+ -GaN	1.6-1.8	1.8-1.9	0.81	0.58
AuPt/ n-GaN	1.4-1.6	1.3-1.8	0.99	0.83
AuPt/ p-GaN	~2	~2	0.49	0.47

diode ideality factors did not improve suggests that the problem for the conventional III-V compound semiconductors, i.e. high density of surface states, is absent for GaN, and $(\text{NH}_4)_2\text{S}$ does not passivate the surface of GaN electronically, as it for the GaAs or InP surfaces. This is consistent with the fact that no Fermi level pinning has been observed on the GaN surface. However we generally got ideality factors much larger than unity, which indicates high dislocation densities and high compensation levels in the current state of GaN materials. Particularly for diodes fabricated on MBE grown wafers, high leakage currents were typically observed, due to relatively low epi thickness of this growth method.

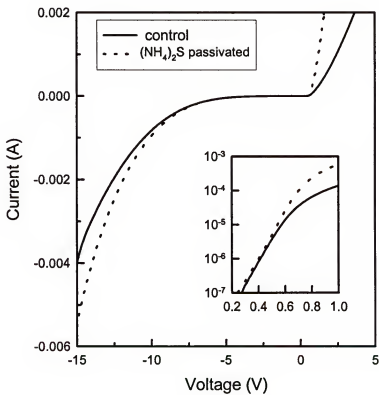


Fig. 5.4 I-V characteristics from complete GaN mesa diodes before and after $(\text{NH}_4)_2\text{S}$ treatment.

5.2.2 Interfacial Insulator Model

A contamination layer such as a thin oxide at the metal/semiconductor interface usually behaves as an insulator, and provides energy barrier for carrier injection. It is assumed that the thickness and the mean tunneling barrier height of this thin oxide layer are δ and χ , respectively. According to the Quantum Mechanics, the transmission coefficient of an electron with energy E through this barrier is given by:

$$T \approx \exp\left\{-\frac{2}{\hbar} \int_0^\delta (2m)^{1/2} [\chi - E]^{1/2} dx\right\} = \exp\left[-\frac{2}{\hbar} (2m)^{1/2} (\chi - E)^{1/2} \delta\right] \quad (5.1)$$

where m is the tunneling effective mass. Therefore, the current density across the interface can be expressed as (the zero of electron energy is chosen as the conduction band edge at the semiconductor surface) :

$$J = \frac{q m_t}{2\pi^2 \hbar^3} \exp\left[-\frac{2}{\hbar} (2m\chi)^{1/2} \delta\right] \int_0^\infty \int_0^\infty (f_s - f_m) dE_t dE_x \quad (5.2)$$

where E_x and E_t are the electron energy components normal and parallel to the Schottky barrier; f_s and f_m are the Fermi-Dirac distribution functions for electron states in the semiconductor and metal, respectively; and m_t is the effective mass component in the semiconductor transverse to the barrier. In the nondegenerate case, the current density for forward biases $V > 3kT/q$ is given by:

$$J = A'' T^2 \exp\left[-\frac{2}{\hbar} (2m\chi)^{1/2} \delta\right] \exp(-q\phi_{b0} / kT) \exp(qV / nkT) \quad (5.3)$$

Compared with eq. 2.7 The effective SBH ϕ_b can be obtained:

$$\phi_b = \phi_{b0} + \Delta\phi \quad (5.4)$$

where ϕ_{b0} is the barrier height without the interfacial layer and $\Delta\phi$ is the additional barrier due to the oxide. The parameter $\Delta\phi$ is given by $\frac{2kT}{\hbar}(2m\chi)^{1/2}\delta$. The χ value for the oxide on GaN is calculated to be ~ 0.2 eV using the free electron mass.¹⁰¹ In this work we typically observed $\Delta\phi$ to be 0.16-0.23 eV for Pt/Au on n-GaN, which yields an estimate for oxide layer thickness of 1-2 nm left on the GaN surface after conventional cleaning. Previous work on the effect of different surface treatments on the r_c of ohmic contacts on p-GaN has shown that wet chemical solutions that remove the native oxide improve the contact resistance. For example, solutions of 1 HNO₃ : 3 HCl were found to produce r_c values of $4.1 \times 10^{-4} \Omega \cdot \text{cm}^2$ for Pd/Au ohmic contacts on p-GaN, whereas untreated samples had values two orders of magnitude larger.¹⁰⁹ Similarly the use of buffered HF and boiling (NH₄)₂S, followed by a final dip in buffered HF prior to metal deposition was able to lower r_c by 3 orders of magnitude relative to untreated diodes.¹¹⁷ The oxide can also be removed by annealing the contact metal at elevated temperatures. Ishikawa et al.¹⁰¹ observed that for Ni/GaN or Ta/GaN contacts, Ni or Ta diffused into the contamination layer after annealing at 500 °C, and grew epitaxially on the GaN surface. However, Au and Pd did not react efficiently with the oxide layer. Our work suggests that the conventional *ex situ* surface treatments using HCl and HF can not completely remove the native oxide on GaN. This oxide has a strong influence on the contact characteristics on both n- and p-type GaN, and appears to be responsible for some of the wide spread in contact properties reported in the literature.

Fig. 5.5 shows the band diagrams for metal/n or n⁺ GaN structures either with an interfacial oxide (top) and after boiling in (NH₄)₂S to remove this oxide (bottom). In the case of n-GaN the dominant current conduction mechanism probably remains as

thermionic field emission (albeit with low barrier height), while for n^+ GaN there may also be a contribution from field emission. Alternative explanations for the increased current in $(\text{NH}_4)_2\text{S}$ -treated samples would be an increase in contact area due to surface roughening. However AFM measurements showed no significant change in the root-mean-square surface roughness in our samples.

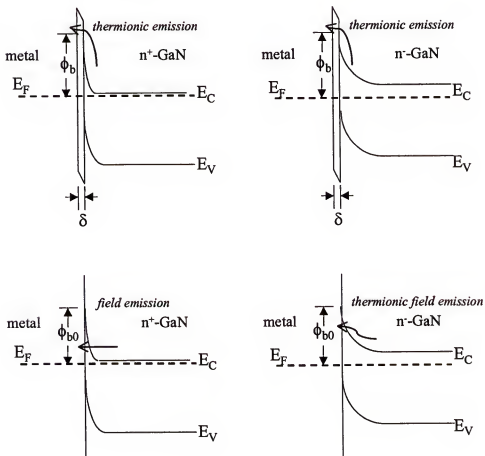


Fig. 5.5 Energy band diagrams at the interface of n^+ -GaN/metal and n^- -GaN/metal with or without an interfacial oxide layer.

5.3 Thermally Stable W-based Ohmic Contact

5.3.1 W on Si-implanted GaN

Undoped GaN layers $\sim 3 \mu\text{m}$ thick were grown on Al_2O_3 by Metal Organic Chemical Vapor Deposition. These samples were implanted with 150 keV Si^+ ions at a dose of $5 \times 10^{15} \text{ cm}^{-2}$ and annealed with AlN caps in place to 1400°C for 10 secs, as described in Chapter 2. W or $\text{WSi}_{0.45}$ layers $\sim 1000 \text{ \AA}$ thick were deposited using an MRC501 sputtering system. The sample position was biased at 90 V with respect to the Ar discharge. Prior to sputtering, the surface contamination was removed by a rinse in HCl and buffered HF solutions. Transmission line patterns were defined by dry etching the exposed metal with SF_6/Ar , and forming mesas around the contact pads using BCl_3/N_2 dry etching to confine the current flow. The samples were annealed for 60 secs at $500 - 1100^\circ\text{C}$ under flowing N_2 .

The Si implantation followed by high temperature activation yielded about a peak n-type doping concentration of $\sim 5 \times 10^{20} \text{ cm}^{-3}$. For as-deposited metal contacts on this highly doped layer, tunneling current dominates the total current. The specific contact resistance is roughly determined by the tunneling mechanism, i.e. eq.2.13. Fig. 5.6 shows the annealing temperature dependence of r_c for W contacts on Si-implanted GaN. The specific contact resistance improves with annealing up to $\sim 950^\circ\text{C}$, and degrades at high temperatures. Cole et al.¹¹⁸ observed the formation of the $\beta\text{-W}_2\text{N}$ phase at W/GaN interface at annealing temperatures between 600°C and 1000°C , as demonstrated by the x-ray results in Fig. 5.7. The as deposited sample displays a well oriented (110) W film overlaying a well oriented (002) GaN epilayer. The sample annealed at 800°C exhibits a well developed face cubic $\beta\text{-W}_2\text{N}$ phase as indicated by diffraction peaks from (111),

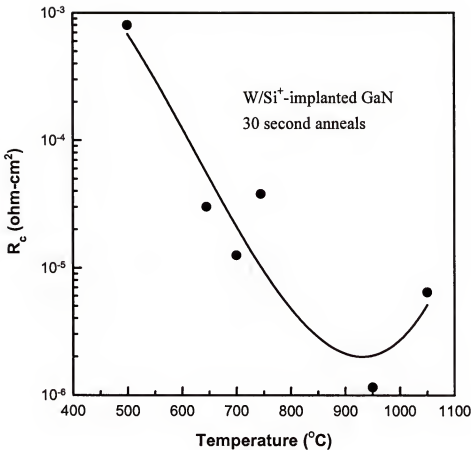


Fig. 5.6 Specific contact resistance for W on Si⁺ implanted GaN, as a function of post-metallization annealing temperature.

(200), (220) and (311) planes. The onset of the formation of this thin compound was first detected after annealing at 600 °C. Annealing at 1000 °C caused this phase to disorder, as reflected by the broaden W₂N(111) as well as the disappearance of the other W₂N peaks. The β-W₂N phase was no longer stable and subsequently transformed into the defect structure of W-N after annealing at higher temperatures.

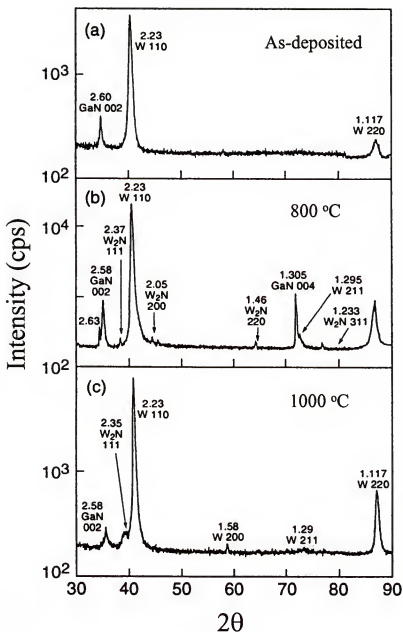


Fig. 5.7 The x-ray diffraction results for the (a) as-deposited, (b) 800 °C annealed, (c) 1000 °C annealed W on n^+ -GaN samples.

The formation of the β -W₂N phase paralleled the low specific contact resistance, and is very likely to be critical for achieving the low resistance W ohmic contacts on GaN. If the N needed to form this interfacial compound has out-diffused from the GaN without discomposing the original structure, then there would exist an accumulation of N vacancies near the GaN surface, which act as donors. Thus the surface GaN would be highly n-type and the carrier tunneling is enhanced. Another possibility is that the N out-diffusion aids in the formation of a Ga enriched highly conductive layer at the GaN surface, and results in a lower barrier height.

The near surface GaN crystal quality is of particularly importance, and could directly influence the uniformity and stability of the W contacts. TEM results showed that the defect laden regions were directly associated with contact spiking into the GaN epilayer, which in turn inhibited the formation and development of the β -W₂N interfacial phase with its associated smooth metal semiconductor interface.¹¹⁹ Protrusion of the metallization down the threading and misfit dislocations was observed at 800 °C, extending >5000 Å in some cases, which is obviously a problem for multilayer structures. In a contrast, contacting to a low defect surface improved the lateral extent of the new phase needed for ohmic contact formation and impeded contact metal spiking. The excellent structural stability of the W on GaN is shown in the SEM micrographs of Fig. 5.8, where a sharp interface is retained after 750 °C annealing.

5.3.2 Behavior of W and WSi Contacts on p-GaN

The 1 μ m thick GaN layers were grown on Al₂O₃ substrates by Molecular Beam Epitaxy using solid Ga and rf-activated N₂ from a plasma source. The Mg acceptor

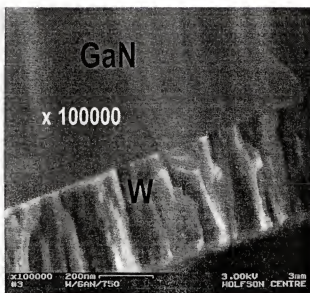
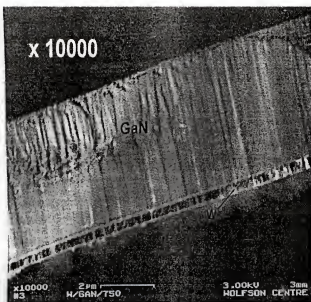


Fig. 5.8 SEM micrographs of W contact on Si^+ -implanted GaN after annealing at 750 °C.

concentration was 10^{18} cm⁻³. Cathodoluminescence revealed a strong peak at 383-385 nm, with very little deep level emission. W or WSi_{0.45} layers \sim 1000 Å thick were deposited using an MRC501 sputtering system using an Ar discharge and an acceleration voltage of 90 V. Prior to sputtering, the samples were cleaned in HCl and buffered HF solutions. TLM patterns were defined by dry etching the exposed metal with SF₆/Ar, and forming mesas around the contact pads using BC_l₃/N₂ dry etching to confine the current flow. For comparison Au(1000 Å)/Ni(500 Å) was deposited by e-beam evaporation, defined by lift-off and mesas formed by dry etching. The samples were annealed for 1 minute at temperatures from 400 - 1100 °C under a flowing N₂ ambient.

Fig. 5.9 shows I-V characteristics for WSi, W and Ni/Au metallization on p-GaN, as a function of post-deposition annealing temperature. It is clear that annealing at low temperatures improves the intimate contact between the metals and GaN, therefore, the contact quality. However, even at the optimum annealing temperatures for each metal scheme (700 °C for Ni/Au and W; 800 °C for WSi_x), there is not true ohmic behavior, and the contacts are better described as leaky Schottky diodes. At annealing temperatures above these optimum conditions, the contact characteristics worsen and become more rectifying. Note that the formation of the W₂N phase at these temperatures could result in a decrease in hole concentration at the GaN surface, and degrades the contact properties.

It is instructive to examine the contact morphology for different annealing temperatures. Fig. 5.10 shows scanning electron micrographs of Ni/Au after annealing at 400 °C (top left) and 700 °C (top right), and of W after annealing at 400 °C (bottom left) or 900 °C (bottom right). In the former case the Ni/Au becomes strongly islanded, as reported by Venugopalan et al.¹²⁰ due to dissociation of the GaN by the reaction with the

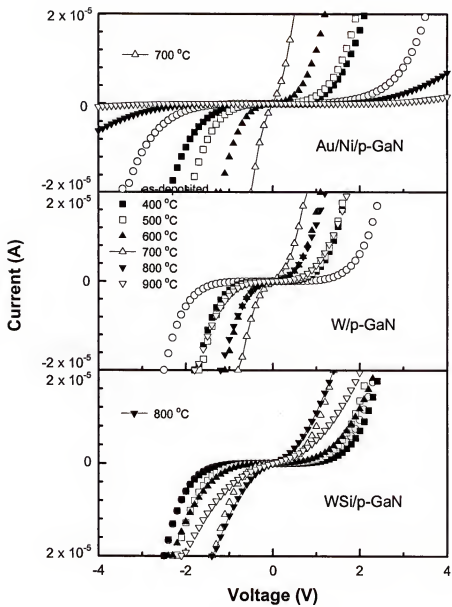


Fig. 5.9 Annealing temperature dependence of I-V characteristics of WSi, W and Ni/Au contacts on p-GaN (60 s anneal times).

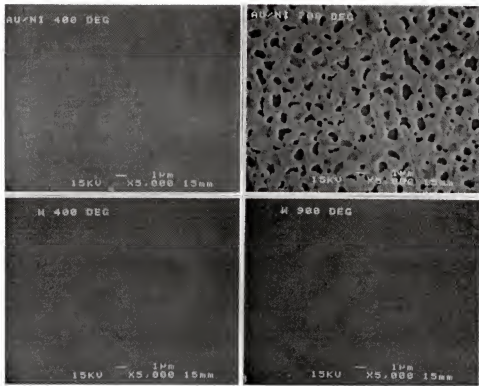


Fig. 5.10 SEM micrographs of Ni/Au contacts on p-GaN after 60 s anneals at 400 °C (top left) or 700 °C (top right), and W contacts after annealing at 400 °C (bottom left) or 900 °C (bottom right).

Ni.⁵⁶ The rate of the reaction becomes increasingly rapid above ~600 °C, and in our contacts a 5 min anneal at 700 °C produced extremely poor results both from an electrical and structural view point. The reacted nature of the Ni/Au contact will definitely be a problem in electronic devices such as heterojunction bipolar transistors or junction field effect transistors, where the contact size is much smaller than in photonic devices, and need to be uniform for large numbers of devices. By sharp contrast, both the W and WSi did not show any loss of dimensional stability or surface morphology degradation even at

> 900 °C. In addition, there is not a strong dependence of the electrical characteristics on annealing time, as shown in Fig. 5.11. There is little change in the contact properties for 30 secs - 2 mins, and contacts become slightly more rectifying for longer time, indicating the interfacial reaction is very limited. In conjunction with the low defect density material grown by epitaxial overgrowth, the use of WSi and W metallization should prove useful in improving the thermal stability of p-ohmic contacts on GaN.

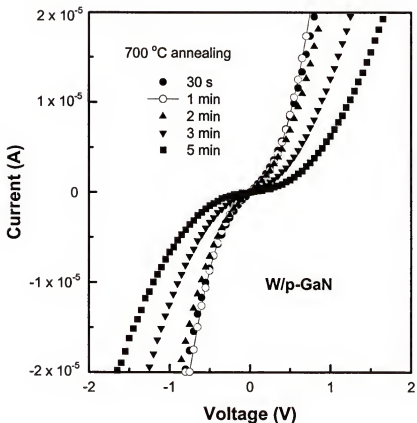


Fig. 5.11 Annealing time dependence at 700 °C of I-V characteristics from W contacts on p-GaN.

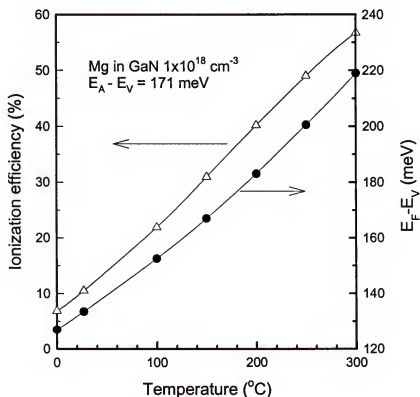
From Fermi - Dirac statistics we can calculate the Fermi level position E_F for p-GaN containing 10^{18} acceptors $\cdot \text{cm}^{-3}$ as a function of absolute temperature T , from

$$N_A \frac{1}{1 + 2 \exp((E_a - E_F) / kT)} = N_V \exp(-(E_F - E_V) / kT) \quad (5.5)$$

where N_A is the acceptor concentration, $E_a = 171$ meV for Mg in GaN and N_V is the valence band density of states. Using this relation, we calculated the ionization efficiency for Mg as a function of sample temperature, as shown in Fig. 5.12. At 25 °C, only ~10% of the Mg is ionized, whereas the efficiency increases to ~57% at 300 °C. Given the acceptor concentration in our films, this means the hole density rises from $\sim 10^{17}$ at 25 °C to $\sim 5.7 \times 10^{17} \text{ cm}^{-3}$ at 300 °C. Past investigations have shown a combination of thermionic emission and thermionic field emission as the dominant conduction mechanisms in contacts to p-GaN.^{105,121} At elevated operating temperatures, the hole density in the material increases rapidly, leading to a decrease in material sheet resistance. Concurrently there should be more efficient thermionic emission and tunneling of holes across the metal - GaN barrier, leading to a decrease in specific contact resistance. Fig. 5.13 shows I - V characteristics from the three different metallization schemes on p-GaN, as a function of measurement temperature. At 250 °C the Ni/Au is truly ohmic, whereas the W and WSi_x have linear characteristics at 300 °C. Table 5.2 shows the r_c values at 300 °C are $9.2 \times 10^{-2} \Omega \cdot \text{cm}^2$ (Ni/Au), $6.8 \times 10^{-1} \Omega \cdot \text{cm}^2$ (W) and $2.6 \times 10^{-2} \Omega \cdot \text{cm}^2$ (WSi). The substrate sheet resistance decreases with increasing temperature, indicating that the increased hole concentration plays a major role in decreasing r_c . Whilst device operation at elevated temperatures clearly would improve the p-contact resistance, it remains to be seen how much of a trade-off this entails in terms of degraded reliability.

Table 5.2. Temperature-dependent contact data for p-GaN.

Contact	Measurement temperature (°C)	Specific contact resistance ($\Omega\text{-cm}^2$)	Contact resistivity ($\Omega\text{-mm}$)	Sheet resistance (Ω/\square)
Ni/Au	200	0.125	415.7	13900
Ni/Au	250	0.121	319.5	8470
Ni/Au	300	0.092	205.9	4600
W	300	0.682	758.4	-
WSi	300	0.026	1728.3	-

Fig. 5.12 Ionization efficiency of Mg acceptors in GaN, and Fermi-level position for GaN doped with 10^{18} cm^{-3} Mg acceptors as a function of temperature.

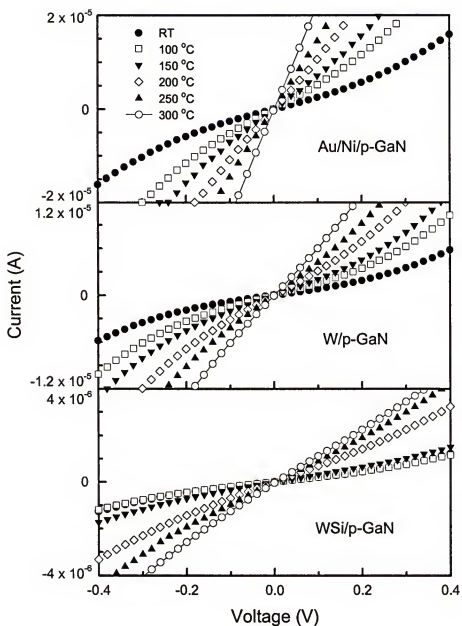


Fig. 5.13 Measurement temperature dependence of I-V characteristics of Ni/Au, W and WSi contacts on p-GaN.

CHAPTER 6

DRY ETCH DAMAGE IN GaN

6.1 Introduction

Dry etching has proven an effective technique for the formation of mesas in GaN devices. However, exposure to the energetic ions may result in significant damage, which often degrades the material properties and device performance. ICP technique uses lower ion energies than RIE, and thus in general has lower damage levels as a result. At high source powers, however, ion flux incidence on the surface is so high that substantial damage can be detected to depths of a few hundred angstrom. Plasma induced damage to GaN may take several forms, all of which lead to changes in its electrical and optical properties, as follows:

1. Ion induced creation of lattice defects which generally behave as deep level states and thus produce compensation, trapping or recombination in the material. Due to channeling of the low energy ions that strike the sample, and rapid diffusion of the defects created, the effects can be measured as deep as 1000 Å from the surface, even though the projected range of the ions is only ≤ 10 Å.
2. Unintentional passivation of dopants by atomic hydrogen. The hydrogen may be a specific component of the plasma chemistry, or may be unintentionally present from residual water vapor in the chamber or from sources such as photoresist mask erosion. The effect of the hydrogen deactivation of the dopants is a strong function of substrate temperature, but may occur to depths of several thousand angstroms.

3. Creation of non-stoichiometric surfaces through preferential loss of one of the lattice elements. This can occur because of strong differences in the volatility of the respective etch products, leading to enrichment of the less volatile species, or by preferential sputtering of the lighter lattice element if there is a strong physical component to the etch mechanism. Typical depths of this non-stoichiometry are <100 Å.
4. Deposition of polymeric film from plasma chemistries involving CH_x radicals, or from reaction of photoresist masks with Cl_2 -based plasma.

In GaN-based photonic devices, the constraints placed on dry etching are minimal. Usually these structures are heavily doped, and etch depths are comparatively large, and thus are fairly resistant to damage. Moreover, the etch proceeds to a n^+ GaN layer, onto which an ohmic contact is subsequently deposited. Preferential loss of N_2 from the near-surface region during the etch step is actually beneficial in this case because it leads to increased n-type doping levels and hence lower contact resistances.^{99,122,123} By sharp contrast, in electronic devices such as HBTs or BJTs, the etching requirements are much more demanding. Low damage processes are required to form mesas for the base and collector contacts without increasing recombination in the base-emitter junction or surface leakage in the base-collector junction.

To date, much less is known about the electrical effects of dry etch damage, and its subsequent removal by chemical treatment or annealing in the GaN system than in other compound semiconductors. Most past work in this area has focussed on n-type material. The sheet resistances of GaN, InGaN, InAlN and InN samples were found to increase in proportion to ion flux and ion energy in an ECR Ar plasma.^{124,125} Ren et al.¹²⁶ examined

the effect of ECR BCl_3/N_2 and CH_4/H_2 plasmas on the electrical performance of InAlN and GaN channel field effect transistors. They found that hydrogen passivation of the Si doping in the channel may occur if H_2 is a part of the plasma chemistry and that preferential loss of N_2 degraded the rectifying properties of Schottky contacts deposited on plasma-exposed surfaces. Saotome et al.¹²⁷ found pure Cl_2 plasma treatment decreased near band-edge PL intensity of the GaN samples by a factor of approximately five through introduction of non-radiative levels, whereas subsequent photo-assisted wet etching restored this to about half of the original value.

There is very little information available on the electrical effects of plasma damage in p-type GaN. Shul et.al.¹²⁸ reported that the sheet resistance of p-GaN increased upon exposure to pure ICP Ar discharge. The increases were almost linearly dependent on ion energy, but weakly dependent on ion flux.

In this chapter, we studied systematically the effects of ICP N_2 , H_2 , Ar or Cl_2/Ar discharge exposure under various conditions on the properties of n- and p-GaN Schottky diodes. The choice of these plasma chemistries enabled us to differentiate between ion mass effects and the role of physical versus chemical components of the etching. The depth and thermal stability of the damage has been determined. Wet etching and thermal annealing were employed to restore the electrical properties of the damaged materials.

6.2 Plasma Damage in n-GaN

6.2.1 Comparison of N_2 and H_2 Discharge Exposure

The layer structure and contact metals are shown schematically in Fig. 6.1. The GaN was grown by rf plasma-assisted Molecular Beam Epitaxy on c-plane Al_2O_3

substrates. The Ti/Au Ohmic contacts were pattern by lift-off and annealed at 750 °C, producing contact resistances in the $10^{-4} \Omega \cdot \text{cm}^2$ range. Samples were exposed to either pure N₂ or H₂ discharges in a Plasma Therm 790 ICP system at a fixed pressure of 5 mTorr. The gases were injected into the ICP source at a flow rate of 15 standard cubic centimeters per minute (sccm). The experimentally varied parameters were source power (300-1000 W) and rf chuck power (40-250 W), which control ion flux and ion energy, respectively. The Pt/Au Schottky metallization was then deposited through a stencil mask by e-beam evaporation. I-V characteristics were recorded on a HP4145A parameter analyzer, and the reverse breakdown voltage (V_B) was defined as the voltage at which the leakage current was 5×10^{-3} A. We found in all cases that plasma exposure caused significant increases in forward and reverse currents, with ideality factors increasing from typical values of 1.4-1.7 on control samples to >2. For this reason we were unable to extract meaningful values of either ideality factor or barrier height.

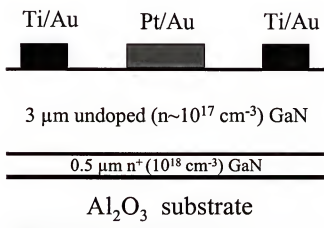


Fig. 6.1 Schematic of GaN Schottky diode structure.

Fig. 6.2 shows a series of I-V characteristics from the GaN diodes fabricated on samples exposed to either H₂ or N₂ discharges at different source powers. It is clear that N₂ plasma exposure creates more degradation of the diode characteristics than does H₂ exposure. This implicates the ion mass (²⁸N₂⁺, ²H₂⁺ for the main positive ion species) as being more important in influencing the electrical properties of the GaN surface than a chemical effect, since H₂ would be likely to preferentially remove nitrogen from the GaN as NH₃.

The variations of V_B of the diodes with the source power during plasma exposure are shown in Fig. 6.3. For any exposure to the N₂ discharges, V_B is severely reduced. By contrast there is less degradation with the H₂ plasma exposures at higher source powers. This is likely related to the lower average ion energy at those conditions, as shown at the bottom of Fig. 6.3. The average ion energy is approximately equal to the sum of dc self-bias and plasma potential, with the latter being in the range -22 to -28 V as determined by Langmuir probe measurements. Ion induced lattice damage in GaN may display n-type conductivity, due to more N atom displaced. In addition, the heavy N₂⁺ ions are also more effective in preferential sputtering of the N relative to Ga and creating N vacancy, compared to the H₂⁺ ions. The net result is that N₂⁺ ions will lead to more degradation of the surface electrical properties of GaN than do H₂⁺ ions of similar energy.

Similar conclusions can be drawn from the data on the effect of increasing rf chuck power. Fig. 6.4 shows the diode I-V characteristics from H₂ or N₂ plasma exposed samples at fixed source power (500 W) but varying rf chuck power. There are once again very severe decreases in breakdown voltage and increases in leakage current. The dependence of V_B on rf chuck power during the plasma exposures is shown in Fig. 6.5,

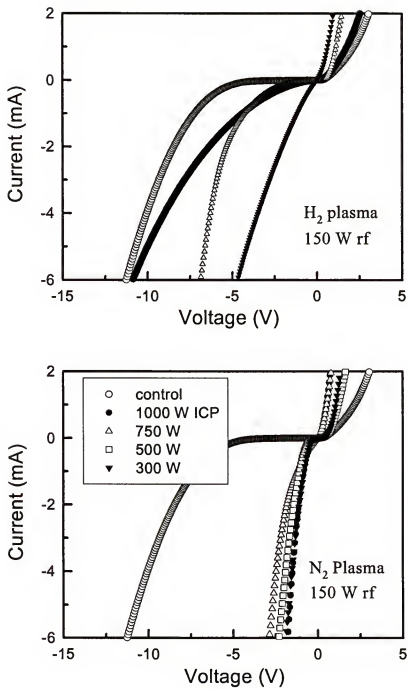


Fig. 6.2 I-V characteristics from GaN diodes before and after H₂ (top) and N₂ (bottom) plasma exposure (150 W rf chuck power, 5 mTorr) at different ICP powers.

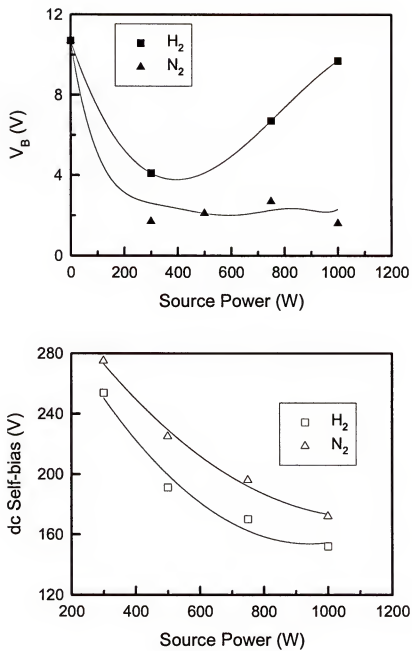


Fig. 6.3 Variation of V_B in GaN diodes (top) and dc chuck self-bias (bottom) as a function of ICP source power in H_2 or N_2 plasmas (150 W rf chuck power, 5 mTorr).

along with the dc self bias. The V_B values fall by more than a factor of two even for very low self-biases, and emphasize how sensitive the GaN surface is to degradation by energetic ion bombardment. The degradation saturates beyond \sim 100 W chuck power, corresponding to ion energies of \sim 175 eV. We assume that once the immediate surface becomes sufficiently damaged, the contact properties basically cannot be made any worse and the issue is then whether the damage depth increases with the different plasma parameters. Since ion energy appears to be a critical factor in creating the near-surface damage, damage depth would be expected to increase with ion energy in a non-etching process. In the case of simultaneous etching and damage creation (e.g. in Cl_2/Ar etch processing), higher etch rates would lead to smaller depth of residual damage because the disordered region would be partially removed.

For completed n-GaN diodes exposed to ICP discharges, we observed the changes in the electrical properties were much less severe than those above. However, the low bias forward currents of the damaged devices were still increased by up to two orders of magnitude. Auger Electron Spectroscopy showed that plasma exposure created a N_2 -deficient region around the periphery of the rectifying contact, which reduced the barrier to current conduction. By contrast, the reverse I-V is more strongly dependent on the bulk doping in the GaN under the contact and is less affected by the plasma damage.

6.2.2 Effect of Etching Chemistries on Damage

It would be expected that exposure to etching chemistries such as Cl_2/Ar create less and shallower damage, on the basis of the fast etching rate and hence improved damage removal. In this section we compare the effects of Cl_2/Ar and Ar ICP exposure on the

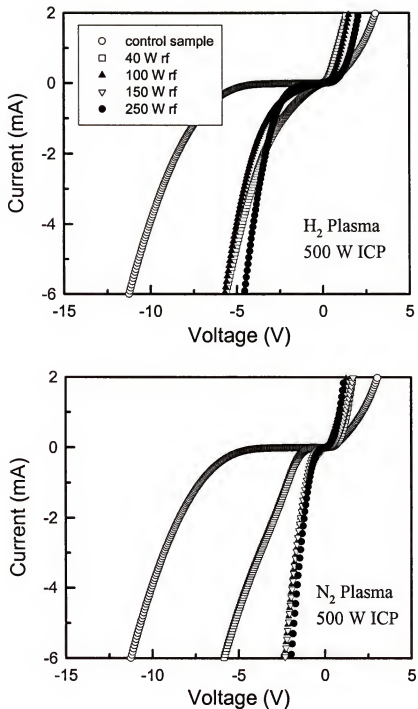


Fig. 6.4 I-V characteristics from GaN diodes before and after H₂ (top) or N₂ (bottom) plasma exposure (500 W source power, 5 mTorr) at different rf chuck powers.

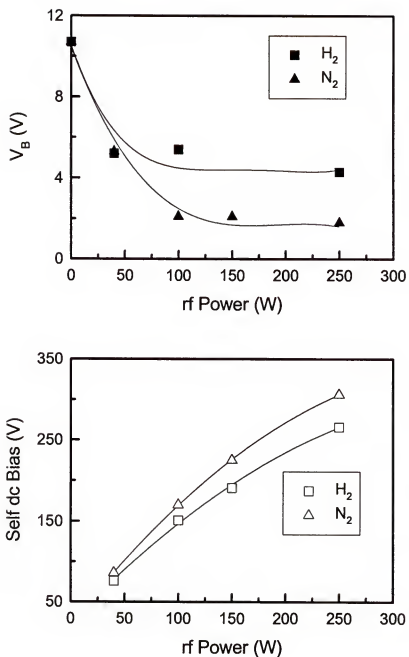


Fig. 6.5 Variation of V_B in GaN diodes (top) and dc chuck self-bias (bottom) as a function of rf chuck power in H_2 or N_2 plasmas (500 W source power, 5 mTorr).

electrical properties of n-GaN Schottky diodes. The layer structure consisted of $0.5 \mu\text{m n}^+$ (10^{18} cm^{-3}) GaN grown on c-plane Al_2O_3 substrate by MBE, followed by $1 \mu\text{m}$ of nominally doped ($n \sim 5 \times 10^{16} \text{ cm}^{-3}$) GaN. The mesas were etched with Ar/Cl_2 ICP discharges at low powers, and ohmic contacts were formed by e-beam evaporation and lift-off of $\text{Ti}/\text{Al}/\text{Pt}/\text{Au}$, followed by annealing at 800°C to remove dry etch damage and alloy the contacts. The samples were exposed to either $10\text{Cl}_2/5\text{Ar}$ or 15Ar (where the numbers denote the gas flow rate in standard cubic centimeters per minute) ICP discharges in a Plasma-Therm ICP reactor at a fixed pressure of 3 mTorr . We investigated a range of rf chuck powers (25-250 W) and etch times (4-100 secs), with a fixed source power of 500 W. The Schottky metallization Pt/Au ($\phi = 50, 70$ or $90 \mu\text{m}$) was then deposited on the damaged surface by e-beam evaporation, followed by lift off. Schematic of the mesa diodes and a SEM micrograph are shown in Fig. 6.6.

Fig. 6.7 shows a series of I-V characteristics from n-type GaN diodes fabricated on samples exposed to either Cl_2/Ar (top) or Ar (bottom) discharges at different rf chuck powers. There is a significant reduction in V_B under all conditions, with Ar producing less damage at low chuck powers. This is probably related to two factors – the slightly higher chuck bias with Cl_2/Ar due to the lower positive ion density in the plasma (Cl is more electronegative than Ar) and the heavier mass of the Cl_2^+ ions compared to Ar^+ . This is consistent with data on the relative effects of N_2 and H_2 plasma exposure, i.e. ion mass was more important in influencing the electrical properties of the GaN surface than any chemical effects.

The variations of V_B and V_F with the rf chuck power during plasma exposure are shown in Fig. 6.8 (top). At powers $\leq 100 \text{ W}$ (this correspond to ion energies $\sim 150 \text{ eV}$),

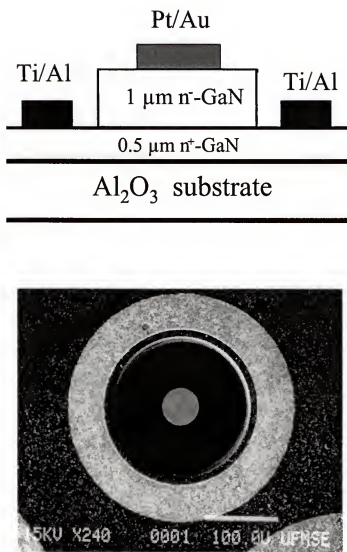


Fig. 6.6 Schematic of the diode structure (top) and SEM of a complete device (bottom).

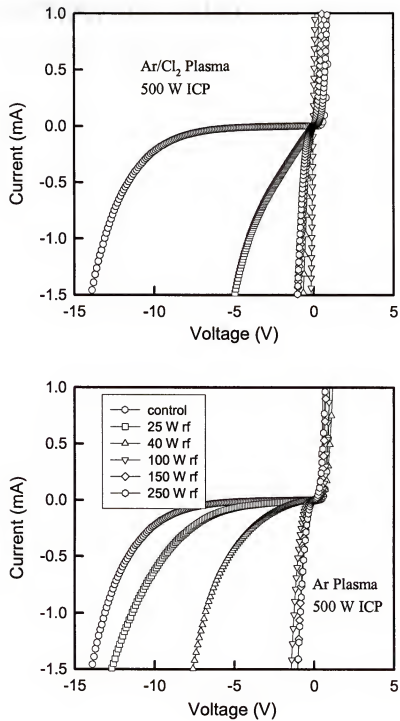


Fig. 6.7 I-V characteristics from n-GaN samples exposed to ICP Cl_2/Ar (top) or Ar (bottom) discharges (500 W source power) as a function of rf chuck power prior to deposition of the rectifying contact.

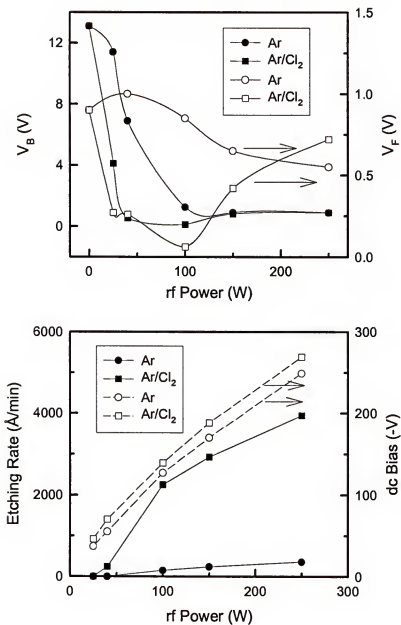


Fig. 6.8 Variations of V_B and V_F (top), and n-GaN etching rate or dc self-bias (bottom) as a function of rf chuck power for n-GaN diodes exposed to ICP Ar and Cl_2/Ar discharges (500 W source power).

the Cl_2/Ar creates more degradation of V_B , as discussed above, while at higher powers the damage saturates. This is also reflected in the variation of the forward on-voltage V_F with rf chuck power. Note that the etch rate in Cl_2/Ar discharges increases rapidly with the rf chuck power (shown at the bottom of the figure). The amount of the etch damage is the direct result of competition between defect introduction and etching processes.

Fig. 6.9 shows a series of I-V characteristics from n-type GaN diodes fabricated on samples exposed to the two different plasmas for different times at fixed rf chuck power (150 W) and source power (500 W). It is clear that the damage accumulates rapidly, with the I-V characteristics becoming linear at longer times. The breakdown voltages < 1 V for basically all plasma exposure times for both Cl_2/Ar and Ar. Fig. 6.10 shows the variations in V_B and V_F in these diodes with plasma exposure, together with the etch depth versus etch time (bottom). As is readily apparent, V_B decreases dramatically after even short plasma exposures (4 secs) and then tends to recover slightly up to ~ 25 secs. It should be remembered that this is damage accumulating ahead of the etch front. The V_B values are saturated after some points due to the etching or sputtering effect. Since the etch rate with Cl_2/Ar is much faster (Fig. 6.10 bottom), the damage accumulation in this chemistry should reach the saturation point much earlier, as shown in Fig 6.10 (top).

The rapid accumulation could explain why Cl_2/Ar discharges produce more damage than pure Ar. Significant damage could be created in the near-surface region in this high density plasma after even a very short exposure. The Schottky contact is most sensitive to the electrical properties of the immediate surface layer. For these reasons it is possible that Cl_2/Ar discharges, containing ions with higher energy and heavier mass, produce

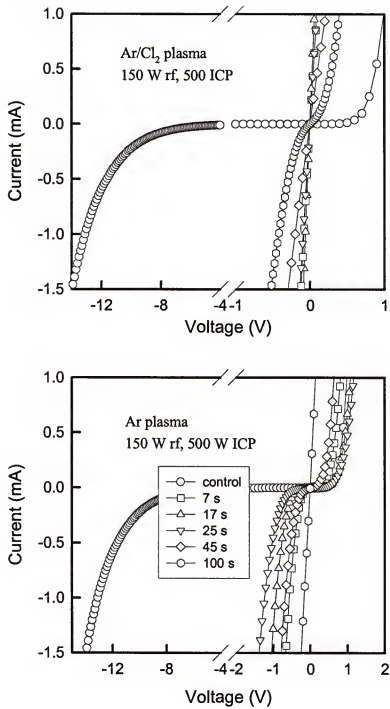


Fig. 6.9 I-V characteristics from n-GaN samples exposed to ICP Cl₂/Ar (top) or Ar (bottom) discharges (150 W rf chuck power, 500 W source power) as a function of plasma exposure time prior to deposition of the rectifying contact.

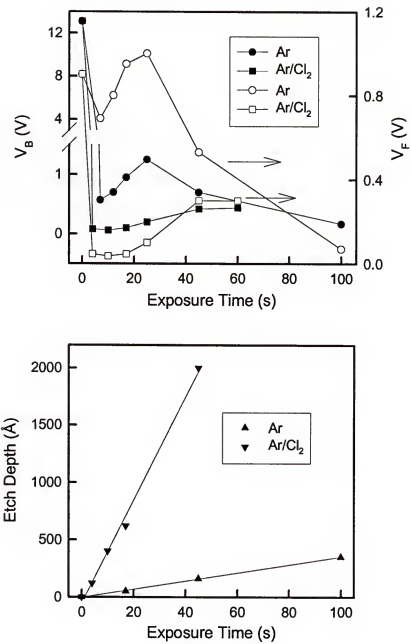


Fig. 6.10 Variation of V_B and V_F (top) and of n-GaN etch depth (bottom) as a function of plasma exposure time for n-GaN diodes exposed to ICP Cl_2/Ar discharges (500 W source power 150 W rf chuck power).

more degradation in the electrical properties of the GaN Schottky diodes than pure Ar discharges, even though the damage depth may be smaller due to high etch rate. Note that we have studied a worst-case scenario for damage introduction during ICP etching. In a real etch process of GaN device, damage would be less severe because much low power conditions are employed.

6.2.3 Thermal Stability of Damage

To examine the thermal stability of the etch damage, the n-type GaN samples were exposed to the 500 W source power, 150 W rf chuck power (dc self-bias -221 V), 5 mTorr N₂ discharge, and then annealed in N₂ for 30 secs at 300 – 850 °C prior to deposition of the rectifying contact. Fig. 6.11 (top) compares the AFM data from the control sample, the as-exposed sample and samples annealed at 550 °C or 750 °C. The fact that plasma exposure severely degraded the surface is clear, as the RMS surface roughness increases from 0.8 nm to 4.2 nm. Subsequent annealing essentially restored the initial morphology. I-V data from annealed samples are shown in Fig. 6.11 (bottom). These samples show that increasing annealing temperature up to 750 °C brings a substantial improvement in V_B. However for annealing at 850 °C the diode began to degrade and this is consistent with the temperature at which N₂ begins to be lost from the surface.⁷³

It is instructive to compare the thermal stability of Pt/Au contacts on the damaged and undamaged GaN. The metal was deposited on control sample and the sample which was plasma exposed (N₂, 500 W source power, 150 W rf chuck power, 5 mTorr), then annealed at different temperatures for 30 secs. The I-V characteristics is shown in Fig.

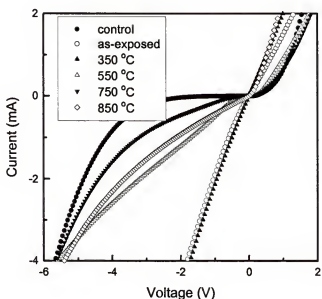
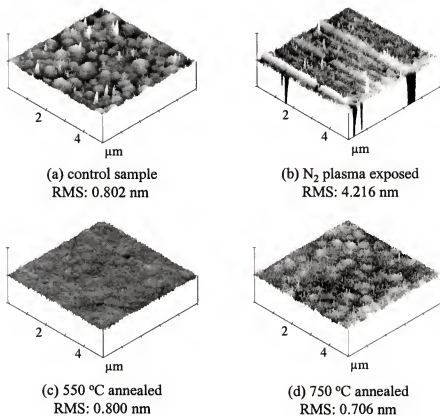


Fig. 6.11 AFM scans of GaN surfaces (top) and I-V characteristics from GaN diodes (bottom) before and after N_2 plasma exposure (500 W source power, 150 W rf power, 5 mTorr) and subsequent annealing at different temperatures prior to deposition of the Schottky contacts.

6.12. The Pt/Au contact is stable to 700 °C on unetched samples, while in the case where the samples were exposed to the N₂ plasma, the I-V characteristics shows continued worsening upon annealing. The poorer stability in etched samples could be related to the surface damage enhancing interfacial reaction between the Pt and GaN, while ohmic contact on the damaged materials can take advantage of this enhanced alloying process.

Fig. 6.13 shows I-V characteristics from control, samples which were exposed to Ar or Cl₂/Ar discharges at a fixed source power (500 W) and rf chuck power (150 W rf), and annealed in N₂. Again, the annealing produced a significant recovery of the electrical properties, and more restoration was achieved for samples exposed to the Ar plasma. The V_B values are shown in Fig. 6.14, as a function of post-plasma exposure annealing temperature. Annealing temperatures between 700-800 °C restored >70% of the original V_B value, but clearly annealing alone cannot remove all of the dry etch induced damage. Annealing temperatures above 800 °C were found to lead to preferential loss of N₂ from the surface, with a concurrent degradation in V_B.

6.3 Plasma Damage in p-GaN

6.3.1 Surface Type-Conversion Effects

The layer structure consisted of 1 μm of undoped GaN (n~5×10¹⁶ cm⁻³) grown on a c-plane Al₂O₃ substrate, followed by 0.3 μm of Mg doped (p~5×10¹⁷ cm⁻³) GaN. The samples were grown by rf plasma-assisted Molecular Beam Epitaxy. Ohmic contacts were formed with Ni/Au deposited by e-beam evaporation, followed by lift-off and annealing at 750 °C. The GaN surface was then exposed for 1 min to ICP H₂ or Ar plasmas in a Plasma-Therm 790 System. The 2 MHz ICP source power was varied from

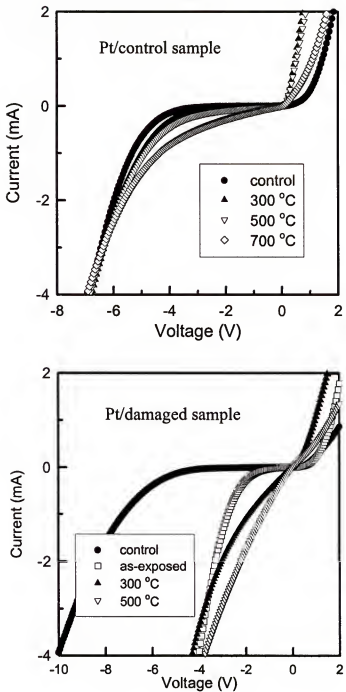


Fig. 6.12 I-V characteristics from GaN diodes with Schottky metal deposited on control samples (top) and plasma-exposed samples (bottom) followed by annealing at different temperatures.

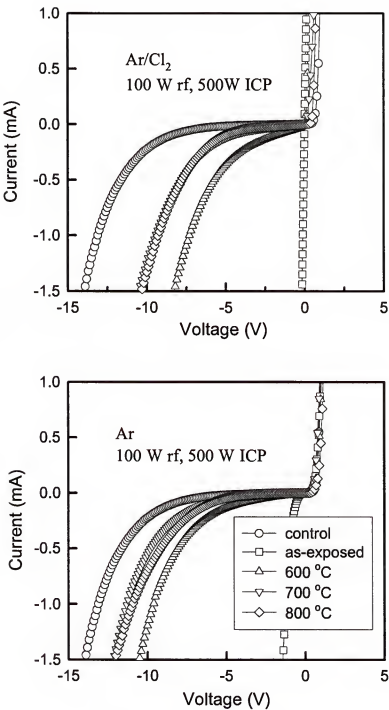


Fig. 6.13 I-V characteristics from n-GaN samples exposed to ICP Cl₂/Ar (top) or Ar (bottom) discharges (500 W source power, 100 W rf chuck power) as a function of annealing temperature prior to deposition of the rectifying contact.

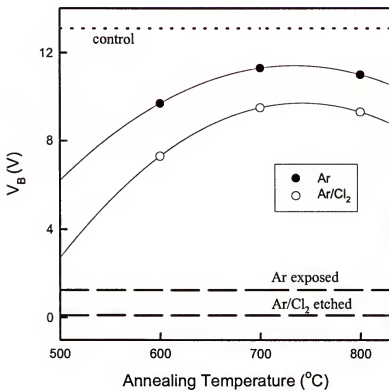


Fig. 6.14 Variation of V_B in n-GaN diodes exposed to ICP Cl_2/Ar or Ar discharges (500 W source power, 100 W rf chuck power) with annealing temperature prior to deposition of the rectifying contact.

300-1400 W, while the 13.56 MHz rf chuck power was varied from 20-250 W. The former parameter controls ion flux incident on the sample, while the latter controls the average ion energy. Ti/Pt/Au contacts with 250 μm diameter were deposited through a stencil mask. The I-V characteristics of the diodes were recorded on an HP 4145A parameter analyzer. The unetched control diodes have reverse breakdown voltages of ~2.5-4 V depending on the wafer – these values were uniform ($\pm 12\%$) across a particular wafer.

Fig. 6.15 shows the I-V characteristics from samples exposed to either H₂ (top) or Ar (bottom) ICP discharges (150 W rf chuck, 2 mTorr) as a function of source power. In both cases there is an increase in both the reverse breakdown voltage and the forward turn-on voltage, with these parameters increasing monotonically with the source power during plasma exposure.

Fig. 6.16 shows this increase in breakdown voltage as a function of source power, and also the variation of the chuck dc self-bias. As the source power increases, the ion density also increases and the higher plasma conductivity suppresses the developed dc bias. Note that the breakdown voltage of the diodes continues to increase even as this bias (and hence ion energy, which is the sum of this bias and the plasma potential) decreases. These results show that ion flux plays an important role in the change of diode electrical properties. The other key result is that Ar leads to consistently more of an increase in breakdown voltage, indicating that ion mass is important rather than any chemical effect related to removal of N₂ or NH₃ in the H₂ discharges.

The increase in breakdown voltage on the p-GaN is due to a decrease in hole concentration in the near-surface region through the creation of shallow donor states. The key question is whether there is actually conversion to an n-type surface under any of the plasma conditions. Fig. 6.17 (top) shows the forward turn-on characteristics of the p-GaN diodes exposed to different source power Ar discharge at low source power (300 W), the turn-on remains close to that of the unexposed control sample, i.e. the surface remains p-type with no significant reduction in conductivity. However there is a clear increase in the turn-on voltage at higher source powers, and in fact at ≥ 750 W the

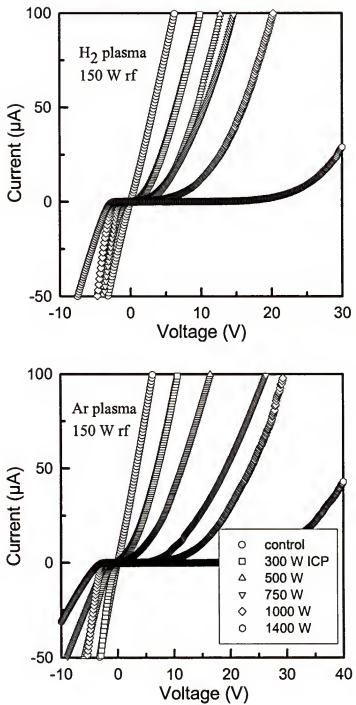


Fig. 6.15 I-V characteristics from samples exposed to either H_2 (top) or Ar (bottom) ICP discharges (150 W rf chuck power) as a function of ICP source power prior to deposition of the Ti/Pt/Au contact.

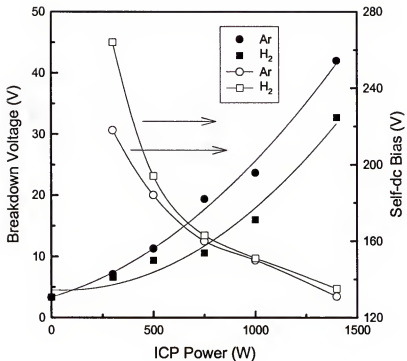


Fig. 6.16 Variation of diode breakdown voltage in samples exposed to H₂ or Ar ICP discharges (150 W rf chuck power) at different ICP source powers prior to deposition of the Ti/Pt/Au contact. The dc chuck self-bias during plasma exposure is also shown.

characteristics are those of an n-p junction, i.e. the surface has converted to n-type. The turn-on voltage at the highest flux conditions is ~ 3.3 V (Fig. 6.17 (bottom)), which is close to the build-in potential of a GaN n-p diode. Since the hole concentration in the GaN is $\sim 10^{17}$ cm⁻³, the Mg acceptor concentration is $\sim 10^{19}$ cm⁻³ based on the ionization level of ~ 170 meV. This means the plasma exposure at high flux conditions produces $>10^{19}$ cm⁻³ shallow donor states and there is surface conversion. According to our previous study, the obvious conclusion is nitrogen vacancies create these shallow donor

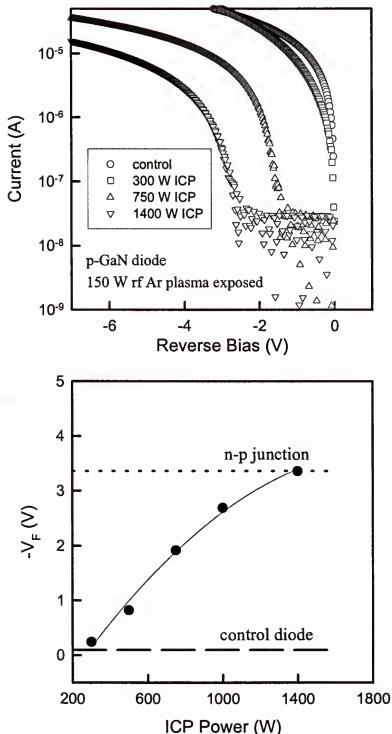


Fig. 6.17 Forward turn-on characteristics (top) and turn-on voltage (bottom) of diodes exposed to ICP Ar discharges (150 W rf chuck power) at different ICP source powers prior to deposition of the Ti/Pt/Au contact.

levels. We found N_2 loss from the p-GaN surface during thermal annealing at temperatures >900 °C also produced significantly decreased p-type conduction.

The influence of rf chuck power on the diode I-V characteristics is shown in Fig. 6.18 for both H_2 and Ar discharges at fixed source power (500 W). A similar trend is observed as for the source power experiments, namely the reverse breakdown voltage increases, consistent with a reduction in p-doping level near the GaN surface. Surface type conversion also occurred at high powers.

Fig. 6.19 plots breakdown voltage and dc chuck self-bias as a function of the applied rf chuck power. The breakdown voltage initially increases rapidly with ion energy (the self-bias plus ~ 25 V plasma potential) and saturates above ~ 100 W probably due to the fact that sputtering yield increases and some of the damaged region is removed. Note that there are very large changes in breakdown voltage even for low ion energies, emphasizing the need to carefully control both flux and energy.

6.3.2 Thermal Stability of Damage

One important method of removing plasma-induced damage is annealing. In these experiments we exposed the samples to the same type of plasma (Ar, 750 W source power, 150 W rf chuck power) and then annealed under N_2 at different temperatures. Fig. 6.20 (top) shows the I-V characteristics of these different samples, while Figure 6.20 (bottom) shows the resulting breakdown voltages as a function of annealing temperature. On this wafer, plasma exposure caused an increase in breakdown voltage from ~ 2.5 to ~ 18 V. Subsequent annealing at 400 °C initially decreased the breakdown voltage, but higher temperature produced a large increase. In some cases, the samples were found to

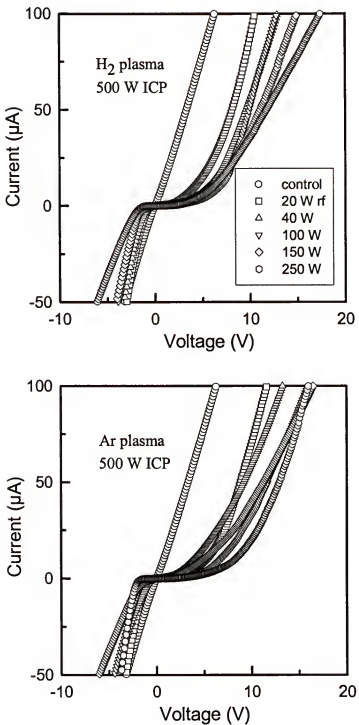


Fig. 6.18 I-V characteristics from samples exposed to either H₂ (top) or Ar (bottom) ICP discharges (500 W source power) as a function of rf chuck power prior to deposition of the Ti/Pt/Au contact.

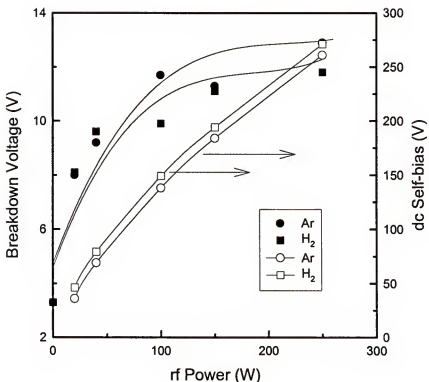


Fig. 6.19 Variation of diode breakdown voltage in samples exposed to H₂ or Ar ICP discharges (500 W source power) at different rf chuck powers prior to deposition of the Ti/Pt/Au contact. The dc chuck self-bias during plasma exposure is also shown.

be highly compensated after annealing at 600 °C-700 °C. At temperatures above 700 °C, the diodes characteristics returned toward their initial values and were back to the control values by 900 °C. This behavior is similar to that observed in implant-isolated compound semiconductors where ion damage compensates the initial doping in the material, producing higher sheet resistances, as discussed in Chapter 4. In many instances the damage site density is larger than that needed to trap all of the free carriers, and trapped electrons or holes may move by hopping conduction. Annealing at higher temperatures

removes some of the damage sites, but there are still enough to trap all the conduction electrons/holes. Under these conditions the hopping conduction is reduced and the sample sheet resistance actually increases. At still higher annealing temperatures, the trap density falls below the conduction electron or hole concentration and the latter are returned to their respective bands. Under these conditions the sample sheet resistance returns to its pre-implanted value. The difference in the plasma exposed samples is that the incident ion energy is a few hundred eV compared to a few hundred keV in implant-isolated material. In the former case the main electrically active defects produced are nitrogen vacancies near the surface, whereas in the latter case there will be vacancy and interstitial complexes produced in far greater numbers to far greater depths. We did not examine the time dependence of the damage removal, but expect it would show a square root power of annealing time.

In our previous work on plasma damage in n-GaN we found that annealing at ~ 750 $^{\circ}\text{C}$ almost returned the electrical properties to their initial values. If the same defects are present in both n- and p-type materials after plasma exposure, this difference in annealing temperature may be a result of a Fermi level dependence to the annealing mechanism.

6.4 Determination of Damage Profile in GaN

An important question is the depth of the plasma-induced damage. We found we were able to etch p-GaN very slowly in boiling NaOH solutions, at rates that depended on the solution molarity (Fig. 6.21) even without any plasma exposure of the material. This enabled us to directly measure the damage depth in plasma exposed samples in two different ways.

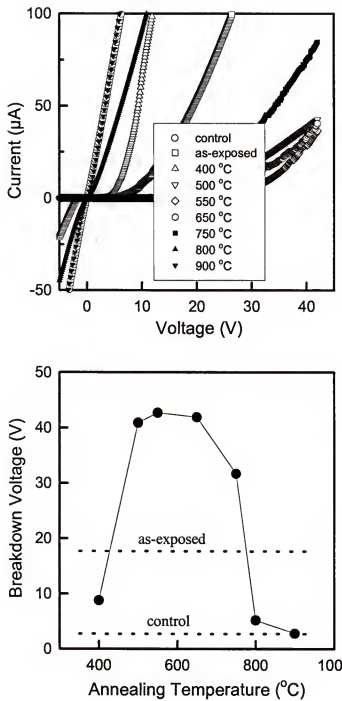


Fig. 6.20 I-V characteristics from samples exposed to ICP Ar discharges (750 W source power, 150 W rf chuck power) and subsequently annealed at different temperatures prior to deposition of the Ti/Pt/Au contact (top) and breakdown voltage as a function of annealing temperature (bottom).

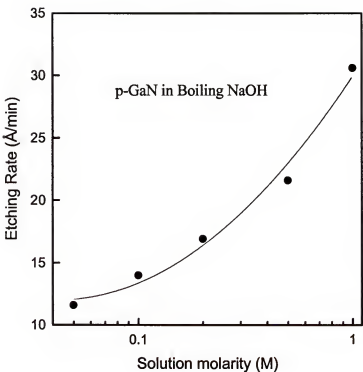


Fig. 6.21 Wet etching rate of p-GaN in boiling NaOH solutions as a function of solution molarity.

The first method involved measuring the etch rate as a function of depth from the surface. Defective GaN resulting from plasma, thermal or implant damage can be wet chemically etched at rates much faster than undamaged material because the acid or base solutions are able to attack the broken or strained bonds present. Kim et al.¹²⁹ reported that the wet etch depth on thermally or ion-damaged GaN was self-limiting. Fig. 6.22 shows the GaN etch rate as a function of depth in samples exposed to a 750 W source power, 150 W rf chuck power Ar discharges (-158 V dc bias). The etch rate is a strong function of the depth from the surface and saturates between ~425-550 Å. Within this depth range the etch rate is returned to the “bulk” value characteristic of undamaged p-GaN.

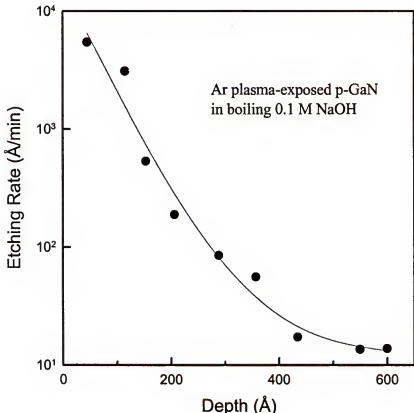


Fig. 6.22 Wet etching rate of Ar plasma-exposed (750 W source power, 150 W rf chuck power) p-GaN as a function of depth into the sample.

The second method to establish damage depth of course is simply to measure the I-V characteristics after removing different amounts of material by wet etching prior to deposition of the rectifying contact. Figure 6.23 (top) shows the I-V characteristics from samples exposed to 750 W source power, 150 W rf chuck power (-160 V dc chuck bias) Ar discharges and subsequently wet etched to different depths using 0.1 M NaOH solutions before deposition of the Ti/Pt/Au contact. Fig. 6.23 (bottom) shows the effect of the amount of material removed on the diode breakdown voltage. Within the

experimental error of $\pm 12\%$, the initial breakdown voltage is re-established in the range 400-450 Å. This is consistent with the depth obtained from the etch rate experiments described above, and corresponds to the ion energy of ~ 180 eV.

It would be instructive to determine and compare the damage depth created after exposure to Cl₂/Ar and Ar discharges (500 W source power, 150 W rf chuck power, 1 min, -192 V or -171 V dc chuck bias). For these plasma conditions, we did not observe type conversion of the surface. The values of forward turn-on voltage increased after plasma exposure, due to the lowered net hole concentration. The electrical properties are almost restored after depths of 500-600 Å were removed by NaOH etching, as can be seen in Fig. 6.24. This data can also be obtained from Fig. 6.25, where the wet etch depth in plasma damaged p-GaN is plot as a function of etching time. What is clear from this data is the damage depth produced in Cl₂/Ar discharges is only slightly smaller than that in Ar discharges, even though the etch rate of GaN in the former plasma is almost 30 times higher.

The damage depth in n-type GaN can be established by photoelectrochemically (PEC)¹³⁰ wet etching different amounts of the plasma-exposed material, and then measuring the electrical properties of the GaN surfaces. For samples exposed to a 500 W source power, 150 W rf chuck power N₂ discharge, the reverse breakdown voltage was restored to about half of its initial value after removal of ~ 260 Å damaged layer. However, increasingly rough surfaces of PEC etching for larger removal depths were usually observed. The estimated damage depth for the N₂ plasma conditions mentioned above could be similar with that established in p-type GaN samples exposed to similar plasma conditions.

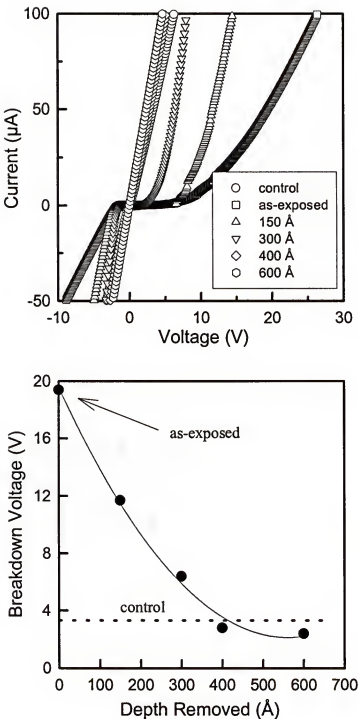


Fig. 6.23 I-V characteristics from samples exposed to ICP Ar discharges (750 W source power, 150 W rf chuck power) and subsequently wet etched to different depths prior to deposition of the Ti/Pt/Au contact (top) and breakdown voltage as a function of depth removed (bottom).

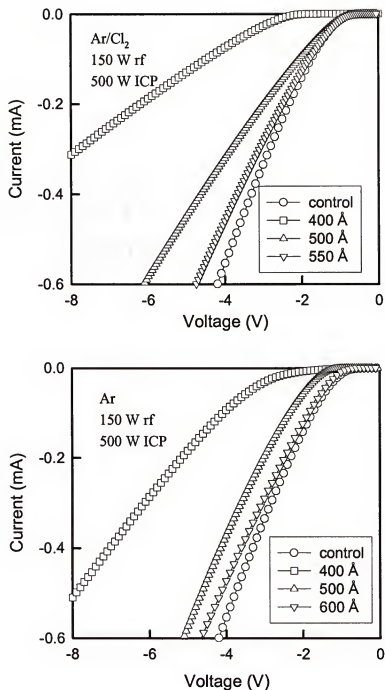


Fig. 6.24 Forward I-V characteristics from p-GaN samples exposed to ICP Cl_2/Ar (top) or Ar (bottom) discharges (500 W source power, 150 W rf chuck power) and wet etched in boiling NaOH to different depths prior to deposition of the rectifying contact.

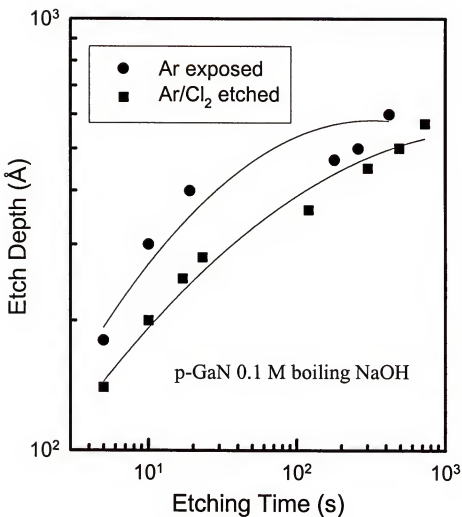


Fig. 6.25 Wet etch depth versus etch time in boiling NaOH solutions for plasma damaged p-GaN.

CHAPTER 7

FABRICATION AND SIMULATION OF GaN-BASED BIPOLAR TRANSISTORS

7.1 Introduction

Wide band gap materials such as III-V nitrides and SiC enjoy the associated advantages of low intrinsic carrier concentration and high breakdown field, and have proven to be effective for electronics for high temperature (>400 °C) and high power (>100 W) applications.⁴ The recent progress in field effect AlGaN/GaN transistors has been impressive, and has demonstrated record figures of high power microwave performance.³⁸⁻⁴¹ Compared to unipolar transistors, HBTs have higher current-carrying capacity, more uniform threshold voltages and better linearity, which are particularly important for radar and communications applications. The driving forces behind the current AlGaN/GaN HBT research come from the inherent promises of this type of device as well as the recent success of AlGaN/GaN heterostructure in both optoelectronics and microelectronics.^{36,39} However, timely development has been hampered by difficulties with growth of high quality junctions and p-type doping. High base doping concentration is required to achieve low output conductance. In state-of-the-art p-type GaN, the acceptor Mg concentration is usually two orders of magnitude higher than the hole concentration due to the high ionization level, while incorporation of high density of dopants can significantly reduce minority carrier lifetime and mobility in the base region. The few reports on GaN/AlGaN HBTs fabricated to date have shown

performance limited by high base recombination rate and high base resistance, with current gain of ~ 3 at room temperature.^{49,50} Moreover the epitaxial growth processes for these devices are far from perfected and the material quality is compromised because of the high defect densities in currently-employed heteroepitaxial crystals. Especially in the MBE grown device structures, junction leakage remains one of the key issues to be solved.

Compared to FETs, the vertical device structures with buried p-type GaN layer, such as npn HBTs and thyristors, put much more demand on fabrication techniques. The challenging issues include how to remove plasma damage and make low resistance ohmic contact after dry etching down to the p-type base region. Damage on the sidewall may result in large leakage current, and must be annealed. N₂ loss from the surface and impurity interdiffusion at the interfaces during the thermal processes may degrade the device performance. In addition, good quality ohmic contacts are difficult to be achieved even on n-type regions, because the annealing temperature cannot go high after metal is deposited on the multilayer structures.

All the work on processing discussed in earlier chapters is directed towards the optimization of GaN-based device performance. In this chapter, MBE grown GaN BJTs and AlGaN/GaN HBTs have been demonstrated with the technical improvements such as low damage dry etch, damage removal, and better ohmic contacts. The devices worked at high temperatures and high powers in common-base mode. The issues related to growth and fabrication which remain unsolved were addressed. Finally, quasi-3D simulation of the bipolar transistors (both npn and pnp structures) was performed by using a physically-

based simulator ATLAS/BLAZE. The effect of layer structure design and materials parameters on the dc performance of the devices were calculated.

7.2 Common Base Operation of GaN BJT and HBT

The layer structures of the devices, as shown in Fig. 7.1, were grown by Molecular Beam Epitaxy using rf plasma activated N₂ and solid Ga and Al. Since we have previously found that the breakdown and leakage characteristics of GaN devices are

HBT Design

GaN 5000 Å $1 \times 10^{19} \text{ cm}^{-3}$ n
AlGaN to GaN, 200 Å $1 \times 10^{19} \text{ cm}^{-3}$ n
AlGaN 20% 800 Å, $1 \times 10^{19} \text{ cm}^{-3}$ n
AlGaN 5% 200 Å, UID
AlGaN x=0 to 5%, 2000 Å, p ⁺
GaN 4000 Å $5 \times 10^{16} \text{ cm}^{-3}$ n
GaN 5000 Å $8 \times 10^{16} \text{ cm}^{-3}$ n

BJT Design

GaN 5000 Å $1 \times 10^{19} \text{ cm}^{-3}$ n
GaN 200 Å UID
GaN 2000 Å p ⁺
GaN 4000 Å $5 \times 10^{16} \text{ cm}^{-3}$ n
GaN 5000 Å $8 \times 10^{16} \text{ cm}^{-3}$ n

Fig. 7.1 Layer structure for HBT and BJT.



Fig. 7.2 TEM cross-section of BJT structure grown on GaN buffer on sapphire.

improved when the active layers are placed as far as possible from the heterointerface, the structures were grown on 2 μm thick GaN buffers on sapphire. Fig. 7.2 shows a cross-sectional transmission electron micrograph of the complete structure. The threading dislocation density in the active regions of the device is $\sim 10^9 \text{ cm}^{-2}$.

The non-self-aligned processing flow for device fabrication is shown schematically in Fig. 7.3. Inter-device isolation was achieved by dry etching mesas down to the sapphire substrate. The base and sub-collector layers were exposed for contacting by dry etching in a Plasma-Therm 790 reactor at ICP source powers of 300 W and rf chuck powers of 40 W using a 10Cl₂/5Ar discharge. Both wet etching in KOH solution and annealing at $\sim 800^\circ\text{C}$ were employed to remove dry etch damage on the base contact

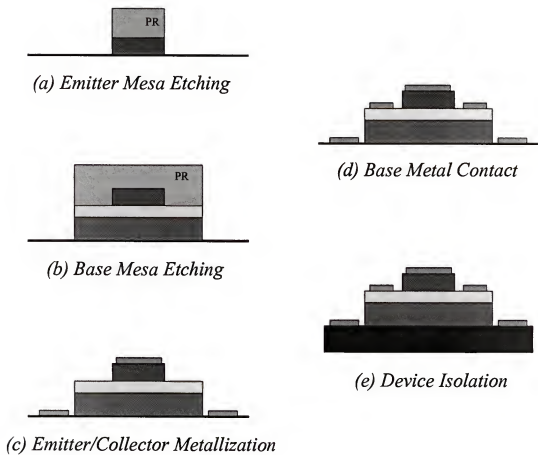


Fig. 7.3 Schematic of process sequence for GaN/AlGaN HBT.

region and the mesa sidewall. N-type ohmic metallization of Ti/Al/Pt/Au and p-type metallization of Ni/Au were deposited by e-beam evaporation and patterned by lift-off. The contacts were annealed at 500 °C for 30 secs under a N₂ ambient to reduce the contact resistance. Fig. 7.4 shows a SEM of a completed HBT (top), together with devices with emitter diameters of 50-90 μ m (bottom). The devices were tested at temperatures up to 300 °C using a temperature-controlled probe station and an HP 4145A parameter analyzer.

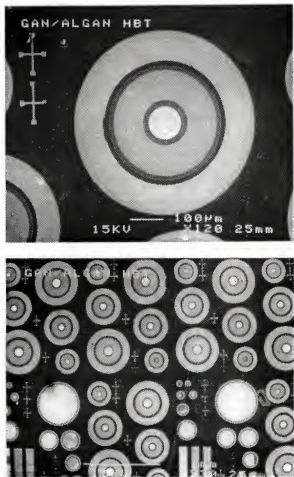


Fig. 7.4 SEM micrograph of complete HBTs.

Common-base current-voltage characteristics from a 90 μm diameter HBT are shown in Fig. 7.5. The collector-base breakdown voltage V_{BCB} is ~ 10 V at 25 $^{\circ}\text{C}$ (top), with an onset of I_{C} of 2-3 V, which is close to the built-in potential of the junction. The saturated collector current is nearly equal to the emitter current, indicating a high emitter injection efficiency. At 250 $^{\circ}\text{C}$ the common-base breakdown voltage (V_{BCB}) decreased to ~ 4 V, as shown at the bottom of Fig. 7.5. The negative temperature coefficient for V_{BCB} may be due to defect-assisted tunneling currents, either from bulk or surface states. Large junction leakage is currently a problem, especially for MBE growth. At both 25 $^{\circ}\text{C}$ and 250 $^{\circ}\text{C}$ the junction ideality factors for both emitter-base and collector-base junctions were close to 2, indicative of significant recombination. Another area for future research will be methods for surface passivation of these device structures.

Gummel plots showed dc current gains of 15-20 at room temperatures (Fig. 7.6), which is a significant improvement over past results. The oscillations at low bias in I_{C} are due to incomplete shielding of the test set-up. By removing the base contact, we observed much smaller collector current, which confirms the transistor modulation. In most of the devices we could not obtain common-emitter operation due to leakage in the collector-base junction, and high base series resistance. P-type doping must be improved to lower the resistance in the extrinsic and intrinsic base regions. Better base contact is also required. At this point, this can be achieved by using thick contact region (extrinsic base regrowth).

Since the main applications for GaN/AlGaN HBTs relate to their current-carrying capability, it is of interest to measure the current density. Fig. 7.7 shows common-base characteristics from a 50 μm diameter emitter device at 25 $^{\circ}\text{C}$. The current density was

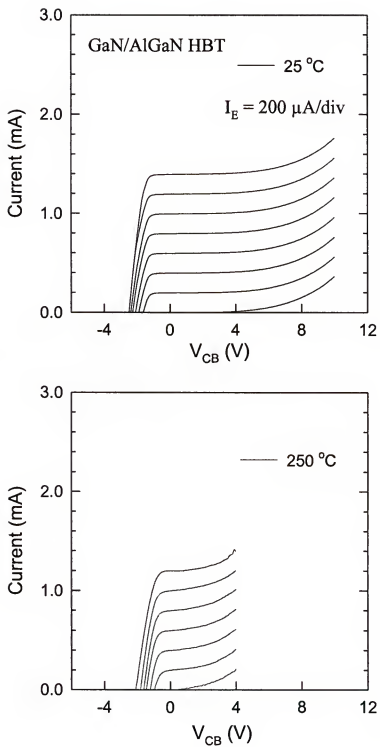


Fig. 7.5 Common-base characteristics from 50 μm diameter devices at 25 °C (top) and 250 °C (bottom). The emitter current was stepped in 200 μA increments from 200 μA .

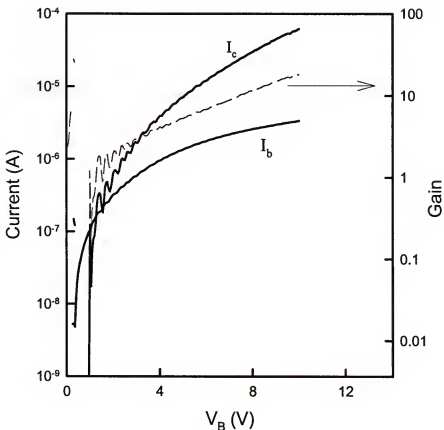


Fig. 7.6 Gummel plot of GaN/AlGaN HBT at 25 °C.

2.55 kA·cm⁻² at 8 V, corresponding to a power density of 20.4 kW·cm⁻². We note that our devices are not optimized for power operation at this point. With optimized device and use of a power mask-set, much higher powers could be expected. This is the first report of power densities in GaN/AlGaN HBTs, showing the potential of these devices for microwave power amplifiers. At high temperatures, the breakdown voltage decreased, and hence the maximum power density obtained was lower.

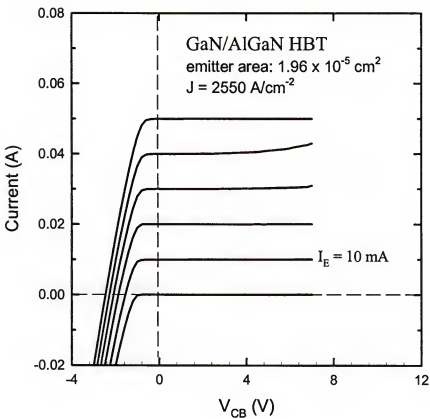


Fig.7.7 Common-base characteristics of GaN/AlGaN HBT at 25 °C.

Common-base I-V characteristics for the GaN BJTs are shown in Fig. 7.8 for both 25 °C and 300 °C measurement temperatures. The saturated collector current is nearly equal to the emitter current. At 300 °C, the devices turn-on at lower collector-base voltages but the breakdown voltage is lower. We obtained a maximum current density of 3.6 kA·cm⁻² for 50 μm diameter devices at 15 V, corresponding to a power density of 54 kW·cm⁻². The offset voltage is relatively high and is probably related to the high base contact resistance. The maximum common-emitter dc current gain $\left(\frac{dI_c}{dI_b}\right)$ was ~15 at

both temperatures, as obtained from Gummel plots. Improved junction properties and possibly surface passivation methods are likely to lead to better device performance. The forward I-V characteristics of the junctions showed evidence of significant recombination. Again, the reduced breakdown voltage at 300 °C may be due to defect-related leakage. For our designs, the BJTs appeared to be more powerful and thermally stable than the HBTs. This can probably be related to the better structure quality. The AlGaN/GaN HBT is relatively more complicated to grow, and the incorporation of Al could result in high density of defects at the hetero-interface.

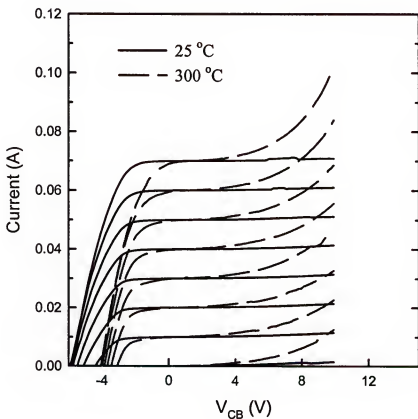


Fig. 7.8 Common-base characteristics of 50 μm diameter BJT at 25 °C and 300 °C. Emitter current was stepped from 10 to 70 mA in 10 mA steps.

A noticeable effect is that the offset voltage is relatively high in the BJTs and increases with the measurement current levels as illustrated in detail in Fig. 7.9, which shows common-base characteristics as a function of the magnitude of the emitter current steps (10 μ A-10 mA). The increases in offset voltage at higher current levels may be a result of the high base contact resistance, as well as the fact that higher voltages are needed to reach a particular current level.

7.3 Growth and Processing Issues

Several key issues, related to interface quality, impurity and doping control, minority carrier lifetime and base doping and contact, remain to be resolved for III-V nitride HBTs to achieve good common-emitter operation and AC performance. First among these is how to suppress the junction leakage in the MBE grown structure. It has been firmly established that the quality of the epi layers is a function of growth thickness and the type of buffer layer on which they are grown. Fig. 7.10 shows I-V characteristics from the emitter-collector junction for devices grown by MBE directly on sapphire, or on buffers grown by MOCVD or HVPE. While the latter are much thicker ($>10 \mu\text{m}$), the morphology can be much rougher than MOCVD buffers. It is quite evident the junction quality is significantly improved on the MOCVD buffers. The dislocation density in the active regions is reduced by at least one order of magnitude, as revealed by TEM measurements.

The second concern is achieving good dopant and background impurity control in HBT structures. The p-type dopant should be rapidly switched on and off around the base region, and not spill-over into the adjacent n-type AlGaN emitter, where it could cause

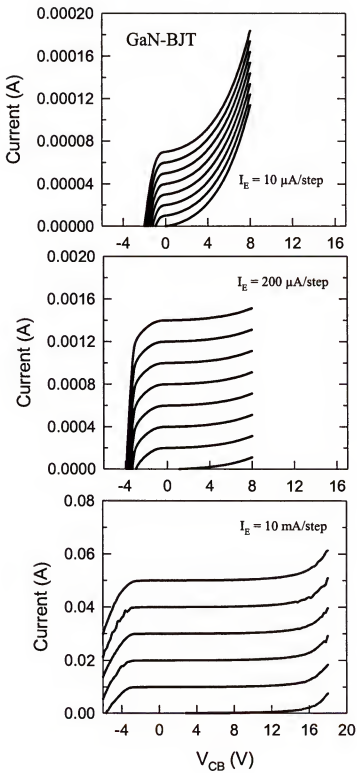


Fig. 7.9 Common-base characteristics of BJTs at 25 °C as a function of different emitter current increments.

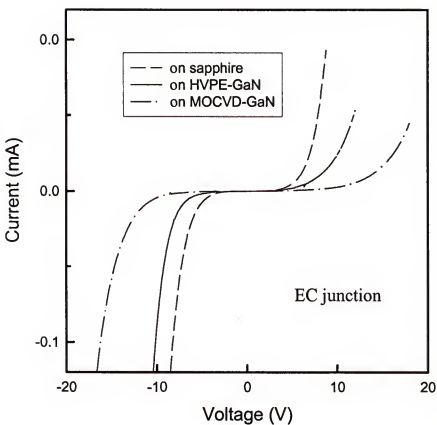


Fig. 7.10 I-V characteristics measured between emitter and collector for HBTs grown on different GaN buffers on sapphire substrates.

displacement of the junction and hence the loss of the advantage of the heterostructure.

Fig. 7.11 shows SIMS profiles of the Al marker (open circle), signifying the position of AlGaN emitter layer, and also the Mg doping profile (solid circle) in the adjacent base region. The base layer is well defined. The so-called “memory effect” associated with the use of Mg¹³¹ is illustrated by the appearance of a spike-like feature in the Mg profile after the Mg has been switched off. We note that growth rate for the n-AlGaN is much lower

than that for the p-GaN base ($\sim 1 \mu\text{m}/\text{hr}$), this would explain the observed enhancement (or spiking) of Mg incorporation during the initial base-emitter transition. It is clear that the reactor memory effect has produced incorporation of Mg in the emitter, although the real situation is not quite as severe as it seems in the data because of "carry-over" of the matrix Al signal during the depth profiling. The fact that HBT characteristics can still be obtained on this material means there is a net surplus of donor over acceptors, and not all of the Mg can be electrically active in the AlGaN. Both the emitter and emitter-contact layers remain n-type.

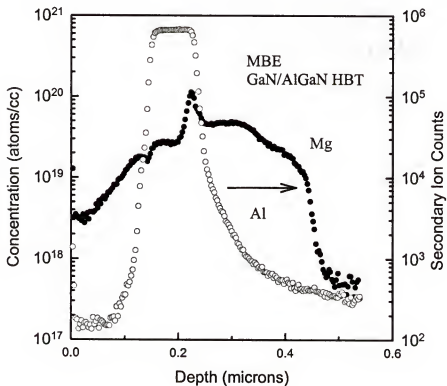


Fig. 7.11 SIMS profile of Mg in MBE grown GaN/AlGaN HBT structures.

Another aspect of impurity control is to minimize the concentration of O (which probably creates a shallow donor state in GaN), C (which may lead to compensated material) and H (which can passivate the Mg acceptors in the base). In MBE grown samples, we usually observe the concentrations of C and O throughout most of the structure are well below that of the intentionally doped Si, suggesting it will have no significant effect on the electrical properties of the material. The incorporation of H is also low, and this is in a contrast to the MOCVD growth, where high concentration residual hydrogen decorates the Mg doping in the base, as shown in Fig. 7.12. This is the case even after the *in situ* activation anneal standard for all MOCVD-grown GaN device structures containing p-layers. We assume in analogy with the behavior of H in other compound semiconductor systems that this anneal dissociates the $(\text{Mg-H})^0$ neutral complexes, producing Mg^+ acceptors and inactive H_2 molecules. Thus, while the hydrogen is still present at a significant concentration in the base, it is not in an active form, and does not effect the electrical properties. It remains to be established as to the relative contributions of background impurities and structural defects to degradation of gain in GaN/AIGaN HBTs.

High specific contact resistance (in particular the p-ohmic contact) is a limiting factor in GaN-based device performance. Fig. 7.13 shows the alloying temperature dependence of the I-V characteristics for Ni/Au contacts to the p-type base layer. Annealing at progressively higher temperatures produced a significant improvement, but the contacts were clearly not purely ohmic and better described as a leaky Schottky contacts. It is noteworthy that 600 °C is the highest annealing temperature can be used in

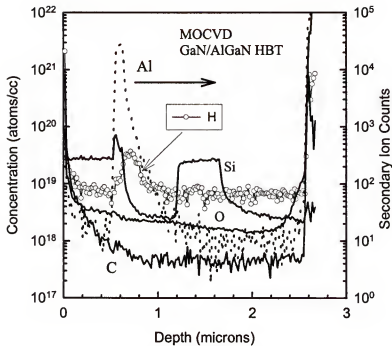


Fig. 7.12 SIMS profiles showing H decorating the base region in an MOCVD grown GaN/AlGaN HBT structure.

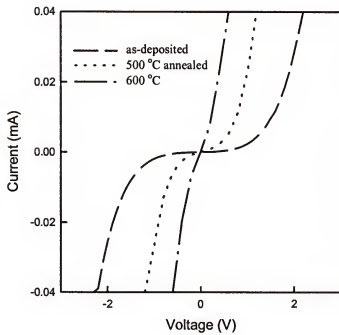


Fig. 7.13 Annealing temperature dependence of I-V characteristics for Ni/Au on the p-type base layer.

most device structures due to junction shorting. In addition, the high sheet resistance in the base due to poor p-type doping could also result in significant parasitic loss, especially when the base layer is thin. Fig. 7.14 shows the typical I-V characteristics at 25 °C and 250 °C from the base-collector and base-emitter junctions of BJTs. Note that there is a kink in the I-V trace for the base-collector junction at ~3.2 V indicating the presence of forward injection current. However, for the base-emitter junction, the forward onset voltage is too high for a pn junction with a built-in potential ~3.2 V indicating high on-resistance. In the former case, the current flows straight down from base contact to collector (similar as in the commercialized GaN LED structure), and the voltage drop on the thin base region is small. However in the latter case, current flows laterally in the base, both high bulk resistivity and current crowding effect limit the carrier transport. The current increases at higher temperatures due to improved thermionic emission as well as higher ionization efficiency of acceptors in the intrinsic and extrinsic base regions.

Regrowth of base contact region or self-aligned base-emitter junction can reduce the extrinsic and intrinsic base resistance, while the key issue is to improve the material quality and p-type doping. Invoking a piezoelectric field to induce free holes in the base is one of potential solutions.¹³²

Minority carrier lifetime is a critical parameter in the gain of bipolar transistors and the conductivity modulation of thyristors. It is also a critical measurement of material quality as it relates to traps and recombination centers. The minority hole lifetime in state-of-the-art n-GaN has been measured to be on the order of 2-7 ns, and the electron lifetime in p-GaN is about one or two orders lower.^{133,134} Bandic et al.¹³⁴ found that line dislocations in unintentionally doped GaN act as recombination sites, and limit the

minority carrier transport properties. As the crystalline quality is improved, better values of the minority carrier lifetime in GaN can be expected.

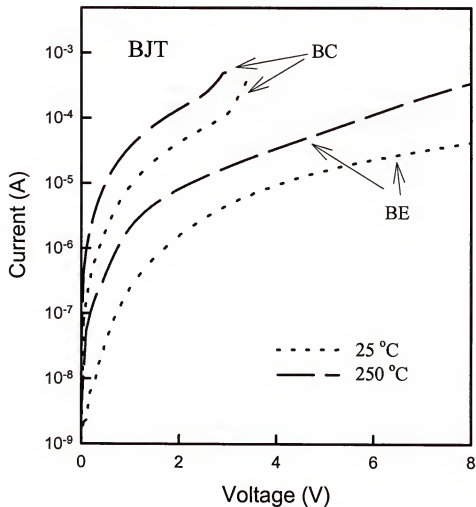


Fig. 7.14 I-V characteristics of base-collector and base-emitter junctions in BJTs at 25 °C or 250 °C.

7.4 Quasi-3D Modeling of Electrical Performance of GaN Bipolar Transistors

In order to gain an understanding of the expected performance of GaN bipolar transistors, we have performed drift-diffusion model-based numerical simulation using ATLAS/BLAZE for AlGaN/GaN HBT and GaN BJT, taking into account carrier statistics, lifetime, mobility and generation-recombination. ATLAS/BLAZE simultaneously solves Poisson's equation and the electron and hole continuity equations over a cross section of the transistor with an iterative Newton-Richardson method.¹³⁵ We chose similar layer structure for the HBT with that previously fabricated and measured. The 2-D transistor cross section with dimensions is shown in Fig. 7.15. Over this cross section, we used a mesh of roughly 1000 nodes with finer meshing near the junctions and in the base region. The simulation employs cylindrical symmetry and is therefore quasi-3D calculation. The model takes into account Schokley-Read-Hall generation-

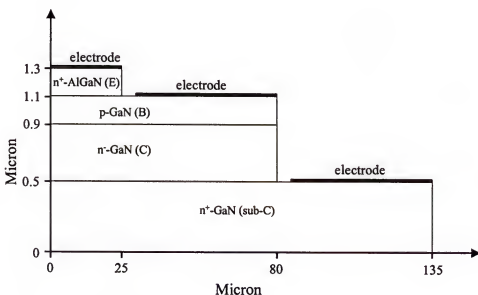


Fig. 7.15 cross-section of a GaN/AlGaN HBT with dimensions.

recombination, Auger and optical processes, concentration dependent low field mobility and lifetime, parallel electric field-dependent mobility, Selberherr's impact ionization and Fermi-Dirac statistics. For high temperature performance, we took into account the temperature dependence of carrier low-field mobility and material bandgap. A list of the parameters employed is shown in Table 7.1 for hexagonal GaN and $\text{Al}_{0.2}\text{Ga}_{0.8}\text{N}$.¹³⁶

Table 7.1 Parameters used in the simulations.

E_g (GaN)	=	3.4 eV (300 K)
N_c (GaN)	=	$2.24 \times 10^{-18} \text{ cm}^{-3}$
V_v (GaN)	=	$1.8 \times 10^{19} \text{ cm}^{-3}$
ε_s (GaN)	=	8.9
v_{sn} (GaN)	=	$2.5 \times 10^7 \text{ cm} \cdot \text{s}^{-1}$
v_{sp} (GaN)	=	$10^6 \text{ cm} \cdot \text{s}^{-1}$
E_{peak} (GaN)	=	$1.4 \times 10^5 \text{ V} \cdot \text{cm}^{-1}$
Richardson constant (GaN)		
A_e^*	=	$26.4 \text{ A} \cdot \text{cm}^{-2} \cdot \text{K}^{-2}$
A_p^*	=	$96 \text{ A} \cdot \text{cm}^{-2} \cdot \text{K}^{-2}$
Auger Recombination Coefficients		
Aug(n)=		$10^{30} \text{ cm}^6 \cdot \text{s}^{-1}$
Aug(p)=		$10^{31} \text{ cm}^6 \cdot \text{s}^{-1}$
GaN/AlGaN band offset ratio		
Q_c	=	0.7
Temperature dependence of bandgap		
$E_g(T) = E_g(300) + 7.32 \times 10^{-4} \left(\frac{300^2}{300 + \beta} - \frac{T^2}{T + \beta} \right)$		
where $\beta = 700K$		
Low field mobility		
$\mu_{no} = \mu_n \left(\frac{T}{300} \right)^{-1.7}$		
$\mu_{po} = \mu_p \left(\frac{T}{300} \right)^{-1.5}$		
Impact ionization (Sellaherr's model): parameters for SiC		
Parameters for AlGaN: $\chi_{\text{Al}_{0.2}\text{Ga}_{0.8}\text{N}} = 0.2\chi_{\text{AlN}} + 0.8\chi_{\text{GaN}}$		

7.4.1 npn Structure

A typical device structure and doping for the npn HBT are shown in Table 7.2.

Since the Mg dopant for the base has a large ionization energy (170 meV), an acceptor concentration approximately an order of magnitude higher than the required hole density is necessary. The material quality is still compromised in currently available GaN due to the high defect concentrations and impurity backgrounds. For this reason we took both the best and typical values for carrier mobility and lifetime in each of the different layers (which have different doping levels), and assumed there was little difference between the values for majority and minority carriers. These range of values are listed in Table 7.3.

Table 7.2 npn GaN/AlGaN HBT structure and doping.

	material	thickness (Å)	doping (cm ⁻³)
emitter	n ⁺ -AlGaN	2000	1×10 ¹⁹
base	p-GaN	2000	2×10 ¹⁷
collector	n ⁻ -GaN	4000	5×10 ¹⁶
subcollector	n ⁺ -GaN	5000	8×10 ¹⁸

Table 7.3 Best and typical values of mobility and lifetime in each layer of the HBT.

	μ _e /μ _h		τ _e /τ _h	
	optimistic	typical	optimistic	typical
emitter	40/5	20/2	1×10 ⁻¹¹ /1×10 ⁻¹⁰	1×10 ⁻¹¹ /5×10 ⁻¹¹
base	600/30	300/14	2×10 ⁻¹⁰ /7×10 ⁻⁹	8×10 ⁻¹¹ /4×10 ⁻⁹
collector	800/40	450/22	1×10 ⁻⁹ /2×10 ⁻⁸	5×10 ⁻¹⁰ /1×10 ⁻⁸
subcollector	200/10	80/4	1×10 ⁻¹¹ /2×10 ⁻¹⁰	1×10 ⁻¹¹ /1×10 ⁻¹⁰

For the layer structure of Table 7.2, the predicted Gummel plots for the HBT are shown at the top of Fig. 7.16 for both the optimistic and typical values of carrier mobility and lifetime. Note that the turn-on voltage is ~ 2.5 V in both cases. The corresponding dc current gains are shown at the bottom of Fig. 7.16, as a function of collector current in devices with 50 μm diameter circular contacts. It is clear that the materials quality can have a tremendous impact on the gain of the device. In the ideal operation region, the gain is ~ 30 for high quality material, but < 10 for more typical structures. Note that even with the best parameters, the calculated gain is limited, probably by the recombination in the base. At high injection levels, the base spreading resistance could result in non-uniform distribution of the emitter current called emitter current crowding. We observed most of the emitter current was concentrated near the edges of the emitter-base junction at current densities $> 10^3 \text{ A}\cdot\text{cm}^{-2}$. Correspondingly, high recombination rates $> 5 \times 10^{25} \text{ cm}^{-2}$ were confined in a small region in the base at the periphery of the junction.

Additional improvements in dc current gain can be obtained by grading the base layer. In Fig. 7.17 we show the results of grading this layer from GaN to $\text{Al}_{0.12}\text{Ga}_{0.88}\text{N}$ linearly, relative to layer of constant compositions. We assumed the optimum values for carrier lifetime and mobility and considered that the transport properties in AlGaN are usually much worse than in GaN. Note that the current gain can reach almost 100 for the graded structure at high current density, at the expense of a slight increase in turn-on voltage. The electron transit time is decreased in the graded structure due to the presence of a quasi-electric field directed from the collector-base junction towards the emitter-base junction (of $\sim 17 \text{ kV}\cdot\text{cm}^{-1}$). In this case, the electrons are transported across the base by diffusion as well as drift.

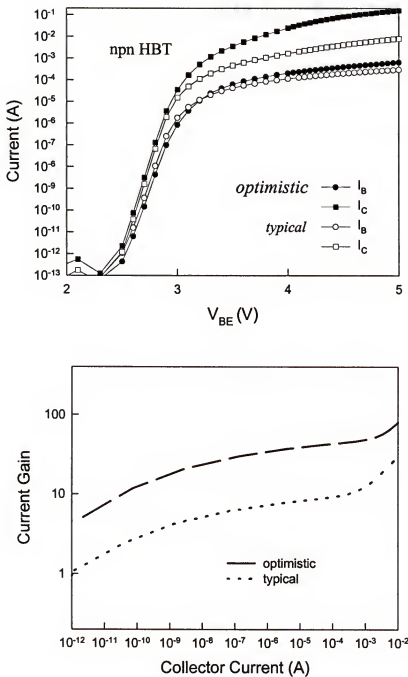


Fig. 7.16 Gummel plot (top) and dc current gain (bottom) for the HBT with structure of Table 7.1, assuming either optimistic or typical values for carrier mobility and lifetime.

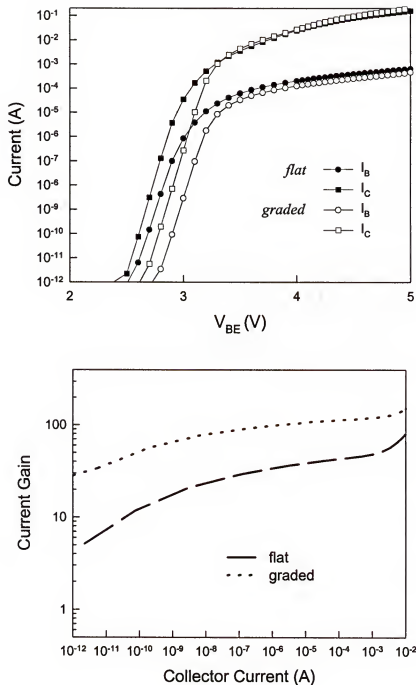


Fig. 7.17 Gummel plot (top) and dc current gain (bottom) for the HBT with structure of Table 7.1, with either a graded or constant composition base layer.

Fig. 7.18 shows the effect on dc current gain of these parameters, namely base thickness (top), minority carrier mobility in the base (center) and minority carrier lifetime in the base (bottom). As expected the gain decreases as the base thickness is increased, due to increased recombination of electrons. Note that with high quality material and a base thickness of 1000 Å, gains of several hundred are possible. There is a direct correlation of gain with the minority carrier mobility, due to the reduced transit time through the base and hence lower recombination, while minority carrier lifetime also has a very strong influence on the device performance. Since GaN is a direct gap material, its minority carrier lifetime would be small. The gain is maximized at low base doping levels in high quality material. When recombination current dominates, we can approximate the common emitter current gain β , as⁷⁶

$$\beta \approx \frac{\tau_e}{\tau_T} \quad (7.1)$$

where τ_e is the electron lifetime in the base and τ_T is the transit time proportional to

$\frac{W_b^2}{\left(\frac{kT}{e}\right)} \cdot \mu_{eb}$. Note that in an ideal HBT, the gain is limited by emitter injection

efficiency, and given by:⁷⁶

$$\beta = \frac{v_{nb} N_{de}}{v_{pe} N_{ab}} \exp(\Delta E_v / kT) \quad (7.2)$$

where v_{nb} and v_{pe} are effective velocities of electrons in the base and holes in the emitter, N_{de} and N_{ab} are doping concentration in the emitter and the base, and ΔE_v is the valence-band offset at the hetero-interface.

Fig. 7.19 shows calculated common-emitter characteristics for a base doping (hole concentration) of $2 \times 10^{17} \text{ cm}^{-3}$ (top), in which the gain is >20 and the Early voltage is ~ 3

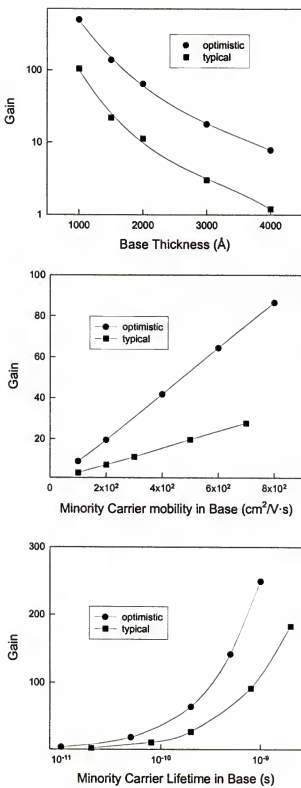


Fig.7.18 Effect on dc current gain of base thickness (top), electron mobility in base (center) or electron lifetime in base (bottom).

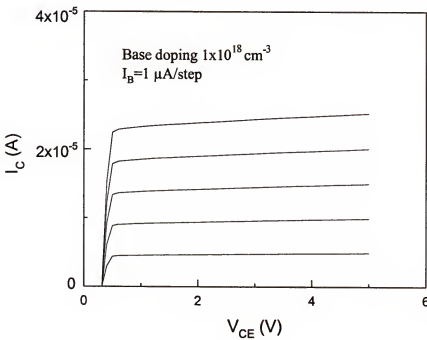
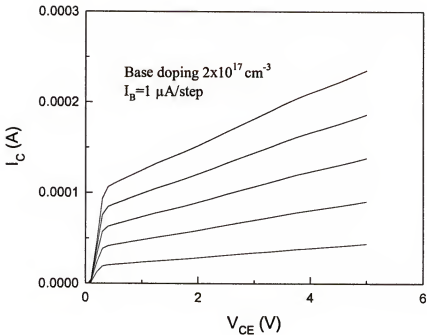


Fig. 7.19 Common-emitter characteristics for the HBT with structure of Table 7.1, for hole concentrations of $2 \times 10^{17} \text{ cm}^{-3}$ (top) or 10^{18} cm^{-3} (bottom) in the base.

V, and for a hole concentration in the base of 10^{18} cm^{-3} (bottom), in which the gain is ~ 5 and the Early voltage becomes much larger because it is proportional to Q_G , the Gummel number. The characteristics do not show good saturation behavior for low base doping due to the base push-out effect.

The relatively high base contact specific resistance is a problem for npn GaN transistors and leads to ohmic heating of the contact/semiconductor interface. This in turn severely degrades the reliability of the device. The typical values of the contact resistance on p-GaN are in the 10^{-2} to $10^{-3} \Omega \cdot \text{cm}^2$ range, but it could be much worse in practical device because high temperature annealing is not applicable. Fig. 7.20 shows the effect of the base contact specific resistance on the Gummel plots from devices with optimum carrier lifetime and mobility. The case of a high base resistance reduces the gain at high current and reduces the low-bias current, emphasizing how important the base contact is in influencing device performance.

The effect of elevated temperature on the Gummel plots is shown in Fig. 7.21 (top). At high temperatures the turn-on decreases, however the gain decreases somewhat due to lower carrier mobility. In the open-base state, the punch-through breakdown voltage BV_{CEO} also decreases from $\sim 18 \text{ V}$ to $\sim 14 \text{ V}$, as shown at the bottom of Fig. 7.21. However, the device operation is still quite good at $300 \text{ }^\circ\text{C}$, and shows the promise of this technology for elevated temperature operation.

Fig. 7.22 shows a comparison of the expected gain for HBT and BJT structures with the same doping and layer thickness. Despite the high band-offset ratio of the AlGaN/GaN heterojunction ($Q_c \sim 0.7$, a high conduction-band spike forms at the hetero-interface which necessitates thermionic emission and tunneling for electron transport

from the n-to-p quasineutral regions), the HBT enjoys a significant advantage in the low injection regime. The results converge at high current densities, and under these conditions the BJT is an attractive alternative because it is simpler to grow.

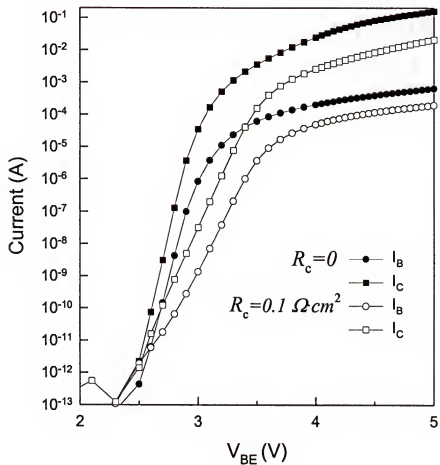


Fig. 7.20 Effect of base contact resistance on Gummel plots.

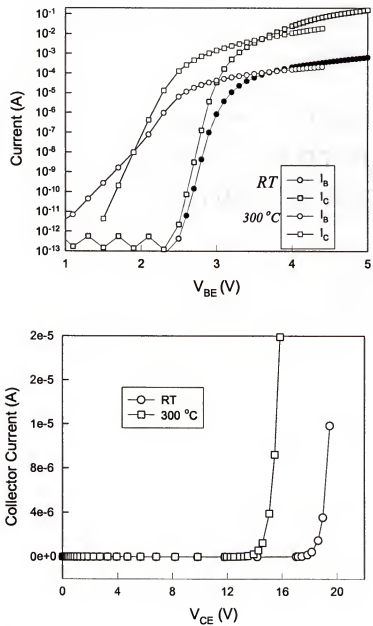


Fig. 7.21 Effect of device operating temperature on Gummel plot (top) or the breakdown voltage of the C-E junction (bottom).

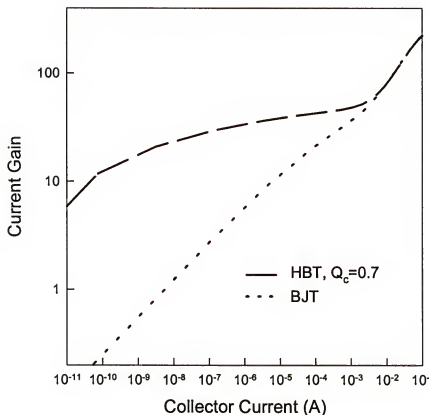


Fig. 7.22 Current gain as a function of collector current for HBT and BJT of the same layer thicknesses and doping.

7.4.2 pnp Structure

One of the limiting factors for npn devices was the high sheet resistance of the base, which results from the large ionization energy of the Mg acceptors in GaN (~170 meV). An obvious alternative is pnp structures, in which the base dopant is a donor (likely Si, ionization energy ~30 meV) and there are fewer problems with obtaining dopant confinement in the base and to achieve a low sheet resistance. The minority hole lifetime is also relatively longer in the base region. In addition, the large conduction-band offset at

the AlGaN/GaN junction can efficiently block the electron current injected from the base to the emitter. The disadvantages to the pnp configuration include much larger hole effective mass and typically very small hole mobility and drift velocity, which might result in a much worse transport coefficient across the base. In this section we describe the results of physically-based modeling of pnp HBTs, in which the same type of analysis has been performed as for the npn structures. The layer structure and the current state-of-the-art values of carrier mobility or lifetime employed for the simulations are shown in Table 7.4 and Table 7.5, respectively. We assumed an emitter contact diameter of 50 μm , and base and collector contact diameters of 100 μm .

Table 7.4 Layer structure and doping for pnp GaN/Al_{0.2}GaN HBT.

	material	thickness (Å)	doping (cm ⁻³)
emitter	p-AlGaN	2000	5×10 ¹⁷
base	n-GaN	1000/2000	2×10 ¹⁷ (1×10 ¹⁸)
collector	p ⁻ -GaN	4000	2×10 ¹⁶
subcollector	p-GaN	5000	1×10 ¹⁸

Table 7.5 Typical values of carrier mobility and lifetime in the various layers of the HBT.

	μ_e/μ_h	τ_e/τ_h
emitter	40/4	4×10 ⁻¹¹ /1×10 ⁻⁹
base	300/14 (150/7)	1×10 ⁻¹⁰ /4×10 ⁻⁹ (2×10 ⁻¹¹ /1×10 ⁻⁹)
collector	550/27	8×10 ⁻¹⁰ /3×10 ⁻⁸
subcollector	150/7	2×10 ⁻¹¹ /1×10 ⁻⁹

The first point of interest is the effect of the contact geometry. In structures grown on sapphire substrates the contact has to be on the top surface of the sub collector. By contrast, if a p-type conducting GaN substrate were available, the collector contact could be placed on the bottom of the subcollector (which would be the substrate in this case). The latter geometry provides a more vertical current flow through the device. Fig. 7.23 shows the Gummel plots (top) and current gain as a function of collector current (bottom) for pnp HBTs with 2000 Å thick base layers with doping of $2 \times 10^{17} \text{ cm}^{-3}$. The gains are identical for the two contact geometries for low current densities, but at high current levels the bottom contact structure is clearly superior. Fig. 7.24 shows the distribution of the streamlines of the emitter current (top) and the recombination rates (bottom) at high injection regime for the side contact structure. There is a significant current loss in the base region, and in the subcollector where the current flow changes direction. High recombination occurs due to the current crowding around the turning point. Note that this is only observed in the pnp structures, where the carrier mobility is very low. In a contrast, the emitter current distributes uniformly in the bottom contact structure, as shown in Fig. 7.25. The recombination rates are detectable only in the base layer, as observed in the npn structures.

In Fig. 7.26 we examine the effect of minority carrier mobility in the base (top), base thickness (center) and minority carrier lifetime in the base (bottom). A dc gain of ~ 50 is obtained at a base thickness of 1000 Å, but it decreases for thicker layers due to increased recombination. The results clearly show that material quality, which will effect the minority carrier lifetime and mobility, has a strong influence on the device performance. State-of-the-art GaN still contains high concentrations of residual

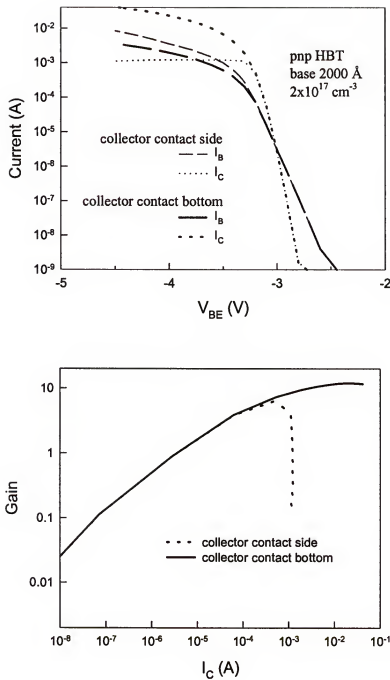


Fig. 7.23 Gummel plot (top) and dc current gain (bottom) for the pnp HBT with structure of Table 7.4, with the collector contact either on top (i.e. to be side of the e and b contacts) or bottom of the sub-collector layer.

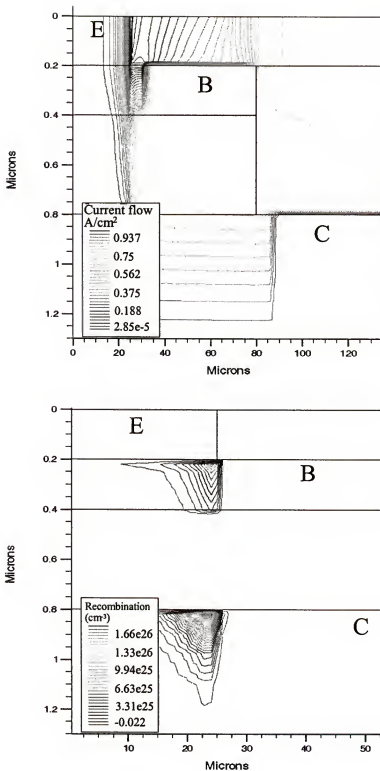


Fig. 7.24 Distribution of the current streamlines (top) and the recombination rates (bottom) at high injection regime for the pnp HBT with side collector contact structure.

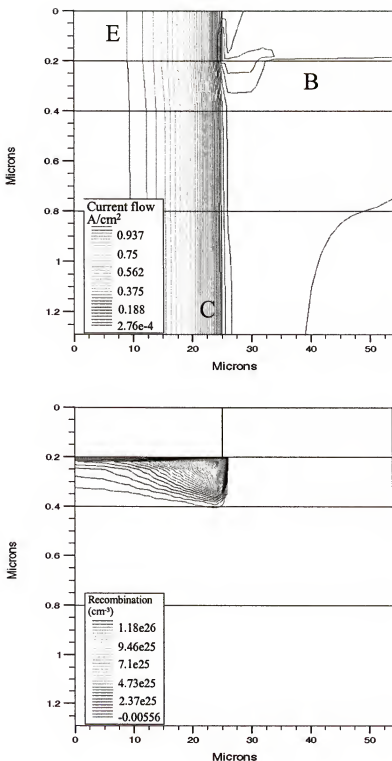


Fig. 7.25 Distribution of the current streamlines (top) and the recombination rates (bottom) at high injection regime for the pnp HBT with bottom collector contact.

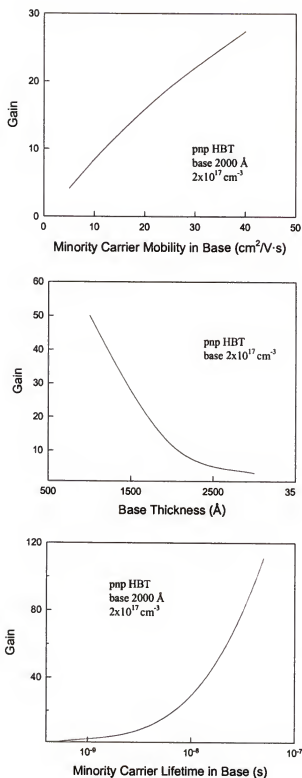


Fig. 7.26 Effect on dc current gain of base thickness (top), electron mobility in base (center) or electron lifetime in base (bottom) in the pnp HBT.

impurities such as O, C, H and Si and obviously has high densities of threading dislocations and other extended defects. As the growth purity and perfection continues to improve, one can expect better HBT performance.

The effect of base doping is shown in Fig. 7.27 for two different doping levels (10^{17} or 10^{18} cm $^{-3}$). We used a base thickness of 1000 Å in these simulations. For the lower doping concentration there is obvious base push-out in the common-emitter characteristics. The Early voltage is ~ 3 V for the 10^{17} cm $^{-3}$ base doping, whereas for the higher doping level it was too large to measure. The Early voltage is roughly proportional to the Gummel number, Q_G , and the base width.

The effect of base thickness on the collector-emitter breakdown voltage is shown in Fig. 7.28 for a fixed doping level of 2×10^{17} cm $^{-3}$. There is a significant increase in breakdown voltage as base thickness increases. This information is useful in designing HBTs for particular application in which either power or switching speed is most important. In the former case, it is desirable to have high breakdown voltage, whereas in the latter, a thin base is necessary.

Since one of the expected attributes of GaN/AlGaN HBTs is ability to operate at high temperatures, it is interesting to investigate the trade-off in performance at elevated temperatures. Fig. 7.29 shows Gummel plots (top) and the resultant dc current gains as a function of collector current (bottom) for 25 °C and 300 °C operation. The gain decreases by about 25% between these two temperatures, and gain at high current density remained above 10 to a temperature of ~ 475 °C. It is quite clear that the transistor gain is limited primarily by the recombination current (eq. 7.1). The decrease in the gain can be explained by the temperature variation of the mobility, which leads to a temperature

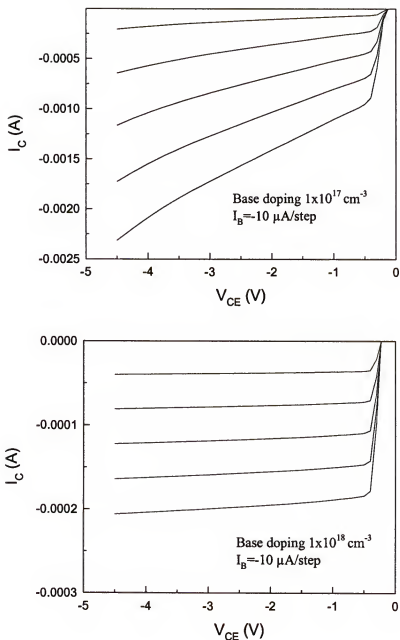


Fig. 7.27 Common-emitter characteristics for the pnp HBT with structure of Table 7.4, for hole concentrations of $2 \times 10^{17} \text{ cm}^{-3}$ (top) or 10^{18} cm^{-3} (bottom) in the base.

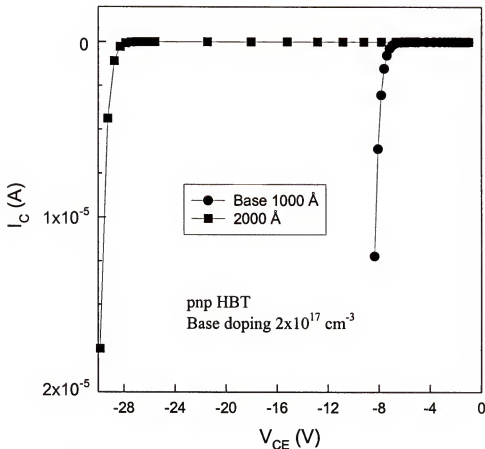


Fig. 7.28 Effect of base thickness on the reverse breakdown voltage of the CE junction in the pnp HBT.

variation of the diffusion constant and transit time in the base. Otherwise, if the gain is limited by the emitter current efficiency, as described by eq. 7.2, a much larger temperature dependence of the gain would be expected.

Fig. 7.30 shows a comparison of the current gain for pnp and npn devices with identical layer structures and doping levels, as a function of collector current. At low

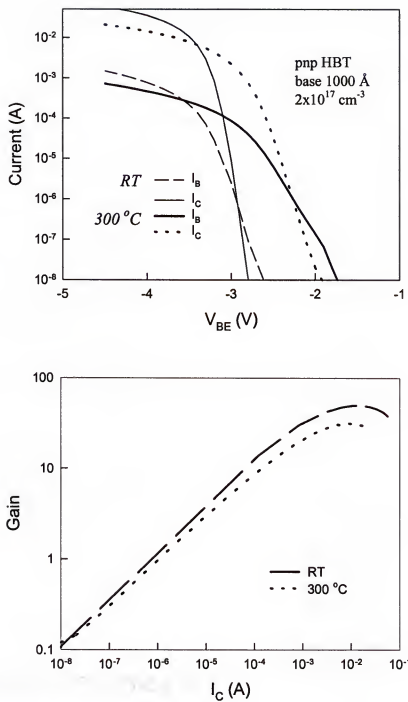


Fig. 7.29 Effect of device operating temperature on Gummel plots (top) and dc current gain (bottom) of the pnp HBT.

injection levels the npn device has a clear advantage, whereas at high current densities the difference is relatively small. From practical point of view, the pnp structure is attractive at this point because it does not suffer from high base resistances.

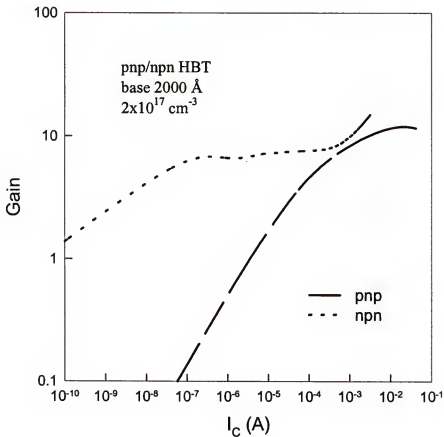


Fig. 7.30 Comparison of dc current gain as a function of collector current for npn and pnp GaN/AlGaN HBTs with the same doping and thickness.

CHAPTER 8

CONCLUSIONS AND FUTURE TRENDS

Recognized for their stability in harsh environments and their unique optical and electronic properties, the III-V nitrides have become one of the few select classes of materials being engineered into optoelectronics and microelectronic devices demanded by today's technologically advancing society. Although early progress was slowed by the lack of ideal substrates and p-type doping ability, the pace of successful GaN-based device fabrication has accelerated within the last few years. The commercialization of blue and green LEDs, and the achievement of long lifetime laser diodes have been followed by the realization of UV photodetectors and numerous different electronic devices. However, the scientific understanding necessary to routinely reproduce these results and advance device performance is still lacking in many critical areas. While further improvement in heteroepitaxial growth is currently gaining considerable attention, reliable processing procedure is another critical factor for GaN to reach its full potential, especially for microwave power electronics. This dissertation has focused on several important aspects of GaN processing, with efforts directed towards optimizing GaN technology and improving GaN-based device performance.

A novel rapid thermal processing at temperatures up to 1500 °C has been developed for GaN and related materials. High quality AlN has proven to be efficient encapsulant at these temperatures, and can be removed selectively in KOH solutions. High dose Si implant followed by 1400 °C annealing produced metallic doping levels ($\sim 5 \times 10^{20} \text{ cm}^{-3}$)

in GaN. Post-implant annealing at 1100 °C was found to be insufficient to remove the lattice damage, while 1400 °C produced much lower defect densities. The implantation and activation of other common donors and acceptors in GaN have also been examined. The group VI donors, though free of the potential drawback of being amphoteric, did not show any advantages over Si for creation of n-type doping in GaN. Only Mg was found to produce p-type conductivity, while C and Be-implanted samples remained n-type due to strong compensation effects. None of the implanted species showed measurable diffusion at high temperatures, but Be did display an apparent defect assisted redistribution at 900 °C. A summary of these results are shown in Table 8.1.

To fully develop the potential of ion implantation in advanced electronics, there is still a need to further examine the possible implanted dopants in GaN, especially to improve p-type doping efficiency in GaN or AlGaN. One attractive technique is to improve the occupation of dopants on the desirable lattice sites through co-implantation, such as co-implantation of C, Ge or Sn with group III species for more conducting p-type nitrides, and co-implantation of Si and group VI dopants to get even better n-type conductivity.

High sheet resistances of $\sim 10^{12} \Omega/\square$ in n-GaN and $10^{10} \Omega/\square$ in p-GaN have been achieved by implantation of O, Cr, Fe and Ti. The concentration of electrically active deep energy levels related to the chemical nature of these species was found to be $< 7 \times 10^{17} \text{ cm}^{-3}$, and the implanted GaN displayed typical damage-related isolation behavior. Temperature-dependent measurements showed that the defect levels are in the range of 0.2-0.49 eV in n-GaN, and ~ 0.44 eV in p-GaN, which are far from midgap, but sufficient to produce high resistivity materials. Future work in the area of implant

Table 8.1 Ion implantation doping in GaN.

DONORS	MAX ACHIEVABLE DOPING LEVEL (cm ⁻³)	DIFFUSIVITY (cm ² ·s ⁻¹)	IONIZATION LEVEL (meV)
Si	5×10 ²⁰	<2×10 ⁻¹³ (1500 °C)	28
S	5×10 ¹⁸	<2×10 ⁻¹³ (1400 °C)	48
Se	2×10 ¹⁸	<2×10 ⁻¹³ (1450 °C)	—
Te	1×10 ¹⁸	<2×10 ⁻¹³ (1450 °C)	50
O	3×10 ¹⁸	<2×10 ⁻¹³ (1200 °C)	30
ACCEPTORS			
Mg	~5×10 ¹⁷	<2×10 ⁻¹³ (1450 °C)	170
Be	n-type	Defect-assisted	165
C	n-type	<2×10 ⁻¹³ (1400 °C)	—

isolation includes search for high compensation in InGaN and thermally stable isolation for use at elevated temperatures.

Effects of surface cleanliness on characteristics of GaN Schottky diodes have been investigated. The reduction in SBH by an additional (NH₄)₂S treatment was correlated with removal of the native oxide that forms an insulating layer on the conventionally-cleaned GaN. Surface treatments, which have a strong influence on the electrical performance of metal contacts, could be critical for formation of high quality ohmic contacts to p-type GaN.

W-based contacts deposited on Si-implanted GaN produced ohmic contacts with low resistance of $10^{-6} \Omega\text{-cm}^2$. Minimal reaction at the W/GaN interface was observed even at 1000 °C. The behavior of W and WSi on p-type GaN has been compared with that of Ni/Au. True ohmic characteristics were obtained only at elevated temperatures. The refractory contact schemes offer superior thermal stability to the standard metallization used in photonic devices, Ti/Al and Ni/Au, and therefore are very promising for GaN-based ultra-high-power electronics. At this point, difficulty in achieving low resistance p-type ohmic is still one of the major obstacles in fabricating efficient photonic devices. Further improvements in this area must be achieved at the next stage, including better understanding of metal/GaN reactions and use of these reactions for tunneling and/or lowering barrier height, exploring and incorporating a graded structure or superlattice layer, or highly doped material with narrower band gap for ohmic contacts.

Dry etch damage is another key issue for optimization of GaN processing. In this work, plasma damage in n- and p- GaN has been studied systematically using Schottky diode measurements. ICP discharges (including real etching chemistries) produced large changes in diode characteristics. The results are consistent with creation of nitrogen vacancy -- related shallow donors in the near surface region (<600 Å), which decrease the doping concentration in p-GaN and increase electron density in n-GaN. Surface type conversion was observed in p-GaN at high ion fluxes and high ion energies. The damage was found to accumulate rapidly, and ion mass appeared to be a key parameter in determining the magnitude in degradation of material properties. Annealing at ~750 °C for n-GaN and 850 °C for p-GaN, or wet chemical etching have proven to be efficient for

damage removal. For GaN-based microelectronics, other promising low damage etching such as low energy electron-enhanced etching¹³⁷ or photo-assisted vapor etching,¹³⁸ could become alternative techniques and attract more and more attention in the future.

GaN-based bipolar transistors and power switches are particularly susceptible to the relative immaturity of current-state material growth and fabrication technology. The commercialization of these devices may still be years away. Based on the technical improvements we achieved, attempts were made to demonstrate MBE-grown GaN/AlGaN HBT and GaN BJT. The devices operated at current densities up to 3.6 kA·cm⁻² and temperatures up to 300 °C, with high common-base injection efficiency. The key issues which currently limit the device performance, such as high base resistance, poor doping and impurity control, and defects resulting from the heteroepitaxial growth, have been addressed. Physically-based simulation has showed that GaN-based bipolar transistors may still suffer from small minority carrier lifetime even if the aforementioned processing problems are sufficiently overcome. During the next few years, with continued rapid development in material growth, there is every reason to believe that major progress will be made on the electronic device front.

GaN and related materials provide exciting opportunities in material research and device engineering, and are perhaps a model system for the interplay between science and technology. In the photonics arena, device applications have appeared before there was a complete understanding of the growth and defect issues. Today, research regarding the III-V nitride materials is focused on the optimization of these and other devices, and realization of their theoretical potential; thus, methods to improve heteroepitaxial growth and critical advances in processing technology are once again at the forefront.

REFERENCES

1. H. Morkoc, S. Strite, G. B. Gao, M. E. Lin, B. Sverdlov and M. Burns, *J. Appl. Phys.* **76** 1363 (1994).
2. T. P. Chow and R. Tyagi, *IEEE Trans. Electron. Dev.* **41** 1481 (1994).
3. Z. Z. Bandic, P. M. Bridger, E. C. Piquette, T. C. McGill, R. P. Vaudo, V. M. Phanse, J. M. Redwing, *Appl. Phys. Lett.* **74** 1266 (1998).
4. R. Gaska, J. W. Yang, A. Osinsky, Q. Chen, M. A. Khan, A. O. Orlov, G. L. Snider and M. S. Shur, *Appl. Phys. Lett.* **72** 707 (1998).
5. Y. Uzawa, Z. Wang, A. Kawakami and B. Komiyama, *Appl. Phys. Lett.* **66** 1992 (1995).
6. O. Ambacher, *J. Phys. D* **31** 2653 (1998).
7. S. Fischer, A. Gisbertz, B. K. Meyer, M. Topf, S. Koynov, I. Dirnstorfer, D. Volm, R. Ueckev, P. Reiche, *Symp. Proc. EGN-1*, 1996.
8. P. Kung, A. Saxler, X. Zhang, D. Walker, R. Lavado and M. Razaghi, *Appl. Phys. Lett.* **69** 2116 (1996).
9. W. Gotz, L. T. Romano, J. Walker, N. M. Johnson, R. J. Molnar, *Appl. Phys. Lett.* **72** 1214 (1998).
10. C. Wetzel, D. Volm, B. K. Meyer, K. Pressel, S. Nilsson, E. N. Mokhov, P. G. Baranov, *Appl. Phys. Lett.* **65** 1033 (1994).
11. Y. A. Vodakov, E. N. Mokhov, A. D. Roenkov, M. E. Boiko and P. G. Baranov, *J. Cryst. Growth* **10** 183 (1998).
12. T. D. Moustakas, T. Lei and R. J. Molnar, *Physica B* **185** 39 (1993).
13. J.M. Van Hove, R. Hickman, J.J. Klaassen, P.P. Chow and P.P. Ruden, *Appl. Phys. Lett.* **70** 282 (1997).
14. M. Ilegems, *J. Cryst. Growth* **13/14** 360 (1972).

15. M. Morita, S. Isogai, N. Shimizu, K. Tsubouchi and N. Mikohiba, *Jpn. J. Appl. Phys.* **19** L173 (1981).
16. H. Amano, N. Sawaki, I. Akasaki and Y. Toyada, *Appl. Phys. Lett.* **48** 353 (1986).
17. S. Keller, P. B. Keller, Y. F. Wu, B. Heying, D. Kapolnek, J. S. Speck, U. K. Mishra and S. P. DenBaars, *Appl. Phys. Lett.* **68** 1525 (1996).
18. S. Nakamura, T. Mukai and M. Senoh, *Appl. Phys. Lett.* **64** 1687 (1994).
19. Y. Kato, S. Kitamura, K. Hiramatsu and N. Sawaki, *J. Cryst. Growth* **144** 133 (1994).
20. H. Marchand, J. P. Ibbetson, P. T. Fini, P. Kozodoy, S. Keller, S. DenBaars, J. S. Speck and U. K. Mishra, *Mat. Res. Soc. Inter. J. Nitride Semi. Res.* **3** 3 (1998).
21. R. Madar, G. Jacob, J. Hallais and R. Frucgart, *J. Cryst. Growth* **31** 197 (1975).
22. J. Karpinski, S. Porowski, S. Miotkowska, *J. Cryst. Growth* **56** 77 (1982).
23. J. Burm, K. Chu, W. Davis, W. J. Schaff, L. F. Eastman, T. J. Eustis, *Appl. Phys. Lett.* **70** 464 (1997).
24. D. L. Rode and D. K. Gaskill, *Appl. Phys. Lett.* **66** 1972 (1995).
25. J. D. Albrecht, R. P. Wang, P. P. Ruden, M. Farahmand and K. F. Brennan, *J. Appl. Phys.* **83** 4777 (1998).
26. R. J. Molnar and T. D. Moustakas, *Bull. Am. Phys. Soc.* **38** 445 (1993).
27. W. Gotz, N. M. Johnson, J. Walker, D. P. Bour, H. Amano and I. Akasaki, *Appl. Phys. Lett.* **67** 2606 (1995).
28. H. Amano, M. Kito, K. Hiramatsu and I. Akasaki, *Jpn. J. Appl. Phys.* **28** L2112 (1989).
29. S. Nakamura, T. Muskai, M. Senoh and N. Iwasa, *Jpn. J. Appl. Phys.* **31** L139 (1992).
30. S. J. Pearton, C. R. Abernathy, C. B. Vartuli, J. C. Zolper, C. Yuan and R. A. Stall, *Appl. Phys. Lett.* **67** 1435 (1995).
31. J. C. Zolper, R. G. Wilson, S. J. Pearton and R. A. Stall, *Appl. Phys. Lett.* **68** 1945 (1996).
32. O. Brandt, H. Yang, H. Kostal and K. Ploog, *Appl. Phys. Lett.* **69** 2707 (1996).

33. S. Nakamura, T. Muskai and M. Senoh, *Appl. Phys. Lett.* **67** 1868 (1995).
34. S. Nakamura, M. Senoh, N. Iwasa, S. Nagahama, T. Yamada and T. Muskai, *Jpn. J. Appl. Phys.* **10B** L1332 (1995).
35. S. Nakamura, M. Senoh, S. I. Nagahama, N. Iwasa, T. Yamada, T. Matsushita, H. Kiyoku and Y. S. Ugimoto, *Jpn. J. Appl. Phys.* **35** L217 (1996).
36. S. Nakamura, M. Senoh, S. I. Nagahama, N. Iwasa, T. Yamada, T. Matsushita, H. Kiyoku and Y. S. Ugimoto, *Appl. Phys. Lett.* **68** 2105 (1996).
37. S. Nakamura, M. Senoh, S. I. Nagahama, N. Iwasa, T. Yamada, T. Matsushita, H. Kiyoku, Y. S. Ugimoto, T. Kozaki, H. Umemoto, M. Sano and K. Chocho, *Appl. Phys. Lett.* **72** 211 (1998).
38. M. A. Khan, A. R. Bhattarai, J. N. Kuznia and D. T. Olson, *Appl. Phys. Lett.* **63** 1214 (1993).
39. M. A. Khan, J. N. Kuznia, D. T. Olson, W. Schatt, J. Burm and M. S. Shur, *Appl. Phys. Lett.* **65** 1121 (1994).
40. S. T. Sheppard, K. Doverspike, W. L. Pribble, S. T. Allen, J. W. Palmour, L. T. Kehias and T. J. Jenkins, *IEEE Electron. Dev. Lett.* **20** 161 (1999).
41. L. Daumiller, C. Kirchner, M. Kamp, K. J. Ebeling, L. Pond, C. E. Weitzel and E. Kohn, *56th Dev. Res. Conf.*, Charlottesville, VA, 1998.
42. P. M. Asbeck, E. T. Yu, S. S. Lau, G. J. Sulliran, J. M. Van Hove, J. Redwing, *Electron Lett.* **33** 1230 (1997).
43. B. E. Foutz, L. F. Eastman, U. V. Bhapkar and M. S. Shur, *Appl. Phys. Lett.* **70** 2849 (1997).
44. M. A. Khan, T. N. Kuznia, A. R. Bhattaraia and D. T. Olson, *Appl. Phys. Lett.* **62** 1786 (1993).
45. S. C. Binari, L. B. Rowland, W. Kruppa, G. Kelner, K. Doverspike and D. K. Gaskill, *Electron. Lett.* **30** 1248 (1994).
46. J. C. Zolper, R. J. Shul, A. G. Baca, R. G. Wilson, S. J. Pearton and R. A. Stall, *Appl. Phys. Lett.* **68** 2273 (1996).
47. S. C. Binari, *Electrochem. Soc. Proc.* **95-21** 136 (1995).

48. F. Ren, M. Hong, S. N. G. Chu, M. A. Marcus, M. J. Schurman, A. G. Baca, S. J. Pearton and C. R. Abernathy, *Appl. Phys. Lett.* **73** 3893 (1999).
49. L. S. McCarthy, P. Kozodoy, M. J. W. Rodwell and S. P. DenBaars, *IEEE Electron. Dev. Lett.* **20** 277 (1999).
50. J. Han, A. G. Baca, R. J. Shul, C. G. Willison, L. Zhang, F. Ren, A. Zhang, G. Dang, S. M. Donovan, X. A. Cao, H. Cho, K. B. Jung, C. R. Abernathy, S. J. Pearton and R. G. Wilson, *Appl. Phys. Lett.* **74** 2702 (1999).
51. J. C. Zolper, J. Han, R. M. Biefeld, S. B. Van Deusen, W. R. Wampler, D. J. Reiger, S. J. Pearton, J. S. Williams, H. H. Tan and R. Stall, *J. Electron. Mater.* **27** 179 (1998).
52. S. C. Binari, H. B. Dietrich, G. Kelner, L. B. Rowland, K. Doverspike and D. K. Wickenden, *J. Appl. Phys.* **78** 3008 (1995).
53. J. C. Zolper, S. J. Pearton, C. R. Abernathy and C. R. Vartuli, *Appl. Phys. Lett.* **66** 3042 (1995).
54. Q. Z. Liu and S. S. Lau, *Solid-State Electron.* **42** 677 (1998).
55. M. E. Lin, Z. Ma, F. Y. Huang, Z. F. Fan, L. H. Allen and H. Morkoc, *Appl. Phys. Lett.* **61** 1003 (1994).
56. V. M. Bermudez, R. Kaplan, M. A. Khan and J. N. Kuznia, *Phys. Rev. B* **48** 2436 (1993).
57. A. C. Schmitz, A. T. Ping, M. A. Khan, Q. Chen, J. W. Yang and I. Adesida, *Electron. Lett.* **32** 1832 (1996).
58. Q. Z. Liu, L. S. Ya, S. S. Lau, J. M. Redwing, N. R. Perkins and T. F. Kuech, *Appl. Phys. Lett.* **70** 1275 (1997).
59. J. S. Foresi and T. D. Moustakas, *Appl. Phys. Lett.* **62** 2859 (1993).
60. I. Adesida, A. Mahajan, E. Andideh, M. A. Khan, D. T. Olsen and J. N. Kuznia, *Appl. Phys. Lett.* **63** 2777 (1993).
61. R. J. Shul, G. B. McClellan, S. J. Pearton, C. R. Abernathy, C. Constantine, C. Barratt, *Electron. Lett.* **32** 1408 (1996).
62. R. J. Shul, G. B. McClellan, S. A. Casalnoro, D. J. Rieger, S. J. Pearton, C. Constantine, C. Barratt and R. K. Karlicek, *Appl. Phys. Lett.* **69** 1119 (1996).
63. S. J. Pearton, C. R. Abernathy and F. Ren, *Appl. Phys. Lett.* **64** 2294 (1994).

64. S. J. Pearton, *Inter. J. Modern Phys. B* 7 4687 (1993).
65. L. A. Christel and J. F. Gibbons, *J. Appl. Phys.* 52 5050 (1981).
66. H. H. Tan, J. S. Williams, J. Zou, D. J. H. Cockayne, S. J. Pearton and R. A. Stall, *Appl. Phys. Lett.* 69 2364 (1996).
67. H. H. Tan, C. Jagadish, J. S. Williams, J. Zou, D. J. H. Cockayne and A. Sikorski, *J. Appl. Phys.* 77 87 (1995).
68. M. W. Focht, A. T. Macrander, B. Schwartz and L. C. Feldman, *J. Appl. Phys.* 55 3859 (1984).
69. *Handbook of Chemistry and Physics*, ed. R. C. Weast, P E92, 1983.
70. S. J. Pearton, F. Ren, R. J. Shul, J. C. Zolper and A. Katz, *Mat. Res. Soc. Symp. Proc.* 468 331 (1997).
71. S. Porowski and I. Grzegory, in *GaN and Related Materials*, ed. S. J. Pearton (Gordon and Breach, NY 1997).
72. J. C. Zolper, J. Han, S. B. Van Deusen, M. H. Crawford, R. M. Biefeld, J. Jun, T. Suski, J. M. Baranowski and S. J. Pearton, 1997 Fall MRS Meeting, Boston, Dec. 1997.
73. J. C. Zolper, D. J. Reiger, A. G. Baca, S. J. Pearton, J. W. Lee and R. A. Stall, *Appl. Phys. Lett.* 69 538 (1996).
74. J. R. Mileham, S. J. Pearton, C. R. Abernathy, J. D. MacKenzie, R. J. Shul and S. P. Kilcoyne, *Appl. Phys. Lett.* 67 1119 (1995).
75. S. M. Sze, *Physics of Semiconductor Devices*, 2nd edition, 1981.
76. M. S. Shur, *Physics of Semiconductor Devices*, 1990.
77. K. K. Shih, J. M. Blum, *Solid-State Electron.* 15 1177 (1971).
78. J. I. Pankove and J. A. Hutchby, *Appl. Phys. Lett.* 24 281 (1974).
79. H. P. Maruska, M. Lioubtchenko, T. G. Tetreault, M. Osinski, S. J. Pearton, M. Schurman, R. Vando, S. Sakai, Q. Chen and R. J. Shul, *Mat. Res. Soc. Symp.* 483 345 (1998).
80. H. H. Tan, J. S. Williams, J. Zou, D. J. H. Cockayne, S. J. Pearton, J. C. Zolper and R. A. Stall, *Appl. Phys. Lett.* 72 1190 (1998).

81. C. R. Abernathy, *Mat. Sci. Eng. R* **14** 203 (1995).
82. C. C. Yi and B. W. Wessels, *Appl. Phys. Lett.* **69** 3026 (1996).
83. P. Bogulawski, E. L. Briggs and J. Bernholc, *Phys. Rev. B* **51** 17255 (1995).
84. C. R. Abernathy, J. D. MacKenzie, S. J. Pearton and W. S. Hobson, *Appl. Phys. Lett.* **66** 1969 (1995).
85. R. G. Wilson, S. J. Pearton, C. R. Abernathy and J. M. Zavada, *Appl. Phys. Lett.* **66** 2238 (1995).
86. M. D. Deal and H. G. Robinson, *Appl. Phys. Lett.* **55** 1990 (1989).
87. H. G. Robinson, M. D. Deal and D. A. Stevenson, *Appl. Phys. Lett.* **58** 2000 (1991).
88. H. G. Robinson, M. D. Deal, P. B. Griffin, G. Amaratunga, P. B. Griffin, D. A. Stevenson and J. D. Plummer, *J. Appl. Phys.* **71** 2615 (1992).
89. S. J. Pearton, *Int. J. Mod. Phys. B* **4** 4687 (1993).
90. M. D. Deal, C. J. Hu, C. C. Lee and H. G. Robinson, *Mat. Res. Soc. Symp.* **300** 365 (1993).
91. J. C. Zolper, J. Han, S. B. Van Deusen, R. M. Biefeld, M. H. Crawford, J. Han, T. Suski, J. M. Baranowski and S. J. Pearton, *Mat. Res. Soc. Symp. Proc.* **482** 609 (1998).
92. G. Harrington, Y. Hsin, Q.Z. Liu, P.M. Asbeck, S.S. Lau, M.A. Khan, J.W. Yang and Q. Chen, *Electron. Lett.* **34**, 193 (1998).
93. S.J. Pearton, M.P. Iannuzzi, C.L. Reynolds and L. Peticolas, *Appl. Phys. Lett.* **52**, 395 (1988).
94. J.C. Zolper, M.E. Sherwin, A.G. Baca and R.P. Schneider, *J. Electron. Mater.* **24**, 21 (1995).
95. M. Cohen, H. Fritsche and S. Ovshinsky, *Phys. Rev. Lett.* **22**, 1065 (1969).
96. S. J. Pearton, *Mat. Sci. Rep.* **4** 313 (1990).
97. *Identification of Defects in Semiconductors*, ed. M. Stavola, *Semiconductors and Semimetals*, Vols. 51A and 51B (Academic Press, San Diego, 1998).

98. K. Pressel and P. Thurian, in *Properties, Processing and Applications of GaN and Related Semiconductors*, ed. J.H. Edgar, S. Strite, I. Akasaki, H. Amano and C. Wetzel (EMIS DataReview 23, INSPEC, IEE, London, 1999).
99. Z. Fan, S. N. Mohammad, W. Kim, O. Aktas, A. E. Botchkarev and H. Morkoc, *Appl. Phys. Lett.* **68** 1672 (1996).
100. V. S. Fomenko, *Emission Properties of Materials*, Naukova Dumka, Kiev 1981.
101. H. Ishikawa, S. Kobayashi, Y. Koide, S. Yamasaki, S. Nagai, J. Umezaki, M. Koike and M. Murakami, *J. Appl. Phys.* **81** 1315 (1997).
102. K. V. Vassilevski, M. G. Rastegaeva, A. I. Babanin, I. P. Nikitina and V. A. Dmitriev, *MRS Internet J. Nitride Semicond. Res.* **1** 38 (1996).
103. T. Mori, T. Kozawa, T. Ohwaki, Y. Taga, S. Nagai, S. Yamasaki, S. Asami, N. Shibata and M. Koike, *Appl. Phys. Lett.* **69** 3537 (1996).
104. T. Kim, J. Khim, S. Chae and T. Kim, *Mat. Res. Soc. Symp. Proc.* **468** 427 (1997).
105. D. J. King, L. Zhang, J. C. Ramer, S. D. Hersee and L. F. Lester, *Mat. Res. Soc. Symp. Proc.* **468** 421 (1997).
106. L. L. Smith, R. F. Davis, M. J. Kim, R. W. Carpenter and Y. Huang, *J. Mater. Res.* **12** 2249 (1997).
107. Y. Koide, T. Maeda, T. Kawakami, S. Fujita, T. Uemura, N. Shibata and M. Murakami, *J. Electron. Mater.* **28** 341 (1999).
108. J. -K. Ho, C. -S. Jong, C. C. Chiu, C.-N. Huang, C. -Y. Chen and K. -K Shih, *Appl. Phys. Lett.* **74** 1275 (1999).
109. J. K. Kim, J. -L. Lee, J. W. Lee, H. E. Shin, Y. J. Park and T. Kim, *Appl. Phys. Lett.* **73** 2953 (1998).
110. J. -L. Lee, M. Weber, J. K. Kim, J. W. Lee, Y. J. Park, T. Kim and K. Lynn, *Appl. Phys. Lett.* **74** 2289 (1999).
111. M. Suzuki, T. Kawakami, T. Arai, Y. Koide, T. Uemura, N. Shibata and M. Murakami, *Appl. Phys. Lett.* **74** 275 (1999).
112. E. F. Schubert, W. Grieshaber and I. D. Goepfert, *Appl. Phys. Lett.* **69** 37371 (1996).
113. L. Zhou, A. T. Ping, F. Khan, A. Osinsky and I. Adesida, *Electron. Lett.* **36** 91 (2000).

114. N. V. Ewards, M. D. Bremser, T. W. Weeks, R. S. Kerm, R. F. Davis and D. E. Aspnes, *Appl. Phys. Lett.* **69** 2065 (1996).

115. V. M. Bermudez, *J. Appl. Phys.* **80** 1190 (1996).

116. L. L. Smith, S. W. King, R. J. Nemanich, R. F. Davis, *J. Electron. Mat.* **25** 805 (1996).

117. J. S. Jang, S. J. Park and T. Y. Seong, *J. Vac. Sci. Technol. B* **17** 2667 (1999).

118. M. W. Cole, D. W. Eckart, W. Y. Han, R. L. Pfeffer, and T. Monahan, F. Ren, C. Yuan and R. A. Stall, S. J. Pearton, Y. Li and Y. Lu, *J. App. Phys.* **80** 278 (1996).

119. M. W. Cole, F. Ren and S. J. Pearton, *J. Electron. Soc.* **144** L275 (1997); *Appl. Phys. Lett.* **71** 3004 (1997).

120. H. S. Venugopalan, S. E. Mohney, B. P. Luther, J. M. DeLucca, S. D. Wolter, J. M. Redwing and G. E. Bulman, *Mat. Res. Soc. Symp. Proc.* **468** 431 (1997).

121. J. T. Trexler, S. J. Miller, P. H. Holloway and M. A. Khan, *Mat. Res. Soc. Symp. Proc.* **395** 819 (1996).

122. J. Y. Chen, C. J. Pan and G. C. Chi, *Solid-State Electron.* **43** 649 (1999).

123. A. T. Ping, Q. Chen, J. W. Yang, M. A. Khan and I. Adesida, *J. Electron. Mater.* **27** 261 (1998).

124. C.R. Eddy, Jr. and B. Molnar, *Mat. Res. Soc. Symp. Proc.* **395**, 745 (1996); *J. Electron. Mater.* **28**, 314 (1999).

125. S. J. Pearton, J. W. Lee, J. D. MacKenzie, C. R. Abernathy and R. J. Shul, *Appl. Phys. Lett.* **67**, 2329 (1995).

126. F. Ren, J. R. Lothian, S. J. Pearton, C. R. Abernathy, C. B. Vartuli, J. D. MacKenzie, R. G. Wilson and R. F. Karlicek, *J. Electron. Mater.* **26**, 1287 (1997).

127. K. Saotome, A. Matsutani, T. Shirasawa, M. Mori, T. Honda, T. Sakaguchi, F. Koyama and K. Iga, *Mat. Res. Soc. Symp. Proc.* **449** 1029 (1997).

128. R. J. Shul, L. Zhang, A. G. Baca, C. G. Willison, J. Han, S. J. Pearton, F. Ren, J. C. Zolper and L. F. Lester, *Mat. Res. Soc. Symp. Proc. Vol.* **573**, 161 (1999).

129. B. J. Kim, J. W. Lee, H. S. Park, T. I. Kim, *J. Electron. Mat.* **27** L32 (1998).

130. C. Youtsey, G. Bulman and I. Adesida, *J. Electron. Meter.* **27** 282 (1998).

131. Y. Ohba and A. Hatano, *J. Cryst. Growth* **145** 214 (1994).
132. S. J. Pearton, J. C. Zolper, R. J. Shul and F. Ren, *J. Appl. Phys.* **86** 1 (1999).
133. P. M. Bridger, Z. Z. Bandic, E. C. Piquette and T. C. McGill, *Appl. Phys. Lett.* **73** 3438 (1998).
134. Z. Z. Bandic, P. M. Bridger, E. C. Piquette and T. C. McGill, *Appl. Phys. Lett.* **72** 3166 (1998).
135. *Atlas User's Manual* (Silvaco International, Santa Clara, California, 1998).
136. *Properties, Processing and Applications of GaN and Related Semiconductors*, ed. J.H. Edgar, S. Strife, I. Akasaki, H. Amano and C. Wetzel, EMIS DataReview No. 23 (IEE, London, 1999).
137. H.P. Gillis, D. A. Choutov, K. P. Martin, S. J. Pearton and C. R. Abernathy, *J. Electrochem. Soc.* **143** L251 (1996).
138. R. T. Leonard and S. M. Bedair, *Appl. Phys. Lett.* **68** 794 (1996).

BIOGRAPHICAL SKETCH

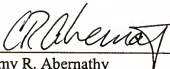
Xian-an Cao was born in Huaining, Anhui, China, on March 31, 1972. After completing 11-year's primary and secondary education in his hometown, and one-year's military training in North China, he moved to Shanghai, and started his undergraduate study at Fudan University in 1991, majoring in physics. In the fall of 1994, he was admitted to the graduate program at Fudan one year ahead of schedule. Under Professor Hou's guidance, he successfully finished his research thesis on sulfur passivation of the GaAs surfaces and devices. With a strong interest in semiconductor technology, and desire for a more nurturing academic atmosphere, Xian-an joined Professor Pearton's group at University of Florida in 1997, working on GaN processing and devices. Since then, he has moved steadily toward his goal to be a successful researcher and become confident to face any challenge in the future.

I certify that I have read this study and that in my opinion it conforms to acceptable standards of scholarly presentation and is fully adequate, in scope and quality, as a dissertation for the degree of Doctor of Philosophy.



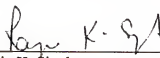
Stephen J. Pearton, Chairman
Professor of Materials Science
and Engineering

I certify that I have read this study and that in my opinion it conforms to acceptable standards of scholarly presentation and is fully adequate, in scope and quality, as a dissertation for the degree of Doctor of Philosophy.



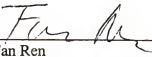
Cammy R. Abernathy
Professor of Materials Science
and Engineering

I certify that I have read this study and that in my opinion it conforms to acceptable standards of scholarly presentation and is fully adequate, in scope and quality, as a dissertation for the degree of Doctor of Philosophy.



Rajiv K. Singh
Professor of Materials Science
and Engineering

I certify that I have read this study and that in my opinion it conforms to acceptable standards of scholarly presentation and is fully adequate, in scope and quality, as a dissertation for the degree of Doctor of Philosophy.



Fan Ren
Professor of Chemical Engineering

I certify that I have read this study and that in my opinion it conforms to acceptable standards of scholarly presentation and is fully adequate, in scope and quality, as a dissertation for the degree of Doctor of Philosophy.

Fred Sharifi

Fred Sharifi
Associate Professor of Physics

This dissertation was submitted to the Graduate Faculty of the College of Engineering and to the Graduate School and was accepted as partial fulfillment of the requirements for the degree of Doctor of Philosophy.

May, 2000

C *C*

M. J. Ohanian
Dean, College of Engineering

Winfred M. Phillips
Dean, Graduate School